

# Joining of Tubular Metal-Composite Parts Using the Electromagnetic Pulse Technology

Carlos Alberto dos Santos Silva Carneiro

*Relatório do Projeto Final / Dissertação do MIEM*

Orientador no INEGI: Eng. Inês Oliveira

Orientador na FEUP: Prof. Ana Reis

Mestrado Integrado em Engenharia Mecânica



Departamento de Engenharia Mecânica

Janeiro de 2017



# RESUMO

---

A evolução das indústrias aeroespacial e automóvel tem promovido o interesse em estruturas híbridas metal-compósito. No entanto, uma das maiores dificuldades na conceção deste tipo de estruturas é a união de materiais com propriedades tão distintas. Os métodos convencionais, como elementos de fixação ou adesivos podem ser utilizados; no entanto acarretam limitações como a concentração de tensões e adição de material no caso da fixação mecânica, ou a necessidade de preparação das superfícies no caso das juntas adesivas. A tecnologia de fabrico por impulsos eletromagnéticos permite a união de componentes de diferentes materiais, conseguindo ainda ultrapassar algumas das limitações impostas pelos métodos convencionais. Neste processo de conformação a alta velocidade, a passagem de corrente elétrica de elevada intensidade por uma bobine gera campos magnéticos pulsados, responsáveis pela aplicação de forças de Lorentz à peça. Este processo permite deformar plasticamente, cortar e unir metais com elevada condutividade elétrica sem que exista contacto entre a ferramenta e os componentes.

Na presente dissertação pretende-se estudar a viabilidade técnica do processo EMPT (Electromagnetic Pulse Technology) para a produção de juntas em peças tubulares metal-compósito. Três juntas são desenhadas e produzidas usando níveis de energia diferentes. São utilizados tubos de alumínio (EN AW 6082) e varões de poliamida reforçada com fibra de vidro (Ertalon PA 6.6 GF30). As juntas produzidas são posteriormente avaliadas com recurso a uma análise materialográfica e ensaios de tração a fim de verificar a viabilidade do processo. Os resultados obtidos comprovam a viabilidade da produção de juntas entre peças tubulares metal-compósito por compressão eletromagnética. É também apresentado um modelo de elementos finitos para simular o processo de cravação de juntas de tubos por forças eletromagnéticas. Implementou-se um modelo desacoplado. O problema eletromagnético é resolvido através do software de cálculo elétrico e magnético por elementos finitos FEMM. A pressão magnética calculada é introduzida no modelo mecânico tridimensional desenvolvido no Abaqus a fim de replicar a componente experimental desta tese. A validação da simulação é efectuada usando os micro-cortes e os ensaios de tração, exibindo uma boa concordância com os resultados experimentais pela comparação dos deslocamentos do tubo e regiões críticas.

**Palavras-chave:** Tecnologia de fabrico por impulsos electromagnéticos; Cravação por forças electromagnéticas; Estruturas híbridas metal-compósito; União de tubos; Compressão eletromagnética de tubos; Análise experimental; Modelação numérica.



# ABSTRACT

---

The development of the transport and aerospace industries has led to an increasing interest in hybrid metal-composite structures. However, one of the main difficulties in designing this kind of structures relates to the capability of joining such different materials. Conventional methods such as mechanical fastening of components or adhesive bonding can be used. However, they present well known limitations, such as the need for surface preparation, for the case of adhesive bonding, and the concentration of stresses and material addition, in mechanical fastened components. The electromagnetic pulse technology (EMPT) is a technique capable of achieving these demanding goals while overcoming some of the conventional methods' flaws. The commonly known as "electromagnetic forming" process allows not only to form tubes and sheet metal but it is also used for joining and cutting operations involving metallic materials with high electrical conductivity. This high-velocity forming method uses pulsed magnetic fields to apply Lorentz forces to metal workpieces: the workpiece's deformation is governed by the interaction of a transient magnetic field induced by a coil and second magnetic field, created by Eddy currents in the surface of the workpiece. The result is a contact-free application of force.

This thesis intends to experimentally study the viability of the EMPT in the form-fit joining of metal-composite tubes. Three joint designs have been developed according to previously existing guidelines for this type of connection. Joints were produced using different energy levels. Aluminum tubes (EN AW 6082) and a glass-fiber reinforced polyamide (Ertalon PA6.6 GF30) are used. They are then evaluated using materialographic analysis and tensile tests in order to prove the applicability of the EMPT in the form-fit joining of metal and composite tubular workpieces. A numerical model has also been created to simulate the joining process by electromagnetic tube compression. An uncoupled approach for the problem has been employed. The electromagnetic model was solved using the FEMM electric and magnetic finite element software. The magnetic pressure calculated is then used as input in the 3D Abaqus mechanical model created to replicate the experimental component of this dissertation. The simulation is validated using the micro-cuts and tensile tests' results, showing good correlation between numerical and experimental results concerning groove filling, displacements, and critical zones. The results obtained from the tensile tests and the micro-cuts prove the feasibility of the production of form-fit joints through tube compression against a composite mandrel.

**Keywords:** Electromagnetic pulse technology; Electromagnetic forming; Metal-composite hybrid structures; Tube joining; Tube compression; Experimental analysis; Numerical modelling.

# AGRADECIMENTOS

---

Esta dissertação contou com o apoio de diversas pessoas e entidades que contribuíram, direta ou indiretamente, para o meu sucesso nesta etapa da minha formação académica. A todos eles deixo o meu profundo agradecimento.

Em primeiro lugar gostaria de agradecer ao INEGI – Instituto de Ciência e Inovação em Engenharia Mecânica e Engenharia Industrial e à Professora Doutora Ana Reis, orientadora desta dissertação, pela possibilidade de elaborar um trabalho numa área científica tão pouco explorada e de elevado interesse tecnológico.

Em seguida, um sincero agradecimento à Doutora Inês Oliveira, orientadora deste trabalho, e cujo apoio foi a chave para a elaboração deste projeto. A sua disponibilidade, empenho e dedicação desde o primeiro contacto serviram de motivação acrescida para o desenvolvimento desta dissertação. Um sincero obrigado pelos conhecimentos transmitidos, pelo acompanhamento exemplar e pela atenção dedicada a este projeto.

Aos meus pais, que ao longo da minha vida tudo fizeram para que conseguisse atingir os meus objetivos. É a eles que dedico este trabalho, em troca do apoio, da persistência e de todas as ferramentas que contribuíram para a minha formação tanto a nível académico como pessoal.

Deixo ainda uma palavra de agradecimento aos meus amigos que me acompanham há mais ou menos tempo, e que neste período não só me apoiaram nas mais diversas ocasiões, como também me souberam desencaminhar quando era preciso.



# CONTENTS

---

<b>RESUMO .....</b>	<b>iii</b>
<b>ABSTRACT.....</b>	<b>v</b>
<b>AGRADECIMENTOS.....</b>	<b>vii</b>
<b>CONTENTS .....</b>	<b>ix</b>
<b>LIST OF FIGURES .....</b>	<b>xiii</b>
<b>LIST OF TABLES .....</b>	<b>xvii</b>
<b>LIST OF SYMBOLS .....</b>	<b>xix</b>
<b>LIST OF ABBREVIATIONS.....</b>	<b>xxi</b>
<b>1 INTRODUCTION.....</b>	<b>1</b>
1.1 Motivation.....	1
1.2 Objectives.....	2
1.3 Scope and Layout of the Thesis.....	3
<b>2 LITERATURE REVIEW .....</b>	<b>5</b>
2.1 The Electromagnetic Pulse Technology .....	5
2.2 RLC Analogy.....	6
2.3 Equipment.....	8
2.3.1 Pulsed Power Generator .....	8
2.3.2 Tool Coil.....	8
2.3.3 Fieldshaper .....	10
2.3.4 Form Defining Tools.....	10
2.4 Advantages and Disadvantages.....	11
2.5 Joining by EMPT.....	12
2.5.1 Interference-Fit Joints .....	13
2.5.2 Form-Fit Joints .....	14
2.6 Summary and Outlook .....	22

---

<b>3</b>	<b>DESIGN OF FORM-FIT JOINTS .....</b>	<b>23</b>
3.1	Considerations for the Geometric Parameter's .....	23
3.2	Definition of the Geometric Parameters .....	24
3.3	Joint Designs.....	25
3.3.1	Joint 1 .....	25
3.3.2	Joint 2 .....	26
3.3.3	Joint 3 .....	27
<b>4</b>	<b>EXPERIMENTAL PROCEDURE .....</b>	<b>29</b>
4.1	Materials and Experimental Setup .....	29
4.1.1	Materials .....	29
4.1.2	EMPT Machine.....	29
4.1.3	Coil and Workpiece Setup .....	30
4.2	Design of the Experiment.....	33
4.3	Results.....	37
4.3.1	Cross-Section Analysis.....	37
4.3.2	Tensile Tests .....	41
4.4	Summary and Outlook .....	57
<b>5</b>	<b>NUMERICAL MODELLING OF EMPT JOINING .....</b>	<b>59</b>
5.1	Review on EMPT Modelling and Simulations.....	60
5.2	Creation of the Form-Fit Joining Model.....	62
5.2.1	Assumptions .....	62
5.2.2	The Electromagnetic Model .....	63
5.2.3	The Mechanical Model.....	69
5.3	Results for the FE Simulation .....	70
5.3.1	Diameter Reduction .....	70
5.4	Discussion and Conclusions.....	78
5.5	Summary and Outlook .....	81
<b>6</b>	<b>CONCLUSIONS .....</b>	<b>83</b>
6.1	Conclusions .....	83
6.2	Future Work .....	85
<b>7</b>	<b>REFERENCES .....</b>	<b>87</b>
<b>8</b>	<b>ANNEXES .....</b>	<b>91</b>
8.1	Joint design 1 (single axial groove) .....	92
8.2	Joint design 2 (double axial groove) .....	93

8.3	Joint design 3 (axial and torque grooves) .....	94
8.4	EN AW 6082 Data Sheet.....	95
8.5	Ertalon 6.6 GF 30 Data Sheet .....	96



# LIST OF FIGURES

---

FIGURE 1 - FIRST MASS PRODUCTION APPLICATION OF EMPT BY RING COMPRESSION [9].....	5
FIGURE 2 - REPRESENTATION OF THE ELECTROMAGNETIC TUBE COMPRESSION PROCESS. THE CURRENT FLOWING THROUGH THE COIL IS ULTIMATELY TRANSFORMED INTO A MAGNETIC FORCE/PRESSURE, REPELLING THE COIL AND WORKPIECE [27]. .....	6
FIGURE 3- EQUIVALENT RLC CIRCUIT FOR THE ELECTROMAGNETIC FORMING PROCESS [8]. .....	7
FIGURE 4- REPRESENTATION OF A) THE EMPT CIRCUIT; B) THE CURRENT $I(t)$ AND C) THE MAGNETIC PRESSURE $P_m(t)$ [8]. .....	7
FIGURE 5- COIL-WORKPIECE CONFIGURATION FOR A) TUBE COMPRESSION, B) TUBE EXPANSION, C) SHEET METAL FORMING [6].....	9
FIGURE 6 - SINGLE TURN COIL [10].....	9
FIGURE 7- SCHEME OF ELECTROMAGNETIC TUBE COMPRESSION WITH A FIELD SHAPER [13].....	10
FIGURE 8- USING FORM DEFINING TOOLS IN EMPT [8].....	11
FIGURE 9- EMPT CRIMPING APPLIED TO JOIN DISSIMILAR MATERIALS (POLYMER-METAL) IN LIGHTWEIGHT AIRCRAFT SEATS [19]. .....	13
FIGURE 10- INTERFERENCE-FIT JOINING PROCESS DESCRIPTION [28].....	14
FIGURE 11- EXAMPLES OF MACHINED SURFACES COMPATIBLE WITH EMPT TUBE JOINING BY INTERFERENCE-FIT. A) AND B) KNURLED SURFACES; C) SCREW THREAD WITH AXIAL GROOVES; D) SCREW THREAD [35].....	14
FIGURE 12- REPRESENTATION OF THE JOINING BY FORM-FIT PROCESS [36]. .....	15
FIGURE 13- APPLICABLE GROOVE SHAPES FOR ELECTROMAGNETIC FORM-FIT JOINTS [13].....	15
FIGURE 14- GEOMETRIC GROOVE PARAMETERS AFFECTING JOINT STRENGTH USING RECTANGULAR GROOVES [34].....	15
FIGURE 15- EXAMPLE OF LOAD-EXTENSION CURVE PLOTTED BY WEDDELING. JOINT FAILURE OCCURS AT FJ, WHERE THERE IS THE FIRST RELATIVE MOVEMENT BETWEEN THE TUBE AND MANDREL [36]...	16
FIGURE 16- FAILURE MODES OBSERVED IN WEDDELING'S WORK. ON THE LEFT, FAILURE BY TUBE/MANDREL PULL-OUT; ON THE RIGHT, TUBE SHEARING [36]. .....	17
FIGURE 17- RELATIONSHIP BETWEEN PULL-OUT FORCE AND GROOVE SHAPE [36]. .....	17
FIGURE 18- RADIOSCOPIC PICTURES OF AXIAL JOINTS WITH DIFFERENT SHAPES [36]. .....	18
FIGURE 19- RELATIONSHIP BETWEEN PULL-OUT FORCE AND GROOVE DIMENSIONS [36]. .....	18
FIGURE 20- RADIOSCOPIC IMAGES OF RECTANGULAR GROOVES WITH DIFFERENT DEPTHS. THE RELATION BETWEEN DEPTH AND ANGLE $\alpha$ AND BETWEEN DEPTH AND DEFORMATION DEGREE IS VISIBLE [36].....	19
FIGURE 21- RELATIONSHIP BETWEEN PULL-OUT FORCE AND CHARGING ENERGY FOR VARIOUS GROOVE DEPTHS [36].....	19
FIGURE 22- INFLUENCE OF THE MAGNETIC PRESSURE IN FILLING THE GROOVES [36]. .....	20
FIGURE 23 - CUT-VIEW OF A DOUBLE GROOVE FORM-FIT AXIAL JOINT [38].....	20
FIGURE 24- EXAMPLE OF THE SOCKETS USED FOR FORM-FIT CONNECTIONS USING EMPT [34]. .....	21

FIGURE 25 - ISOMETRIC VIEW OF JOINT 1 (FROM SOLIDWORKS). .....	25
FIGURE 26 - SIDE VIEW OF JOINT 1 (FROM SOLIDWORKS). .....	26
FIGURE 27 - ISOMETRIC VIEW OF JOINT 2 (FROM SOLIDWORKS). .....	27
FIGURE 28 - SIDE VIEW OF JOINT 2 (FROM SOLIDWORKS). .....	27
FIGURE 29 - ISOMETRIC VIEW OF JOINT 3 (FROM SOLIDWORKS). .....	28
FIGURE 30 - SIDE VIEW OF JOINT 3 (FROM SOLIDWORKS). .....	28
FIGURE 31 - EMPT SYSTEM USED FOR THE EXPERIMENTAL PROCEDURES [51]. .....	30
FIGURE 32 – CUT-VIEW OF THE SOLIDWORKS MODEL FOR THE COIL AND WORKPIECES ASSEMBLY. ....	30
FIGURE 33 - DETAIL OF THE POSITIONING AND CONSTRAINING SYSTEM. ....	31
FIGURE 34 - DETAIL OF THE ADAPTED POSITIONING SYSTEM. ....	32
FIGURE 35 - CUT VIEW OF THE COIL-GROOVE OVERLAPPING AREA (SOLIDWORKS). ....	32
FIGURE 36 - RESULT OF THE PRELIMINARY TEST AT 14 KV (TOP) AND 16 KV (BOTTOM). .....	33
FIGURE 37 - BROKEN JOINT PRODUCED AT 16 KV. ....	34
FIGURE 38 - SCHEME FOR THE CUT OF THE SPECIMENS. ....	34
FIGURE 39 - TEST SPECIMEN PRODUCED AT 14 KV AFTER A LONGITUDINAL CUT WITH NO VISIBLE CRACKS AND WITH ALMOST COMPLETE FILLING OF THE CAVITY. ....	35
FIGURE 40 - DETAIL OF THE GROOVE REGION OF THE CUT SPECIMEN. ....	35
FIGURE 41 - EXAMPLE OF A FORM-FIT JOINT FOR DESIGN 1. ....	36
FIGURE 42 - EXAMPLE OF A FORM-FIT JOINT FOR DESIGN 2. ....	36
FIGURE 43 - EXAMPLE OF A FORM-FIT JOINT FOR DESIGN 3. ....	36
FIGURE 44 - JOINT 1: MICROSCOPE IMAGES OF THE GROOVE'S AREA WITH 7.5X ZOOM (ON THE LEFT COLUMN) AND DETAILED VIEW OF THE TOP HALF-SECTION WITH 30X ZOOM (ON THE RIGHT COLUMN) FOR THE PROPOSED ENERGY LEVELS. ....	37
FIGURE 45 - JOINT 2: MICROSCOPE IMAGES OF THE GROOVE'S AREA WITH 7.5X ZOOM (ON THE LEFT COLUMN) AND THE DETAILED VIEW OF THE TOP HALF SECTION WITH 30X ZOOM, EMPHASIZING THE DEEPER GROOVE (ON THE RIGHT COLUMN) FOR THE PROPOSED ENERGY LEVELS. ....	38
FIGURE 46 - CRACKED REGION IN JOINT L2D2. ....	39
FIGURE 47 - JOINT 3: MICROSCOPE IMAGES OF THE GROOVE'S AREA WITH 7.5X ZOOM (ON THE LEFT COLUMN) AND THE DETAILED VIEW OF THE TOP HALF SECTION WITH 30X ZOOM, EMPHASIZING THE DEEPER GROOVE (ON THE RIGHT COLUMN) FOR THE PROPOSED ENERGY LEVELS. ....	39
FIGURE 48 - DETAIL OF THE MOST DAMAGED REGION FOR JOINT L3D3. ....	40
FIGURE 49 - SETUP OF THE TENSILE TESTING. ....	41
FIGURE 50 - SNUG-FITTING METAL PLUG INSERTED IN THE TUBE'S ENDING [ASTM A370] [54]. ....	42
FIGURE 51 - LOAD-DISPLACEMENT CURVES FOR JOINT L1D1. ....	42
FIGURE 52 - JOINTS L1D1-2 (BOTTOM) AND L1D1-3 (TOP) AFTER TENSILE TESTING. NOTICE THE PLASTIC DEFORMATION OF THE ALUMINUM TUBE OUT OF THE GROOVE. ....	43
FIGURE 53 - LOAD-DISPLACEMENT CURVES FOR JOINT L2D1. ....	44
FIGURE 54 - JOINTS L2D1-2 (BOTTOM) AND L2D1-3 (TOP) AFTER TENSILE TESTING. ....	45
FIGURE 55 - DETAIL OF THE FRACTURE SURFACE FOR JOINTS L2D1-2 (RIGHT) AND L2D1-3 (LEFT). ....	45
FIGURE 56 - LOAD-DISPLACEMENT CURVES FOR JOINT L3D1. ....	46
FIGURE 57 - JOINTS L3D1-2 (BOTTOM) AND L3D1-3 (TOP) AFTER TENSILE TESTING. ....	46
FIGURE 58 - LOAD-DISPLACEMENT CURVES FOR JOINT L1D2. ....	47
FIGURE 59 - JOINTS L1D2-2 (BOTTOM) AND L1D2-3 (TOP) AFTER TENSILE TESTING. ....	48
FIGURE 60 - LOAD-DISPLACEMENT CURVES FOR JOINT L2D2. ....	49
FIGURE 61 - LOAD-DISPLACEMENT CURVES FOR JOINT L3D2. ....	50
FIGURE 62 - JOINTS L3D2-2 (BOTTOM) AND L3D2-3 (TOP) AFTER TENSILE TESTING. ....	50
FIGURE 63 - LOAD-DISPLACEMENT CURVES FOR JOINT L1D3. ....	51
FIGURE 64 - JOINTS L1D3-2 (BOTTOM) AND L1D3-3 (TOP) AFTER TENSILE TESTING. ....	52
FIGURE 65 - LOAD-DISPLACEMENT CURVES FOR JOINT L2D3. ....	53
FIGURE 66 - JOINTS L2D3-2 (BOTTOM) AND L2D3-3 (TOP) AFTER TENSILE TESTING. ....	53

FIGURE 67 - LOAD-DISPLACEMENT CURVE FOR JOINT L3D3.....	54
FIGURE 68 - JOINTS L3D3-2 (BOTTOM) AND L3D3-3 (TOP) AFTER TENSILE TESTING. ....	55
FIGURE 69 - INTERACTIONS BETWEEN THE ELECTROMAGNETIC, MECHANICAL AND THERMAL PROBLEMS [55].....	59
FIGURE 70 - SCHEME OF THE FEA MODEL PERFORMED BY NASSIRI ET AL. [59]. ....	61
FIGURE 71 - COMPARISON BETWEEN SIMULATION AND EXPERIMENTAL DATA DEVELOPED BY CONRAUX ET AL. REGARDING EMPT TUBE COMPRESSION [55].....	62
FIGURE 72 - GEOMETRY INPUT FOR THE ELECTROMAGNETIC SIMULATION IN FEMM.....	63
FIGURE 73 - CURRENT CURVES CALCULATED USING THE MACHINE PARAMETERS REFERRED ABOVE. ....	65
FIGURE 74 - FLOWCHART OF THE MODELLING STEPS IN FEMM [51].....	66
FIGURE 75 - SCREEN-SHOT OF THE FEMM MODEL.....	66
FIGURE 76 - MAGNETIC FIELD DENSITY FOR A 12.5 KV DISCHARGE.....	67
FIGURE 77 - MAGNETIC PRESSURE DISTRIBUTION ALONG THE TUBE LENGTH FOR THE THREE ENERGY LEVELS. ....	68
FIGURE 78 - NODE SETS CHOSEN FOR THE TARGET FOR JOINTS 2 AND 3. ....	71
FIGURE 79 - REPRESENTATION OF THE NODE SET CHOSEN FOR THE TUBE ANALYSIS. ....	71
FIGURE 80 - FINAL FRAME OF JOINT 2'S SIMULATION WITH PLOT CONTOURS REPRESENTING DISPLACEMENT (MAGNITUDE). ....	72
FIGURE 81 - FINAL FRAME OF JOINT 3'S SIMULATION WITH PLOT CONTOURS REPRESENTING DISPLACEMENT (MAGNITUDE). ....	73
FIGURE 82 - EVOLUTION OF THE RADIUS FOR THE FULL LENGTH OF THE SAMPLE FOR DIFFERENT ENERGY LEVELS IN JOINT 2. ....	74
FIGURE 83 - ZOOMED EVOLUTION OF THE RADIUS FOR THE SAMPLES IN JOINT 2. ....	74
FIGURE 84 - NODAL DISTRIBUTION EMPHASIZING THE REBOUND PHENOMENA OCCURRING IN THE SIMULATION. ....	75
FIGURE 85 - EVOLUTION OF THE RADIUS FOR THE FULL LENGTH OF THE SAMPLE FOR DIFFERENT ENERGY LEVELS IN JOINT 3. ....	76
FIGURE 86 - DETAIL OF THE EVOLUTION OF THE RADIUS WITH THE LENGTH OF THE SAMPLE FOR DIFFERENT ENERGY LEVELS IN JOINT 3. ....	76
FIGURE 87 - DETAIL OF THE EVOLUTION OF THE RADIUS WITH THE LENGTH OF THE SAMPLE FOR DIFFERENT ENERGY LEVELS IN JOINT 3 (TORQUE GROOVE).....	77
FIGURE 88 - DETAIL OF THE EVOLUTION OF THE RADIUS WITH THE LENGTH OF THE SAMPLE FOR DIFFERENT ENERGY LEVELS IN JOINT 3 (RADIAL GROOVE).....	77
FIGURE 89 - COMPARISON BETWEEN THE NUMERICAL SIMULATION ANT THE CUT VIEWS FOR JOINT 2 FORMED WITH 12.5 KV. ....	79
FIGURE 90 - COMPARISON BETWEEN THE NUMERICAL SIMULATION AND THE CUT-VIEWS FOR JOINT 2 FORMED WITH 14 KV. ....	79
FIGURE 91 - COMPARISON BETWEEN THE NUMERICAL SIMULATION AND THE CUT VIEWS FOR JOINT 2 FORMED WITH 15 KV. ....	80
FIGURE 92 - COMPARISON BETWEEN THE NUMERICAL SIMULATION ANT THE CUT VIEWS FOR JOINT 3 FORMED WITH 12.5 KV. ....	80
FIGURE 93 - COMPARISON BETWEEN THE NUMERICAL AND THE CUT-VIEW FOR JOINT 3 FORMED WITH 14 KV. ....	81
FIGURE 94 - COMPARISON BETWEEN THE NUMERICAL SIMULATION AND THE CUT-VIEW FOR JOINT 3 FORMED WITH 15 KV. ....	81
FIGURE 95 - JOINT DESIGN 4 (FROM SOLIDWORKS).....	85
FIGURE 96 - JOINT DESIGN 5 (FROM SOLIDWORKS).....	86



# LIST OF TABLES

---

TABLE 1 - DIMENSIONS CHOSEN FOR JOINT 1. ....	26
TABLE 2 – DIMENSIONS CHOSEN FOR JOINT 2.....	26
TABLE 3 - DIMENSIONS CHOSEN FOR JOINT 3. ....	28
TABLE 4 - ELECTROMAGNETIC PULSE MACHINE'S SPECIFICATIONS.....	29
TABLE 5 - ELECTRICAL AND GEOMETRICAL PROPERTIES OF THE COIL.....	30
TABLE 6 - DESIGN OF EXPERIMENTS PROPOSED TO EVALUATE THE EMPT FORM-FIT JOINING. ....	35
TABLE 7 - MAXIMUM LOAD AND CORRESPONDING DISPLACEMENT FOR THE L1D1 JOINTS. ....	43
TABLE 8 - MAXIMUM LOAD AND CORRESPONDING DISPLACEMENT FOR THE L2D1 JOINTS. ....	44
TABLE 9 - MAXIMUM LOAD AND CORRESPONDING DISPLACEMENT FOR THE L3D1 JOINTS. ....	47
TABLE 10 - MAXIMUM LOAD AND CORRESPONDING DISPLACEMENT FOR THE L1D2 JOINTS.....	48
TABLE 11 - MAXIMUM LOAD AND CORRESPONDING DISPLACEMENT FOR THE L2D2 JOINTS.....	49
TABLE 12 - MAXIMUM LOAD AND CORRESPONDING DISPLACEMENT FOR THE L3D2 JOINTS.....	51
TABLE 13 - MAXIMUM LOAD AND CORRESPONDING DISPLACEMENT FOR THE L1D3 JOINTS.....	52
TABLE 14 - MAXIMUM LOAD AND CORRESPONDING DISPLACEMENT FOR THE L2D3 JOINTS.....	54
TABLE 15 - MAXIMUM LOAD AND CORRESPONDING DISPLACEMENT FOR THE L3D3 JOINTS.....	55
TABLE 16 - REARRANGEMENT OF THE TENSILE TESTS RESULTS WITH RESPECTIVE FAILURE MODES. ....	56
TABLE 17 - MATERIAL, MACHINE AND GEOMETRIC PROPERTIES USED IN THE FEMM SIMULATION. ....	64
TABLE 18 - DENSITY AND ELASTIC PROPERTIES FOR THE ALUMINUM TUBE [65]. ....	69
TABLE 19 - JOHNSON-COOK PLASTIC PROPERTIES FOR THE ALUMINUM TUBE [65].....	69
TABLE 20 - DENSITY, ELASTIC AND HASHIN DAMAGE PROPERTIES USED IN THE COMPOSITE MODELLING. .....	69
TABLE 21 - MINIMUM RADIUS DETECTED IN THE SIMULATION AT EACH GROOVE FOR THE DIFFERENT ENERGY LEVELS (JOINT 2). ....	74
TABLE 22 - MINIMUM RADIUS DETECTED IN THE SIMULATION AT EACH GROOVE FOR THE DIFFERENT ENERGY LEVELS (JOINT 3). ....	78
TABLE 23 - NUMERICAL AND EXPERIMENTAL VALUES FOR THE MINIMUM EXTERNAL DIAMETER IN THE TUBE FOR JOINT 2. ....	78
TABLE 24 - NUMERICAL AND EXPERIMENTAL VALUES FOR THE MINIMUM EXTERNAL DIAMETER IN THE TUBE FOR JOINT 3. ....	78



# LIST OF SYMBOLS

---

Symbol	Description	Units
$E_c(t)$	Energy stored in the capacitor	J
$C$	Capacitance	F
$L_t$	Inductance of the circuit	H
$R_t$	Resistance of the circuit	$\Omega$
$R_{coil}$	Resistance of the coil	$\Omega$
$L_{coil}$	Inductance of the coil	H
$U(t), V_o$	Charging voltage	V
$I(t), I_{coil}$	Current of the circuit	A
$I_w(t)$	Induced current in the workpiece	A
$P_m(t)$	Magnetic pressure	Pa
$g$	Gap between coil and workpiece	m
$w$	Groove width	m
$d$	Groove depth	m
$l$	Groove length	m
$\alpha$	Angle in the deformed tube	$^\circ$
$F$	Force	N
$t$	Thickness	m
$D$	Rod diameter	m
$r$	Groove edge radius	m
$\mu$	Electrical permeability	H/m
$\mu_0$	Electrical permeability of vacuum	H/m
$\sigma$	Electrical conductivity	S/m
$\sigma_w$	Electrical conductivity of the workpiece	S/m
$\sigma_c$	Electrical conductivity of the coil	S/m
$\sigma_{air}$	Electrical conductivity of air	S/m
$\tau$	Damping factor	s
$I_0$	Maximum current	A
$\omega$	Current frequency	rad/s
$\delta$	Skin depth	m
$\rho$	Electrical resistivity of the workpiece	$\Omega/m$
$B$	Magnetic field density	T
$B_r$	Radial component of the magnetic field density	T
$B_z$	Axial component of the magnetic field density	T
$J$	Electrical current density	$A/m^2$

---

$J_\theta$	Eddy current density	A/m <sup>2</sup>
$F_r$	Radial component of the Lorentz force	N
$F_z$	Axial component of the Lorentz force	N
$P_r$	Radial component of the magnetic pressure	Pa
$P_z$	Axial component of the magnetic pressure	Pa

# LIST OF ABBREVIATIONS

---

EMPT	Electromagnetic Pulse Technology
EMF	Electromagnetic Forming
FEM	Finite Element Method



# 1 INTRODUCTION

---

## 1.1 Motivation

The requirement to produce lighter frames and more efficient structures has led to the interest in hybrid metal-composite structures for the automotive and aerospace industries. However, one of the main challenges in the design of these structures relates to the joining of the two materials. The use of hybrid metal-composite structures requires specific joining methods that guarantee the production of strong and efficient connections between materials with such different characteristics.

Adhesive bonding is a joining method that relies on the use of a polymeric adhesive to bond two surfaces of different workpieces. This method is one of the most universal joining techniques as most materials can be bonded using adhesives and whether the joint is between parts of similar or distinct materials. The benefits of adhesive bonding include the ability to withstand both static and alternating loads, the formation of a homogeneous stress distribution and the possibility to join large surfaces with thin adhering section. On the other hand, the inability to disassemble an adhesive joint can also be taken into consideration if the design involves assembling and disassembling the parts repeatedly. Another downside is that this method requires surface cleaning and preparation of the adherents in order to produce proper and lasting joints. Adhesive joints are also sensitive to environmental factors such as humidity and temperature, which may degrade the bonding prematurely. [1-4].

Mechanical fastening is a joining method fit for most material combinations: joining metals to metals, plastics to plastics and metals to plastics as well. It involves adding a fastening component (such as a rivet or a screw) in a preexisting hole drilled in both workpieces. In the case of rivet joining between metal and polymeric materials, the process depends on the geometric parameters of the rivet and the force used to apply it. This type of joints is extremely versatile but its main advantage is the ease in the assembly, disassembly, and recycling of fastened parts and of the fasteners themselves. However, this technique features peaks in the stress distribution around the holes, added weight from the fixation components as well as the need for preparation machining and drilling before the assembly. When joining metals to fiber reinforced composites, these processes may reduce the workpiece's integrity and induce premature failure in the form of delamination or fiber

breakage. They also allow the absorption of moisture which influences the structure's weight and corrosion resistance [1-4].

Welding is another joining mechanism commonly used that requires the materials to heat, melt and fuse to make the joint. Different welding processes can be used depending on the materials to be joined: conventional methods (i.e., MAG, TIG...) are used to bind metals together, however they produce more energy than the necessary for joining metals to composites or polymers. Other techniques, such as resistance welding, laser welding or ultrasonic welding can be used in order to produce polymer-polymer joints, as long as they are thermoplastics. However, there are no welding methods that allow for the creation of direct metal-composite joints. This is due to the dissimilarities of these materials when it comes to their microstructures and plasticizing temperatures: these characteristics make it impossible to design welded joints between metals and composites as on the one hand, metal and composite solubility is very low and on the other hand, the temperature needed to melt the metallic component is usually too extreme and degrades the softer polymer [1-5].

Although these metal-composite joining methods already exist, they all have specific limitations that make it important to develop new ways of bonding parts made of different materials that provide better efficiency, flexibility and quality of the joints produced. The electromagnetic pulse technology is a process capable of achieving these demanding goals.

Even though the technology's name (electromagnetic forming) may suggest otherwise, joining is the most common application. This method provides a unique way of joining similar or different materials without the use of additional fixation elements or significant heat exchanges. When compared to the conventional joining methods these joints also achieve considerably more homogeneous characteristics due to the uniform application of the magnetic pressure.

## 1.2 Objectives

The aim of this dissertation is to evaluate the viability of the EMPT in the joining process for tubular metal-composite workpieces. In order to study the magnetic pulse technology, a set of tasks was proposed:

- Joint design: development of viable geometries to be used in EMPT tube joining operations. The designed joints should withstand axial and torque solicitations and must be obtainable through conventional manufacturing processes. Several designs are to be created in order to study the influence of groove geometry;
- Experimental joining: creation of the form-fit joints using the joint designs proposed. Different discharge energies are tested in order to assess the influence of the magnetic pressure in the behaviour of the joints;
- Joint characterization and validation: evaluation of the manufactured specimens. A materialographic analysis is performed to assess groove filling and tensile tests are performed to evaluate their resistance;

- Simulation of the tube joining process: development of a numerical model that replicates the experimental procedure. It intends to be used as a tool in the design and optimization process of form-fit joints.

The last task was not proposed at in the beginning of the project. However, the numerical simulation of the joining process is considered a useful tool in the design of this type of connections by replicating the process without extensive physical testing.

### 1.3 Scope and Layout of the Thesis

In order to fulfil the main objectives proposed, this dissertation is divided in six chapters. After this short introduction, Chapter 2 presents a literature review including the basic principles of the EMPT and the description of the usual processes used for this technology. The typical components of the EMPT machine are studied as well as the advantages and disadvantages of this process compared to conventional metal forming techniques. Extensive review is performed regarding the joining techniques for tubular workpieces (force-fit and form-fit joints) and a background review of electromagnetic form-fit joints is performed in order to define the main process parameters for the creation of these joints.

Chapter 3 provides a description of the strategy and rules for the design of tubular form fit joints. Taking advantage of the review performed in the previous chapter optimal geometric parameters are proposed. Based on what is defined, five joint designs are developed to resist to axial, torsional or a combination of both solicitations. Three of those designs are chosen for further testing.

Chapter 4 includes the production process of the metal-composite tubular joints and their experimental testing. A first look is given to the materials used for the experiment and to the equipment used to manufacture these joints. As little or no previous experiments have been done regarding metal-composite joining, preliminary tests are performed in order to define the critical forming energy that caused the rupture of the composite mandrel through impact. After defining the maximum forming energy for the process, two lower energy levels are proposed and the creation of the specimens began. Three specimens of each of the nine *joint design – energy level* combinations are created. The evaluation of the joints is performed through the analysis of the axial section of a cut sample and through tensile tests. This chapter also presents the conclusions regarding the performed tests as well as regarding their correlation.

In Chapter 5, a 3D Finite Element (FE) model that replicates the tube joining process using EMPT tube compression is developed. It presents the steps along model creation and include a detailed review about the various approaches for the simulation of the electromagnetic-mechanical problem and the materials' mechanical and electric properties that are used as input for the model. Two main softwares are used for the analysis: FEMM allows for the calculation of the electromagnetic component of the problem and Abaqus is used so solve the mechanical part. An uncoupled approach is used, meaning that the solution of the electromagnetic problem is not updated after each step of the mechanical problem, providing acceptable computation times. After solving the FEMM electromagnetic problem, its output (the magnetic pressure along the tube) is used in the Abaqus software

to simulate the non-uniform magnetic pressure imposed during the process. The results obtained from Chapter 4 are then compared to the simulations' results for validation.

Finally, in Chapter 6, a brief summary of all subjects that were mentioned and the actions performed in order to write this document is presented, along with this work's main conclusions and considerations regarding the viability of the EMPT in the production of form-fit joints between metal and composite tubes. Some suggestions for future work are also presented in this chapter, along with other considerations.

## 2 LITERATURE REVIEW

---

### 2.1 The Electromagnetic Pulse Technology

Electromagnetic pulse technology (EMPT) is a high-speed forming method that takes advantage of pulsed magnetic fields to apply forces to a workpiece made of highly conductive material. This technique is therefore associated with metals and alloys such as Aluminum and Copper. The EMPT is a versatile technology that can be used for multiple applications such as forming of either tubes or sheet metal, joining of metallic closed profiles and cutting operations [1, 3, 6-17].

The first attempts to use electromagnetic forces to deform materials took place in the 1920's [9]. However, the electric currents needed to induce the electromagnetic fields required for permanent deformation were not reached due to the lack of technical knowledge and several malfunctions that occurred with the systems created, leading to a lack of interest in this subject for several decades. In the beginning of the 1960's, experiments in the area of nuclear fusion used high intensity magnetic fields in order to compress gas by discharging several connected capacitors. The currents used at the time reached around  $10^6$  Ampere and induced magnetic forces capable of deforming the conductors apart by exceeding the material's yield strength. Several experiments were made during this decade showing promising results which lead to the slow introduction of this process to the industrial environment [9].



*Figure 1 - First mass production application of EMPT by ring compression [9].*

In 1964, EMPT equipment was first used by General Motors to attach by ring compression neoprene covers to ball joints used in the automotive industry (Figure 1). The equipment used was rudimental when compared to the what is used nowadays however it relied on the same principles and was used for many years in the production of reliable automotive parts [9]. Since then, the process has evolved in terms of reliability, operator safety and ease of use as the first machines introduced were laboratory research machines adapted to the industrial needs [9, 18].

This process takes advantage of electrical and electromagnetic principles in order to deform a metallic workpiece. When a pulsed high current (usually from 100 to 1000 kA [18, 19]) flows through a conducting coil, a transient magnetic field is created. If a metallic object (the workpiece) is placed nearby the coil and therefore inside the magnetic field produced, eddy currents will be generated, flowing on the opposite direction when compared to the current flowing through the coil [6-9, 15]. These two currents will then create an intense repulsive force between the tool and the workpiece that acts like a pressure orthogonal to the workpiece surface (Figure 2) [10]. If this magnetic pressure is strong enough, meaning it is higher than the flow stress of the material, high-speed deformation will occur [13, 14]. Due to the magnitude of the magnetic pressure imposed, the workpiece can easily reach velocities around a couple hundreds of meters per second [11] and strain rates around  $10^4 \text{ s}^{-1}$ , with operation times between 10 and 100  $\mu\text{s}$ . Further information regarding the EMPT process was obtained can be obtained from [19-27] .

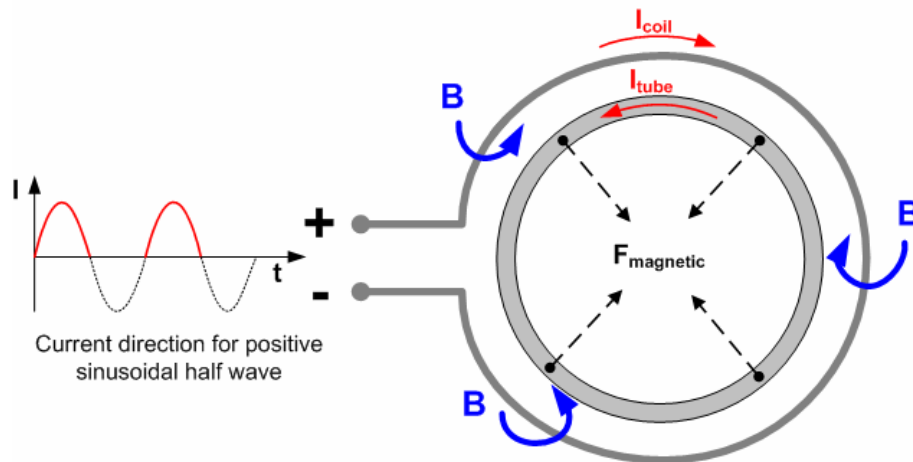


**Figure 2 - Representation of the electromagnetic tube compression process. The current flowing through the coil is ultimately transformed into a magnetic force/pressure, repelling the coil and workpiece [27].**

Although tube joining by electromagnetic compression is the most common application on the EMP technology, three process variants can be achieved depending on the geometry and positioning of the coil and workpiece: tube or hollow profile compression or expansion and 2D or 3D (preformed) metal sheet forming [6, 8]. These will be discussed in the "Equipment" Sub-Chapter.

## 2.2 RLC Analogy

The EMPT process can be represented by a RLC circuit (Figure 3) where the circuit capacitor  $C$ , the inductance  $L_i$  and the resistance  $R_i$  constitute the forming machine that is

connected to the coil's resistance  $R_{coil}$  and inductance  $L_{coil}$  in series. The energy stored in the capacitor  $E_C(t)$  can be calculated using Eq. 1 from the capacity  $C$  and the voltage  $U(t)$  [6, 8]. Common charging voltages are between 3 and 25 kV, achieving charging energies from 1 to 100 kJ [13, 28].

$$E_C(t) = \frac{1}{2} CU(t)^2 \tag{1.1}$$

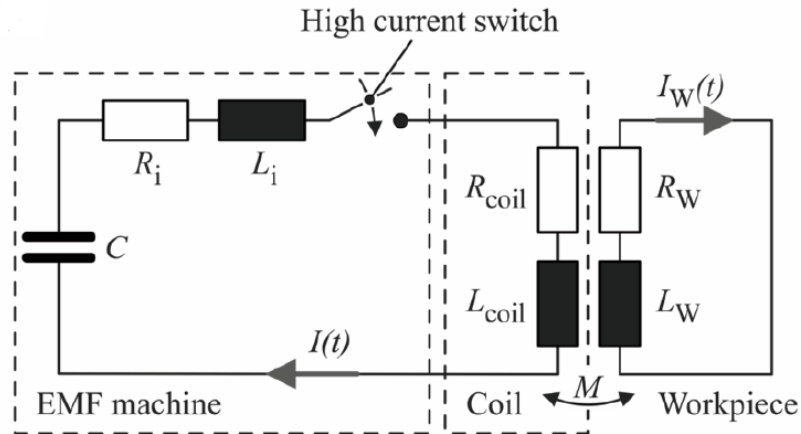


Figure 3- Equivalent RLC circuit for the electromagnetic forming process [8].

A rapid discharge generates the current  $I(t)$  or  $I_{coil}$ . This current is represented by a damped sinusoidal oscillation, determined by the forming machine's parameters (Figure 4). This current is responsible for the magnetic field which induces a secondary current  $I_W(t)$ , in the opposite direction on the surface of the workpiece. Due to the second current  $I_W(t)$ , the magnetic field  $M$  is concentrated in the gap between the coil and the workpiece [6, 8], thus creating the magnetic pressure responsible for the workpiece deformation as soon as the yield stress of the material is reached [27].

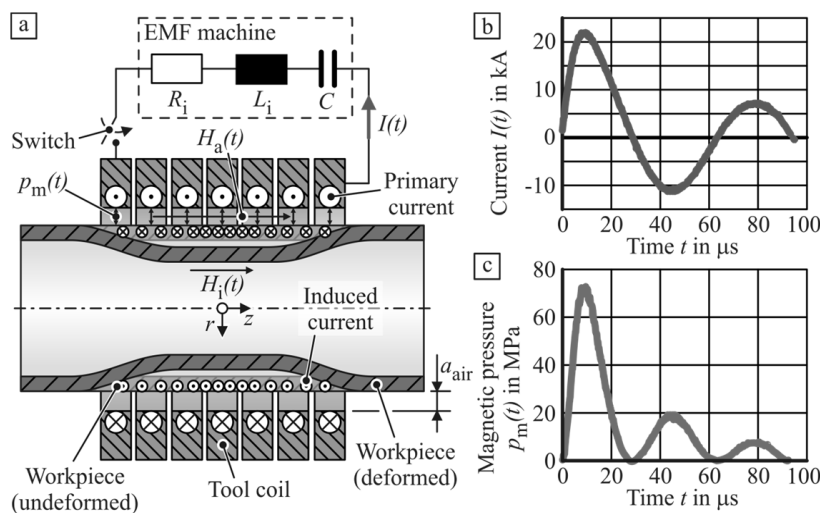


Figure 4- Representation of a) the EMPT circuit; b) the current  $I(t)$  and c) the magnetic pressure  $P_m(t)$  [8].

## 2.3 Equipment

A typical EMPT system is composed by four main elements: pulsed power generators, energy storage and control; tool coil; fieldshaper; form defining tools. These components will be studied in this chapter in order to better understand the EMP technology [8].

### 2.3.1 Pulsed Power Generator

In order to create the high energy electrical impulse required to operate this system, the first component to take into consideration is the pulse power generator. It is the element designed to store energy provided by the power source [6, 8]. As such it must be able to resist the high voltage and current necessary for the forming operations [12]. They consist in a group of capacitors connected in parallel, a charging unit and a high current switch [6, 8, 19].

### 2.3.2 Tool Coil

The coil is the element that converts the electrical energy to a magnetic pressure that will deform the workpiece. They are designed to conduct the electric current and create a suitable distribution of the magnetic field and pressure [6, 8].

They must be able to convert effectively the capacitor bank energy to deformation force while having high mechanical resistance, resistance to excessive voltage and the simplest design possible for the operation planned [8, 9].

As mentioned before, depending on the geometry and positioning of the coil and workpiece, three process variants can be achieved: tube or hollow profile compression or expansion and 2D or 3D (pre-formed) metal sheet forming [6, 8, 13].

Tube compression is achieved by using a cylindrical coil that surrounds the outer tube shell. Using the same type of coil but on the interior of the metal tube will result in an expansion. For the sheet metal forming, flat coils are used (Figure 5).

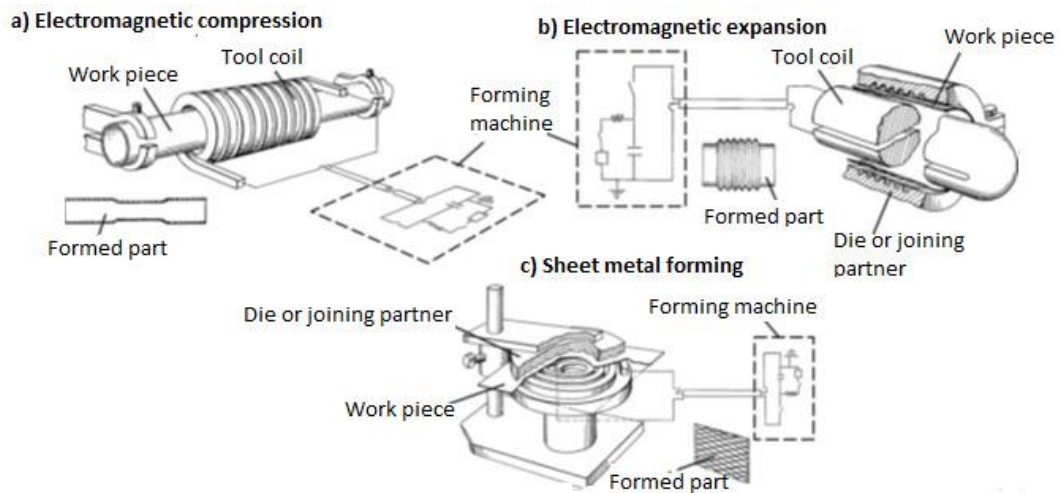


**Figure 5- Coil-workpiece configuration for a) tube compression, b) tube expansion, c) sheet metal forming [6].**

Two main coil types are used in tube forming operations: multi turn coils and single turn coils. Multi turn coils are produced by coiling highly conductive wire according to the process demands, for example coil position or workpiece size. They lack structural integrity due to their shape and therefore show a relatively short lifetime [8, 10, 29].

A single turn coil consists in a machined conductive plate, usually featuring a hole and a slot as shown in Figure 6. Although this type of coil is quite inefficient due to its low inductance, its geometry and size make it tougher and provides longer lifetime than a spiral multi turn [8, 10, 29]. The materials used for this type of coil are chosen based on their high electrical conductivity and yield strength and include high-strength aluminum alloys, copper beryllium alloys and brasses [10] and should be encapsulated with plastic materials [8, 10]. In the experimental component of this dissertation, this type of coil will be used to build the designed joints.

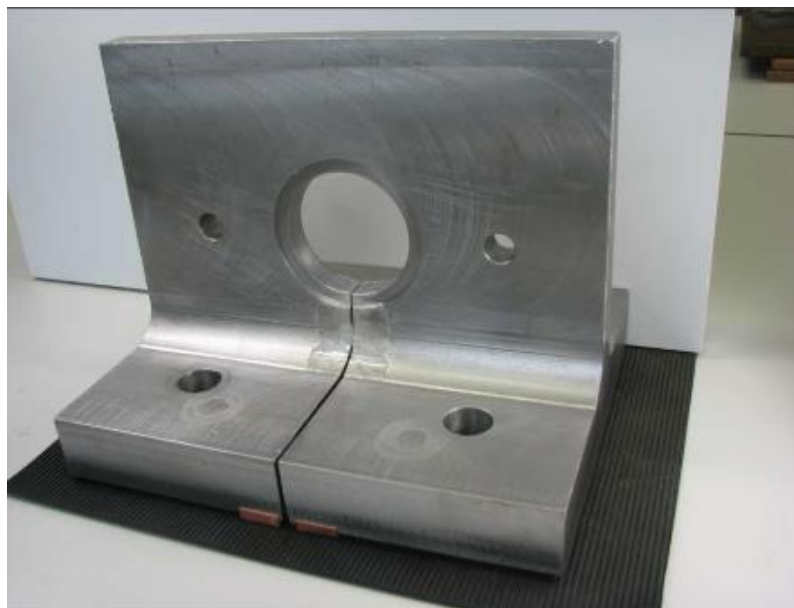


**Figure 6 - Single turn coil [10].**

### 2.3.3 Fieldshaper

The fieldshaper (Figure 7) is an optional element in an EMPT machine. Its function is to adjust and concentrate the generated magnetic field and consequent magnetic pressure in order to manufacture a better final product. It is usually an axisymmetric, highly conductive component inserted between the coil and the workpiece [8, 13].

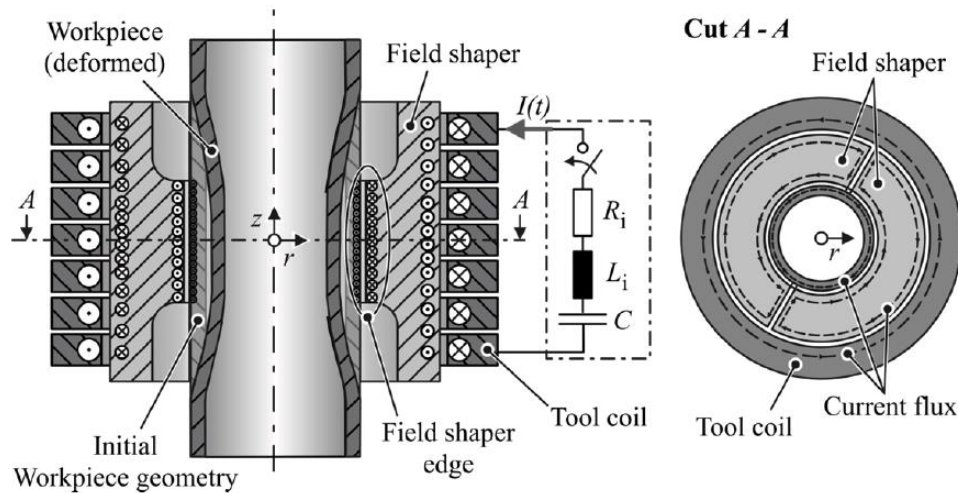


**Figure 7- Scheme of electromagnetic tube compression with a fieldshaper [13].**

When using a fieldshaper, as the high energy electrical discharge flows through the coil it induces eddy currents on the fieldshaper's outer surface. These superficial currents flow around this tool and reach the interior surface through a gap intentionally designed [13, 29]. As the inner surface is usually smaller than the outer one, an intensification of the magnetic field strength occurs, as eddy currents are generated once more but this time between the fieldshaper and the tubular workpiece [8, 29].

Besides the application of specific and concentrated magnetic fields, fieldshapers can provide a longer coil lifetime as this element creates stronger repulsive forces between it and the workpiece than between it and the tool coil [8, 13, 14, 20].

The use of a fieldshaper can bring several advantages to the electromagnetic forming process as well. The use of this kind of tool makes the EMPT process more flexible, as a generic coil can be complemented with a fieldshaper in order to produce parts that would otherwise need a coil with different characteristics (for example for forming small diameter tubes with coils designed to fit larger ones) [8, 13, 20, 21]

### 2.3.4 Form Defining Tools

Form defining tools are frequently used in order to end up with specific geometries that would not be achievable if the workpiece was not pressed against that specific die, for example when a free forming operation does not allow for the creation of the desired roundness of deformation. These tools can be used in all EMPT workpiece types: sheet metal or tubes (through compression or expansion) (Figure 8).

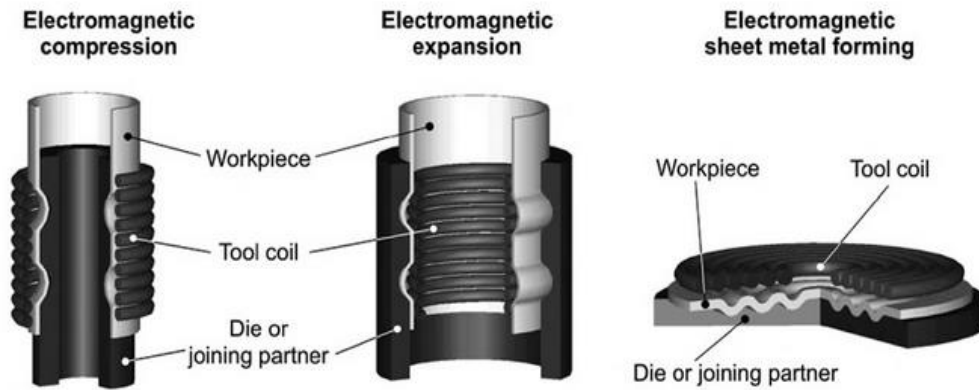


*Figure 8- Using form defining tools in EMPT [8].*

Focusing on tubular workpieces, the position of a form defining tool is related to the forming process being done: in the case EMPT by compression, this element (usually referred to as the mandrel) is located inside the tube in order to create the grooves intended; on the other hand, for expansion processes, the form defining tool is located on the outside surface so that a bulge is formed [6, 8].

If the objective of the forming process is to form the workpiece (instead of joining), magnetic forces imposed must take into consideration the fact that the form defining tool used must be removed from the workpiece. As such, the magnetic pressure limit is set by the force needed to extract the workpiece after forming. Other measures, besides the reduction in magnetic pressure that help reduce pull-out forces, include the use of lubrication, geometric adjustments, the material's choice or the use of pre-strained mandrels [6, 8].

## 2.4 Advantages and Disadvantages

When comparing the EMPT process with other more conventional metal forming methods, several advantages can be found. The most important ones are discussed in this chapter, along with the major negative aspects of this process.

The main advantages regarding the EMPT processes are the following:

- Due to the processes' high strain rates, the mechanical properties can be improved when compared to quasistatic forming conditions [8, 12]. The high strain rate can lead to an increased formability in some materials [22, 23, 30]. As an example of this phenomenon, aluminum sheet metal can be deformed about 100% without failure when formed at high strain rates, while the same material fails at 20 – 40% deformation when using conventional forming methods [12];
- The processing velocity also influences production rates and cycle times: these are influenced mainly by the machine preparation and setup (final product removal, new workpiece setup and charging time) [6, 8]. If these procedures are automated and optimized, output capacity can reach values of about 3600 operations/hour [8, 12];

- High strain rates allow the use of dies with simpler designs, as there is reduced springback at the end of the operation [6, 8, 26];
- Being a contact-free forming method means that a workpiece can be electromagnetically formed without damaging the cover or leaving tool imprints on the surface [6, 8, 12, 16]. Surface treatments such as anodizations are not damaged [8, 12]. This also means that no lubricants or special working mediums are required, making this method more environmentally friendly than regular metal forming by mechanical or hydraulic press, for example, while providing output parts of the same or better quality [8]. Clean room environments can be simulated by enclosing the workpiece in a non-electrical conductive material during the forming operations. Materials like glass and other ceramics or polymers are penetrated by the pulsed magnetic field and are not affected by the pulsed magnetic field, allowing the electromagnetic forming of environment sensitive materials [12];
- This process provides high repeatability, as the adjustment of the discharge energy and voltage and therefore pressure, is extremely accurate [12, 14].

However, this technology, just like any other, also has some drawbacks. The main process disadvantages are:

- Only materials characterized by a high conductivity and low flow stress can be formed by this method. Overcoming this disadvantage is possible by either adapting the discharge frequency or by using a driver foil: surrounding the workpiece with a high conductivity material (such as aluminum foil or annealed copper) intensifies the induced electrical flow in the workpiece, amplifying the forces between it and the coil [8];
- There are shape limitations for electromagnetically formed workpieces. Complex geometries and deep drawing are not easily achievable and there are size limitations to the workpieces formed [8, 12];
- This process is also known for being extremely inefficient when the capacitor bank charging energy and the effective energy used to form the metal workpiece are compared. Several reports state that this ratio can be somewhere between 2 and 20% [6, 8-10];
- Safety requirements are also a concern as this process involves electrical discharges of high current and voltage that result in strong magnetic fields [6, 8, 9, 12].

## 2.5 Joining by EMPT

Even though the technology's name (electromagnetic forming) may suggest otherwise, joining is actually the most common application. This method provides a unique way of joining similar or different materials without the use of additional fixation elements or using significant heat exchanges [7, 8, 31, 32]. When compared to the conventional joining methods (mechanical crimping and fastening, welding and adhesive bonding) the joints also achieve considerably more homogeneous characteristics due to the uniform application of the magnetic pressure [13, 19, 33].

For tube joining, electromagnetic forming provides a versatile method for manufacturing joints by interference fit, form fit or impact welded joint although the latter is not suitable

for joining metals to composites or polymers. The use of an adhesive can also be implemented to increase the strength of the connection [32-34].

Both tube compression and expansion can be used for joining processes involving metals and composites, but the first one is seen as the most viable method. This is due to limitations related to the mechanical strength of the coils used in electromagnetic expansion and their low lifetime [6, 8, 13, 14]. In Figure 9, an aircraft seat with metal-polymer joint performed by EMPT is shown.

Joining by electromagnetic forming has revealed especially interesting in the field of joining lightweight materials by tube compression as joint strengths can sometimes exceed the tube's tensile strength [28].



**Figure 9- EMPT crimping applied to join dissimilar materials (polymer-metal) in lightweight aircraft seats [19].**

In general, two types of joints can be achieved with the use of the EMPT: interference-fit and form-fit joints [13].

### 2.5.1 Interference-Fit Joints

Interference-fit or force-fit joints rely on a difference in the elastic recovery of the two workpieces being joined together [13].

This method is described in Figure 10 for both electromagnetic compression and expansion. When radial magnetic pressure is applied to the metallic tube (A), it is deformed until it touches the mandrel (B). Deformation proceeds, with workpiece A being elastic-plastically deformed and workpiece B being purely elastically deformed. After the end of the magnetic pressure application, both parts recover elastically but due to the higher elastic strain of workpiece B, the parts do not recover completely and therefore an interference pressure is created between the two workpieces.

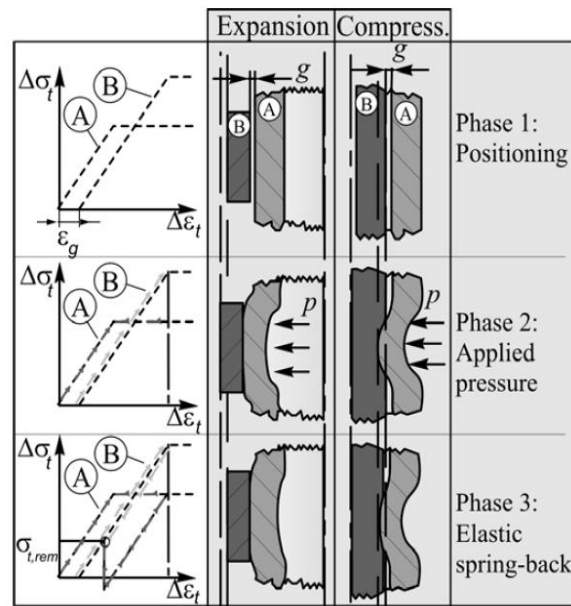


**Figure 10- Interference-fit joining process description [28].**

The gap between the joining partners in phase 1 of Figure 10 is also an important parameter in this process as it influences the strength of the joint as well [8]. During the electric pulse, the workpiece is accelerated until it reaches a maximum speed and then decelerates. In order to fully take advantage of the maximum energy, the gap should be chosen in a way that allows for the maximum workpiece velocity to be reached [26, 27, 30].

The strength of this joint depends on the interference pressure, the coefficient of friction and the area of the joining zone [8, 13]. With this in mind, the strength of these types of joints can be increased by increasing the electrical discharge intensity (resulting in an increased interference pressure), by increasing the length of the joint (which requires a larger coil) or by increasing the coefficient of friction, the latter being the most effective way to increase joint strength. Machined mandrels such as the ones in Figure 11 have shown higher joint strength than plain mandrels for the same process parameters [35].



**Figure 11- Examples of machined surfaces compatible with EMPT tube joining by interference-fit. a) and b) knurled surfaces; c) screw thread with axial grooves; d) screw thread [35].**

### 2.5.2 Form-Fit Joints

Form-fit connections imply that one of the joining partners, the mandrel in the case of joining by compression, has additional geometric elements such as grooves. During the

tube deformation, the tube is formed in such a way that it adapts to these features so that the joint is fixed against an external load (Figure 12). This process typically provides stronger joints when compared to interference-fit joints made by EMPT [13, 26, 27, 31].

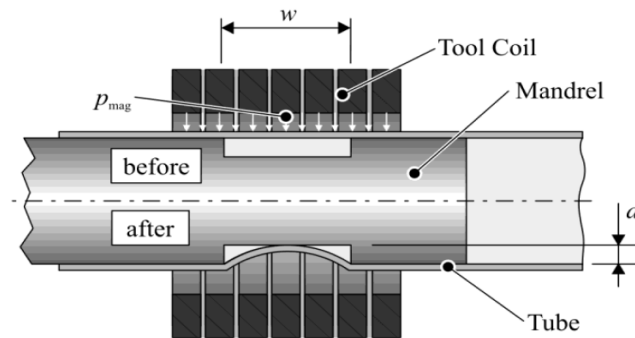


Figure 12- Representation of the joining by form-fit process [36].

### 2.5.2.1 Review on Form-Fit Joints

Axial joints are most commonly composed by one or more circumferential grooves as these provide locking mechanisms against the slipping of the joining components. Different groove geometries can be applied (Figure 13) [13].

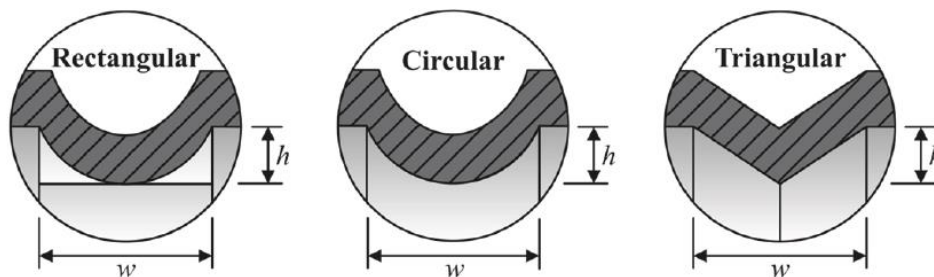


Figure 13- Applicable groove shapes for electromagnetic form-fit joints [13].

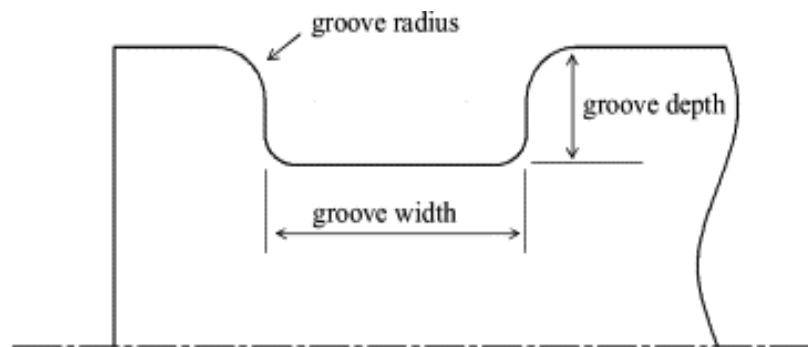


Figure 14- Geometric groove parameters affecting joint strength using rectangular grooves [34].

Since the first developments of this technology, many authors have investigated the behaviour of form-fit joints by EMPT as well as the influence of the mandrel's geometric parameters (Figure 14). Bühler et al. [37] have investigated the influence of the rectangular groove's geometry in the joint strength of EMPT joints. By varying the groove width and depth and adjusting the electromagnetic pressure (in order to achieve a joint where that

simply touched the groove bottom), results showed that an increase in depth and a decrease in width of the grooves influences joint strength positively [8, 36].

Park et al. [34] also studied the groove's geometric influence in the joint strength, focusing on groove depth, width but also on the radius at the edges. Besides the characterization of the radius, Park's research differed from Bühler's in the way that groove parameters were altered without adjusting the magnetic pressure, resulting in different contact areas in the bottom of the groove for different geometric parameters. The results matched the ones obtained three decades earlier regarding groove depth, although excessive depths lead to a decrease in joint strength because of localized thinning of the tube walls at the edges. It was also discovered that an increase in groove width which promoted a larger contact area, lead to an increase in joint strength due to the appearance of interference-fit related stresses at the bottom of the groove; however, an excessive increase causes a wrinkling effect that negatively influences joint strength. Regarding the groove radius, Park et al. [34] discovered that smaller radius lead to higher joint strength, however there is a lower radius limit below which there is an increase in shearing effects at the groove edge. Additionally, both researches have shown that it is possible to further increase a joint's strength by using multiple grooves instead of just one [36].

Weddeling et al. [36] also performed extensive research and testing regarding the influence of groove geometry in axial metal-metal joints. His work focuses all relevant aspects to the production of form-fit joints. Unlike previously mentioned work that only focused on the groove shape and dimensions, it covers the relationship between the charging energy and the joint's tensile strength as well (Figure 15. Two failure modes were observed during the tensile tests of the joints: pull-out of the tube from the mandrel and tube breakage over the groove edge (Figure 16). These failure modes were associated with the parameters being evaluated and are represented in the plots as unfilled marks for failure by tube pull-out and filled marks for failure by tube tearing [36].

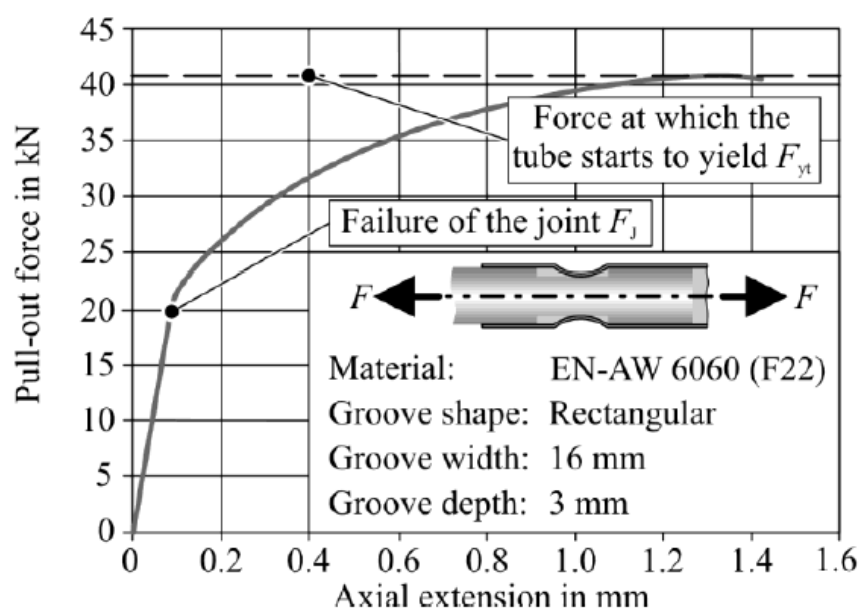


Figure 15- Example of load-extension curve plotted by Weddeling. Joint failure occurs at  $F_j$ , where there is the first relative movement between the tube and mandrel [36].

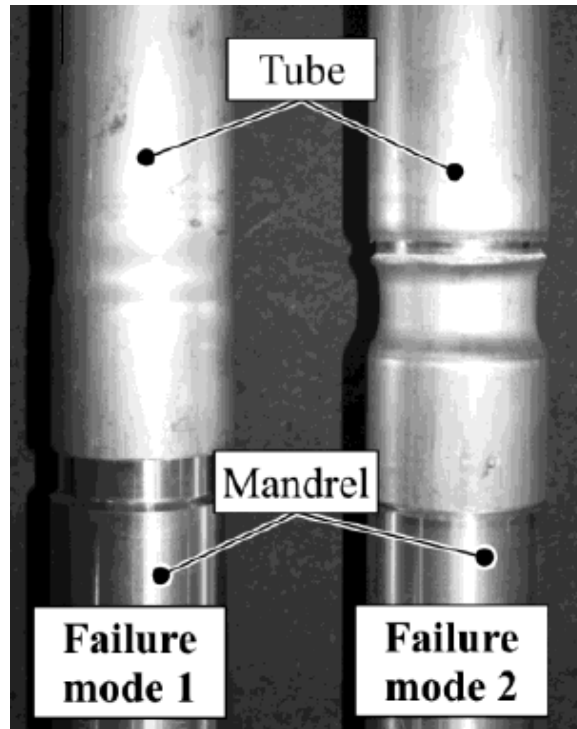


Figure 16- Failure modes observed in Weddeling's work. On the left, failure by tube/mandrel pull-out; on the right, tube shearing [36].

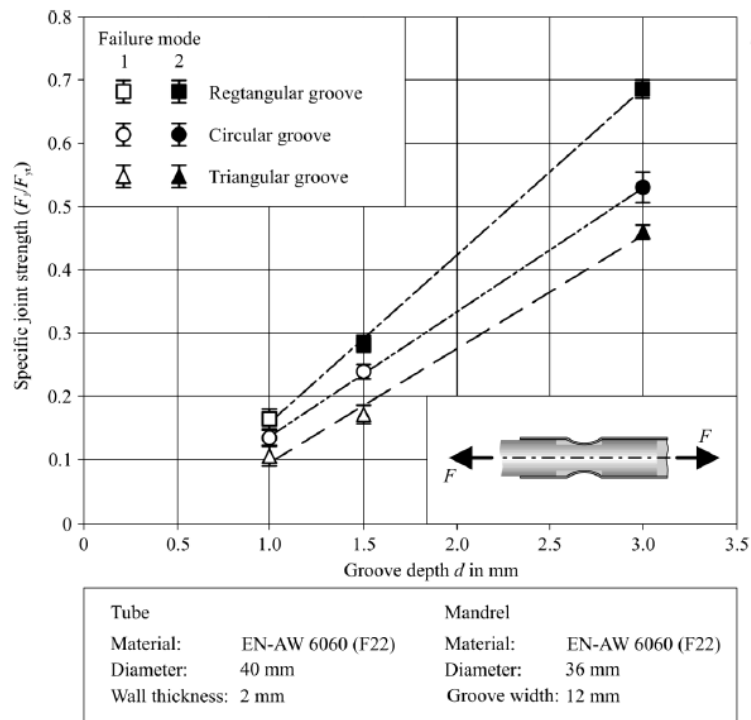


Figure 17- Relationship between pull-out force and groove shape [36].

When evaluating the different groove shapes, Weddeling et al. [36] verify that for each shape, increasing depth increases joint strength in a linear way. It also shows that no matter what, rectangular shapes always provide higher joint strength, while triangular grooves provide the weakest connections (Figure 17). This is considered to be due to the shearing and necking formed at the groove edge for this configuration that locks the

components together. On the other hand, the triangular grooves are always found to be the weakest: for this groove type the angle  $\alpha$  is bigger and therefore the tube is prone to deform considerably less, resulting in lower joint strength (Figure 18) [36, 38].

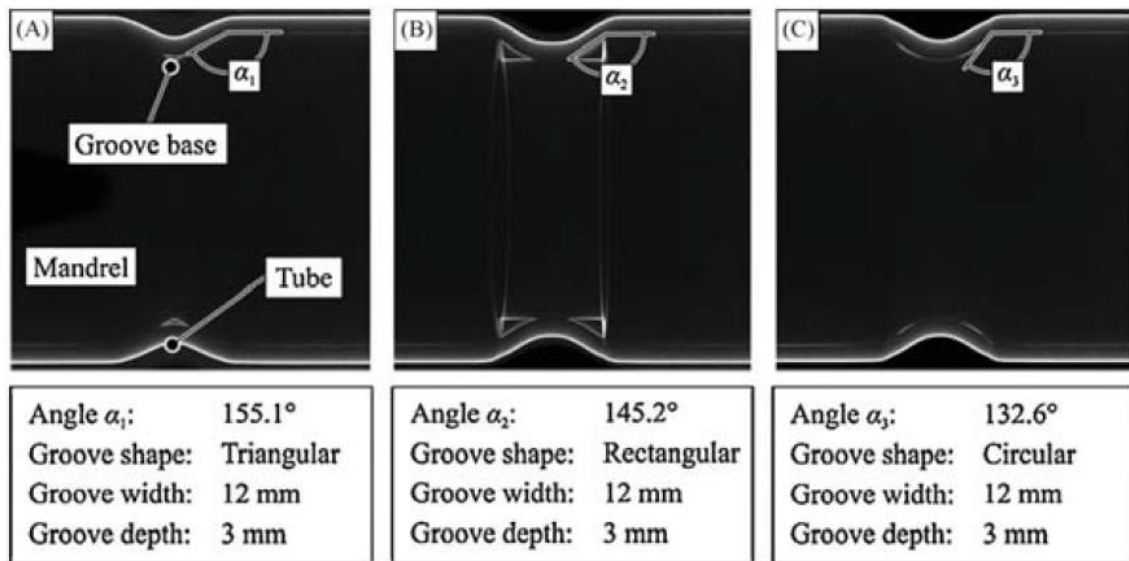


Figure 18- Radioscopic pictures of axial joints with different shapes [36].

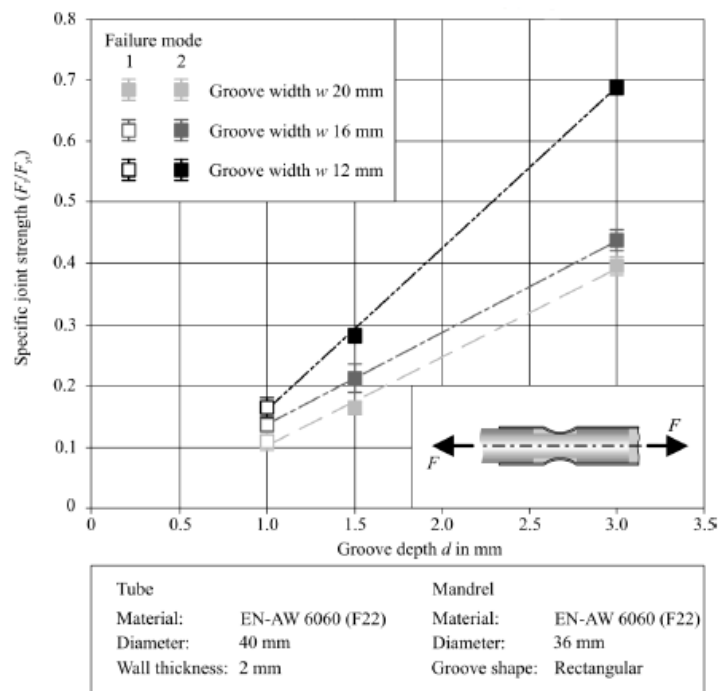


Figure 19- Relationship between pull-out force and groove dimensions [36].

The result distribution obtained by Weddeling et al. [36] for the influence of a rectangular groove’s dimensions (Figure 19) shows a clear relationship between groove dimensions and the joint’s ultimate force, where deeper and/or narrower grooves provide higher strength just like the previous researches had shown. This could be due to the fact that bigger deformation is needed to fill such a deep, “aggressive” feature, resulting in higher stiffness at the groove. The radioscopic images obtained (Figure 20) provide a visual representation of the variation of  $\alpha$  with depth. The use of deeper grooves assures a lower angle  $\alpha$  which

increases the degree of deformation of the outer tube at the groove edge, locking the two pieces together more firmly. Although it may seem that one could increase joint strength by increasing depth, it should be taken into consideration that shearing at the groove edge can occur if the deformation is excessive and, therefore, there is an upper limit where increased depth no longer leads to an increased joint strength.

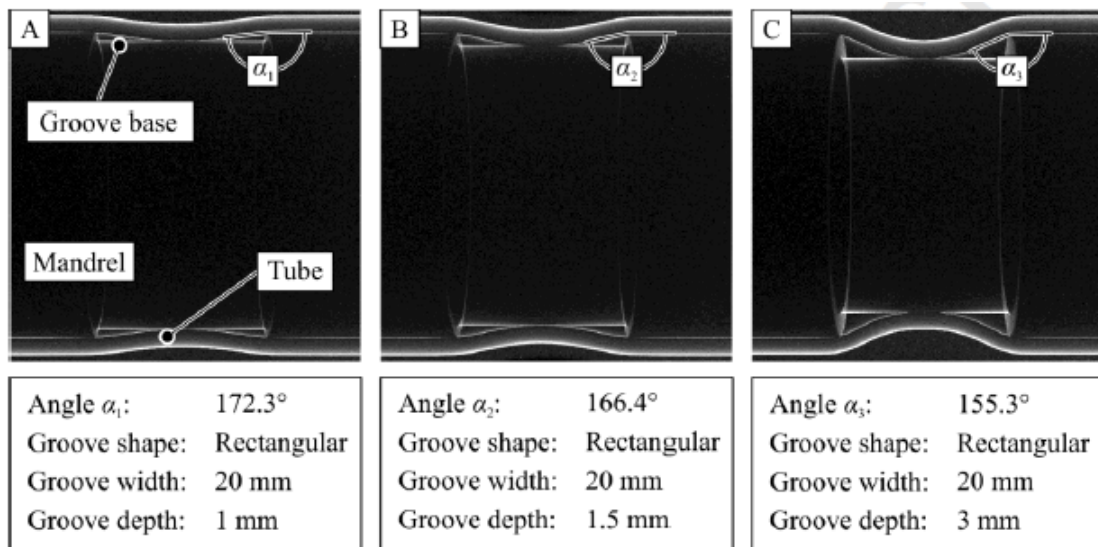


Figure 20- Radioscopic images of rectangular grooves with different depths. The relation between depth and angle  $\alpha$  and between depth and deformation degree is visible [36].

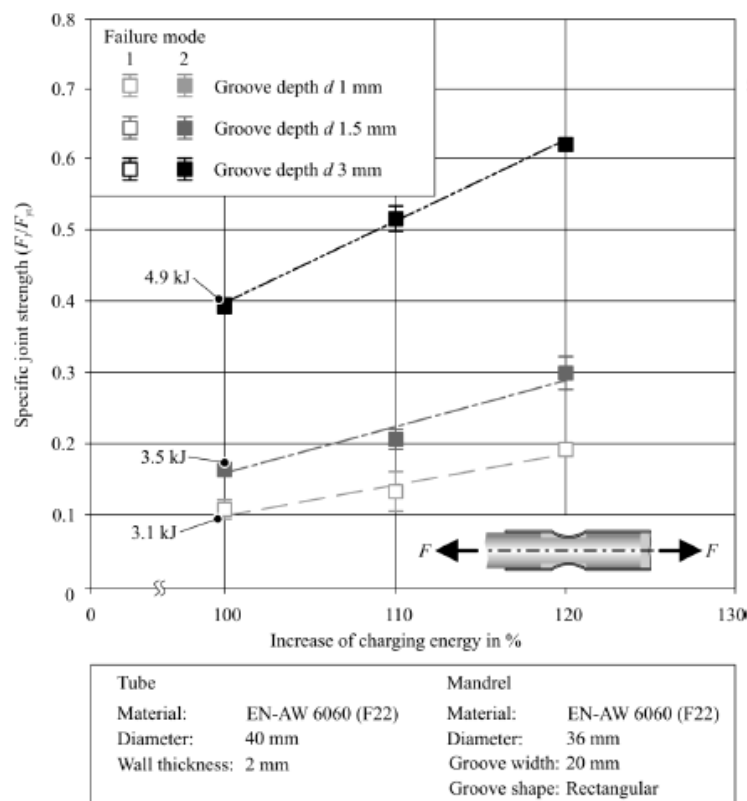


Figure 21- Relationship between pull-out force and charging energy for various groove depths [36].

As expected, the results for the pull-out force vs. charging energy show that for each groove design, an increase of the charging energy (which was at first calculated so that the

deformed tube only touched the groove bottom) linearly increases the strength of the joint in this range of values (Figure 21). The energy increase creates a larger contact surface between the deformed tube and the mandrel and increases joint strength by adding a component related to an interference-fit inside the groove. Higher forming energies also decrease the angle  $\alpha$ , as it is shown in Figure 22.

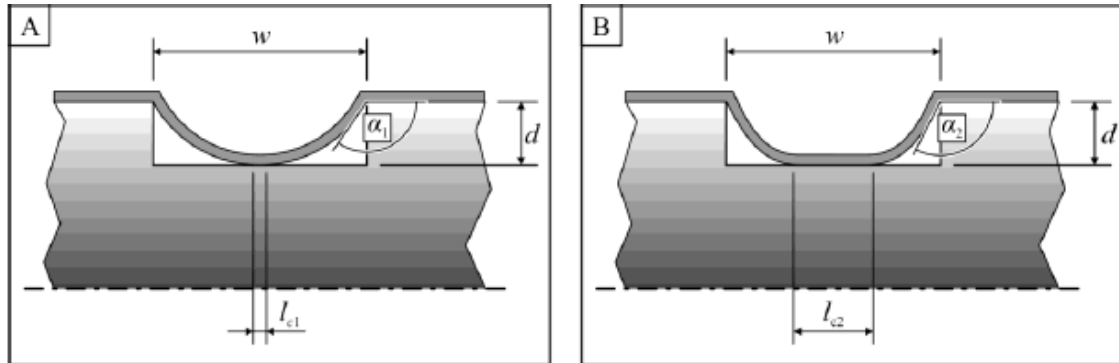


Figure 22- Influence of the magnetic pressure in filling the grooves [36].

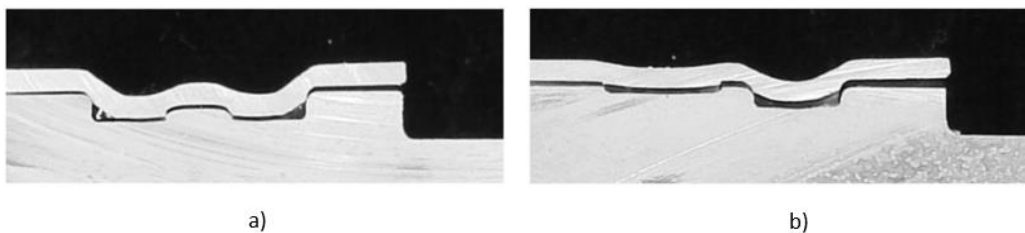


Figure 23 - Cut-view of a double groove form-fit axial joint [38].

This investigation also shows that the charging energy and depth strongly influence how the joint fails under loading: deeper and/or narrower gaps formed with higher forming energies tend to fail by tube shearing. This is due to the fact that the use of higher magnetic pressures increases shearing effects at the edge of the grooves, which locally reduces the tube's stiffness [36].

Additionally, both researches have shown that it is possible to further increase a joint's strength by using multiple grooves instead of just one such as in Figure 23 [34, 36]. Vanhulsel et al. [38] and Faes et al. [39] examine the influence of the second groove and optimize this geometry in terms of groove filling and torque resistance, concluding that this change positively influences the performance of axial form-fit joints.

### 2.5.2.2 Design of Torque Form-Fit Joints

The design of torque joints is similar to the design of axial joints except the loads act in the circumferential direction, twisting the joint. The pocket's main geometric parameters to take into consideration are the groove length in the axial direction and the number of grooves around the mandrel although the groove's width, depth, and edge radius (Figure 24). Park et al. [34] conclude several relation between geometrical parameters and torque strength: an increase in groove width and depth positively influences the joint's resistance until a certain degree [34, 40].

Bogaert et al. [40] discuss the influence of each groove parameter:

- Groove edge radius can be defined according to the two extreme situations: when an edge radius is too small, excessive necking may occur, along with thinning of the tube, decreasing joint strength; on the other hand, a too large groove radius may allow for the tube to easily slip out of the groove. It is also assumed that as this parameter influences the joint less in torsional cases than in axial cases, so a lower radius can be reached;
- A deeper groove is able to lock the workpieces together more firmly, as more deformation occurs at the tube. However, an excessive depth may lead to severe necking at the groove's edges;
- An increase in groove length creates larger contact areas between mandrel and tube, resulting in more frictional force and therefore joint strength;
- Groove width behaves like the length parameter in the way that increased strength is observed with increased width.

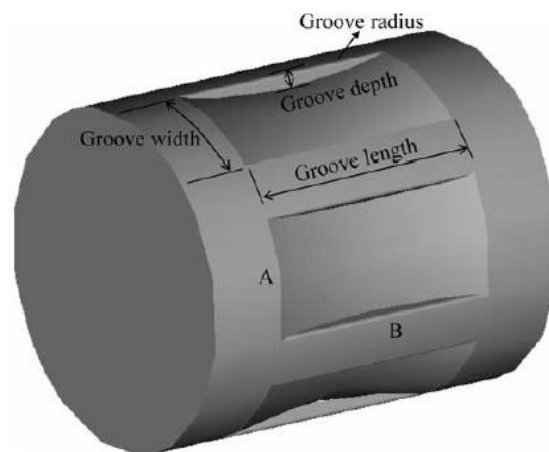


**Figure 24- Example of the sockets used for form-fit connections using EMPT [34].**

One of the main aspects to take into consideration when designing this type of joints relates to the fact that increasing joint strength by increasing the pocket's length influences the structure's weight and cost negatively, as a larger overlapping area must be created leading to the use of more material. Thus an effort has to be made in order to minimize groove length without compromising the joint's integrity [34].

Groove width must be taken into consideration as well and minimized as it the most influencing factor when determining the number of grooves that can be machined onto a mandrel. However, creating pockets that are too narrow in order to maximize the number of pockets is useless, as there must be space for the tube material to flow and adapt to the groove [32, 41].

In [41], Faes et al. analyze the effect of the number of axial grooves in the resistance of the joint. They test similar crimp connections with internal mandrels with longitudinal grooves,

differing in the number of said grooves. They prove the almost linear relation between joint strength and number of grooves expected.

## **2.6 Summary and Outlook**

In this chapter, a bibliographical review is presented in order to introduce the electromagnetic pulse technology. First, the basic principles of this technology and its most important applications are presented. The equivalent RLC circuit is analyzed as well as the equipment that is commonly used in the process. After comparing the EMPT with conventional tube joining techniques, the process's advantages and disadvantages are reviewed. Finally, a review focused on the use of the EMPT in the joining process of tubes is presented, along with the analysis of several experimental reports that provide crucial information regarding the main process and geometrical parameters that influence the behavior of force and form-fit joints manufactured by the EMPT.

The fact that there is little literature in the field of hybrid joints involving metals and fiber reinforced polymers, makes this dissertation one of the pioneers in the study of the behavior of electromagnetically crimped joints.

## 3 DESIGN OF FORM-FIT JOINTS

---

Taking into consideration the literature review regarding form-fit joints performed in the previous chapter, the process of joint design is now explained and fundamented. A set of design rules is presented for the production of viable tube connections.

In order to study the applicability of the EMPT for the form-fit joining of metal-composite tubes, three joint designs are later proposed.

### 3.1 Considerations for the Geometric Parameter's

Considering previous experiments and simulations developed throughout the last decades, some guidelines towards optimal form-fit designs can be specified [34, 38, 39, 41, 42].

#### Groove Depth ( $d$ )

Groove depth should be such that provides full groove penetration (i.e. at least the tube thickness ( $t$ )). On the other hand, excessive deformation may cause wrinkles or excessive shearing at the groove edges. According to the literature review, the optimal groove depth is given by the relation:

$$t \leq d \leq 0.05 \cdot D \quad (3.1)$$

where  $t$  is the tube's wall thickness and  $D$  is the average tube diameter [34, 41].

#### Groove Radius ( $r$ )

According to the difference in influence of the groove edge radii when comparing axial and torque joints, it is inferred that torque joints allow the use of smaller edge radii than axial joints [41]. A value of  $0.5 \cdot t$  for torque joints and  $t$  for axial joints is considered a valid guideline to design this feature. In [34, 41], the parameter relation for defining groove edge radius is given as:

$$t \leq r \leq \begin{cases} 0.5 \cdot d \\ \min(t, 0.5 \cdot d) \end{cases} \quad (3.2)$$

### Groove Width ( $w$ )

Groove width has different geometric significance in both axial and torque joints.

In axial joints, it represents the groove size in the axial dimension. For its correct design, it must be as small as possible (in order to reduce the overlapping zone, thus reducing weight), without influencing the proper material flow inside the groove and remembering that wider grooves promote higher joint strengths.

In torque joints, the width basically determines the number of grooves admissible around the tube. In both circumstances, a minimum width of 3 to 4 times the depth of the groove is advised [38, 42].

### Groove Length ( $l$ )

Groove length relates only to torque joints and it is the dimension of the groove measured in the axial direction. Although it is one of the parameters that influences the joint's strength, along with the number of grooves around the mandrel, it should be minimized for the same reasons that width in axial grooves is minimized.

## 3.2 Definition of the Geometric Parameters

According to the guidelines established in the last sub-chapter and taking into consideration the experiments developed by MetalMorphosis [43], the mandrel's dimensions can be calculated.

### Groove Depth:

Considering that  $t = 1 \text{ mm}$  and  $D = 19.5 \text{ mm}$ :

$$t \leq d \leq 0.05 \cdot D \Leftrightarrow 1 \text{ mm} \leq d \leq 1 \text{ mm} \quad (3.3)$$

The calculation above suggests 1 mm for the optimal groove depth. However, 1.5 mm was chosen for the effective depth. This provided extra space for the aluminum tube deformation, as the tube's thickness itself is 1 mm. This parameter is used for both axial and circumferential grooves.

### Groove Edge Radius:

- Axial component:

$$t \leq r \leq 0.5 \cdot d \Leftrightarrow 1 \text{ mm} \leq r \leq 0.5 \text{ mm} \quad (3.4)$$

- Torque component:

$$0.5 \cdot t \leq r \leq \begin{cases} 0.5 \cdot d \\ \min(t, 0.5 \cdot d) \end{cases} \Leftrightarrow 0.5 \text{ mm} \leq r \leq \begin{cases} 0.5 \text{ mm} \\ \min(1 \text{ mm}, 0.5 \text{ mm}) \end{cases} \quad (3.5)$$

According to the relations above and considering that axial joints require a higher value, the groove edge radii for axial and torque components are 1 and 0.5 mm respectively.

**Groove Width:**

$$w \geq 3 \cdot d \Leftrightarrow w \geq 3 \text{ mm} \quad (3.6)$$

The guidelines for groove design advise that for this mandrel, groove width should be above 3 mm.

**Groove Length:**

Groove length in the axial direction is limited by the maximum length of the coil. The active surface of the coil is 12 mm long, which should be reduced considering the properties of the transient magnetic pressure applied at the edges of the coil. Therefore, an attempt is made to keep the total groove length in the axial direction under 10 mm.

### 3.3 Joint Designs

The joint design process originated five mandrel designs, three of which showing special relevance to this work. Only the used designs will be mentioned in this chapter, while the others will be referenced in the chapter regarding Future Work. 2D drawings of these designs are featured in the Annexes section of this dissertation.

#### 3.3.1 Joint 1

The first joint designed is the simplest and features a single radial groove to provide axial resistance. It will be used mainly for comparison purposes as it is expected that the other joint designs will exceed this joint's strength. The figures below are a SolidWorks model of the first mandrel design.

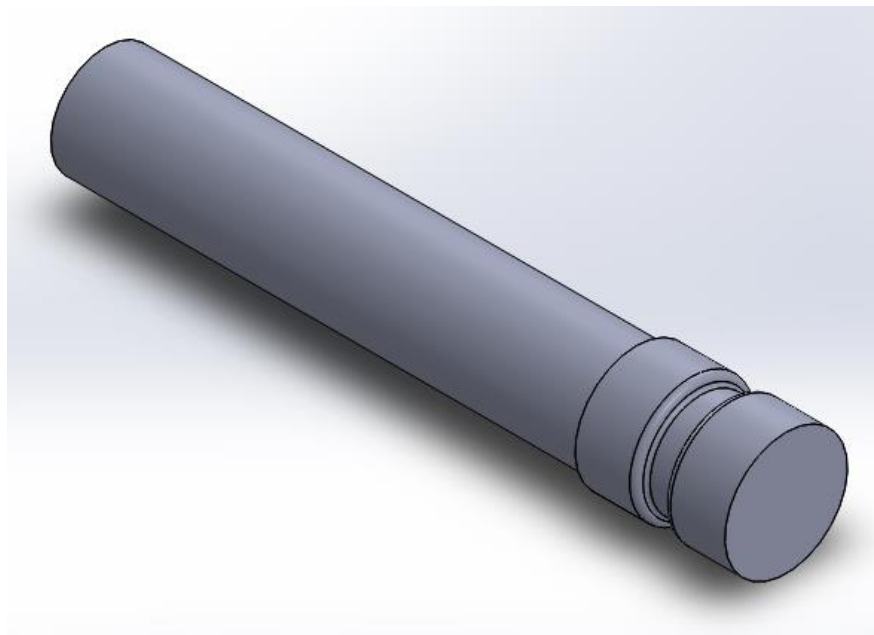


*Figure 25 - Isometric view of joint 1 (from SolidWorks).*

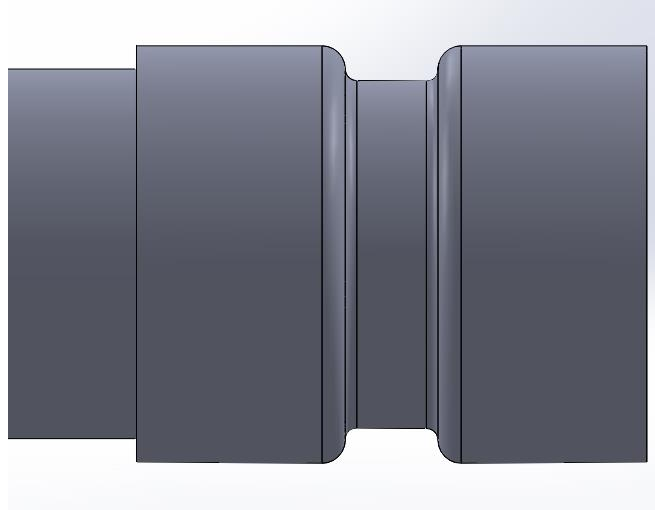


*Figure 26 - Side view of joint 1 (from SolidWorks).*

Joint 1 features a single groove with 1.5 mm in depth and 4.5 mm in width. The top groove edge radius is 1 mm while the bottom one is 0.5 mm (Table 1 - Dimensions chosen for joint 1.). This geometry is based on the guidelines proposed in the last chapter.

*Table 1 - Dimensions chosen for joint 1.*

<b>Groove Depth (mm)</b>	1.5
<b>Groove Width (mm)</b>	4.5
<b>Groove Edge Radii – Top (mm)</b>	1
<b>Groove Edge Radii – Bottom (mm)</b>	0.5

### 3.3.2 Joint 2

The second groove geometry defined features two radial grooves as proposed in [34, 41] (Figure 27 and Figure 28). A scale of 2:1 was implemented between the first and second grooves' depth and width as this helps to distribute the stresses between both grooves. The first two joints are manufactured exclusively through the use of a lathe. Groove dimensions for this joint can be seen in Table 2.

*Table 2 – Dimensions chosen for joint 2.*

	<b>Deep groove</b>	<b>Shallow groove</b>
<b>Groove Edge Radii (mm)</b>	1	1
<b>Groove Depth (mm)</b>	2	1
<b>Groove Width (mm)</b>	6	3

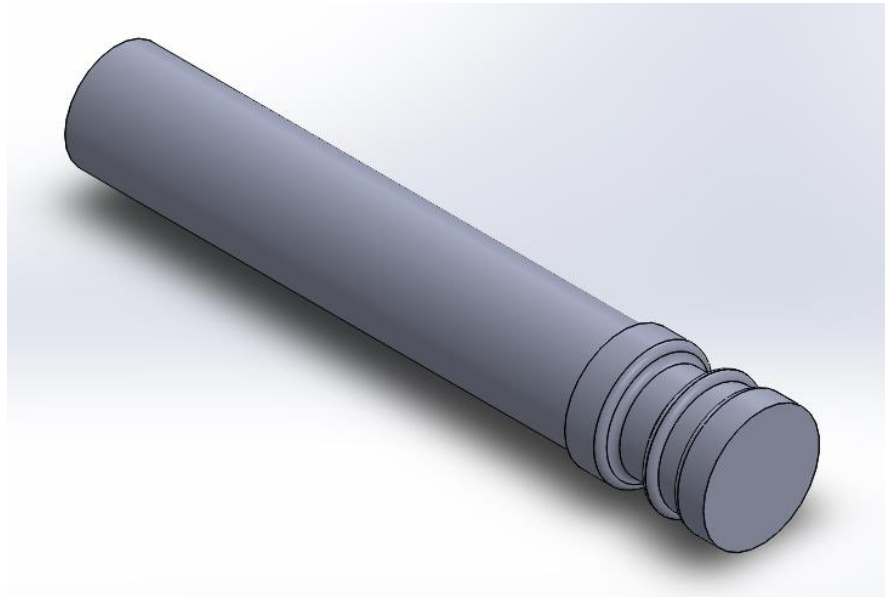


*Figure 27 - Isometric view of joint 2 (from SolidWorks).*

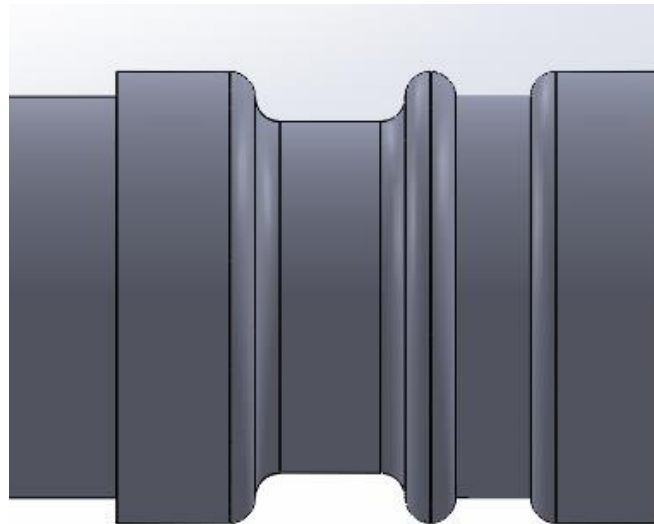


*Figure 28 - Side view of joint 2 (from SolidWorks).*

### 3.3.3 Joint 3

Joint 3 features both longitudinal and radial slots as it is designed for both axial and torsional solicitations as shown in Figure 29 and Figure 30. The mandrel's grooves are designed in such a way that axial and torque grooves are separated.

Both tensile and torque tests were intended for this joint. However, torque tests could not be performed. This joint is used to analyze the formability into axial and radial grooves as well as the influence of extra geometric features in the tensile behaviour of the form-fit joints.

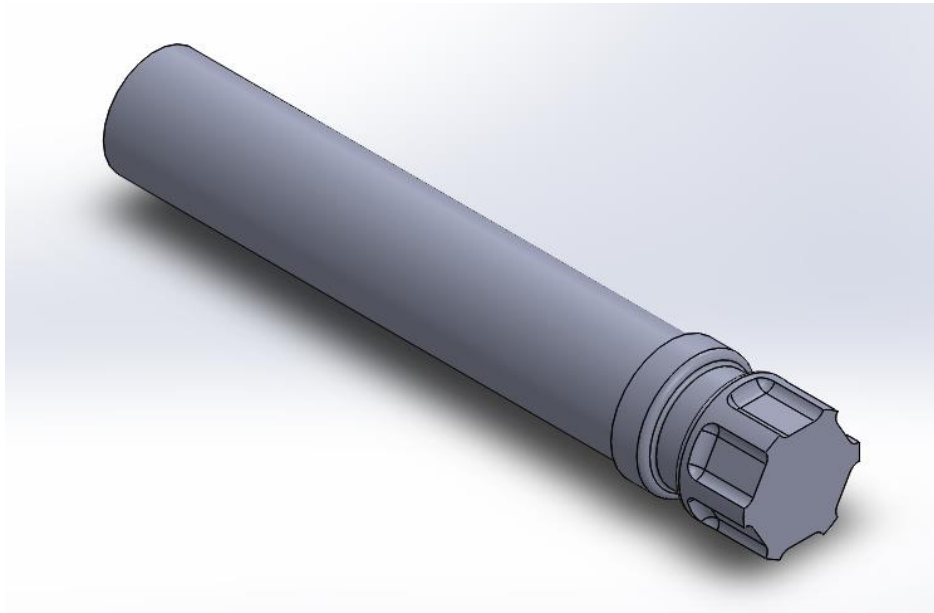


*Figure 29 - Isometric view of joint 3 (from SolidWorks).*

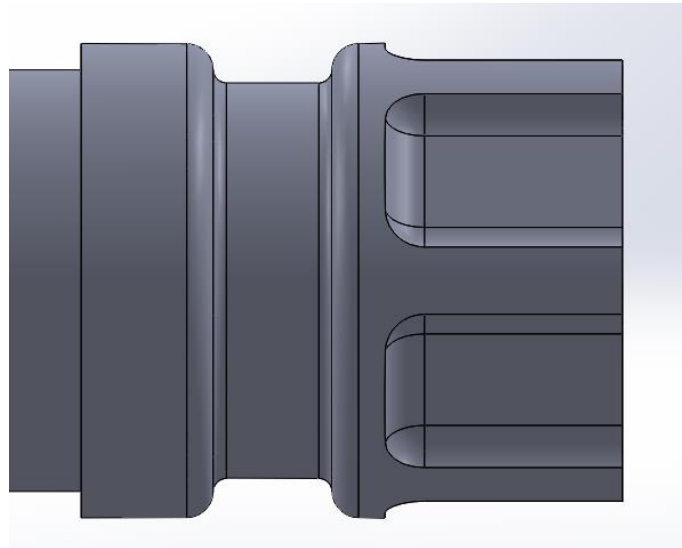


*Figure 30 - Side view of joint 3 (from SolidWorks).*

The radial groove is designed using the same dimensions as Joint 1 (Table 3): 1.5 mm deep, 4.5 mm wide and with top and bottom groove radii of 1 and 0.5 mm respectively. The axial groove is 1.5 mm deep as well. The axial grooves are designed to be machined using a ball nose milling tool with 3 mm diameter, which was a manufacturer's demand. Six slots are designed so that they do not affect each other.

*Table 3 - Dimensions chosen for joint 3.*

	Radial groove	Axial groove
Groove Edge Radii – Top/Bottom (mm)	1/0.5	0/1.5
Groove Depth (mm)	1.5	1.5
Groove Width (mm)	4.5	9

# 4 EXPERIMENTAL PROCEDURE

---

This chapter describes the materials, equipment and methodology used for the production and evaluation of form-fit joints between metal and composite tubes.

## 4.1 Materials and Experimental Setup

### 4.1.1 Materials

The tube is made of the aluminum alloy EN AW 6082. It is known as a structural alloy and it is the strongest of all the 6000 series aluminums [44, 45]. The increased strength is due to the grain structure resulting from the addition of manganese [46]. It is typically used in high stressed applications, structures such as bridges or cranes and in the transportation industry [45]. A material datasheet for this aluminum alloy is present in Annex 4 [47]. For each sample, 1 mm thickness and 20 mm outer diameter tube with 100 mm length was used.

The material chosen for the composite mandrel is PolyLanema's Ertalon® 66-GF30, a short glass-fiber reinforced polyamide. Compared to virgin polyamide 6.6, this reinforced version with 30 % mass fraction of short and randomly oriented glass fibers, offers greater mechanical strength, stiffness, creep and fatigue resistance and dimensional stability [48]. It is also characterized by good machinability as well as for being a good electrical insulator [49]. A material datasheet for this fiber reinforced polymer is presented in Annex 5 [50].

### 4.1.2 EMPT Machine

The magnetic pulse system (Figure 31) used in the experiments is defined with the set of characteristics presented in Table 4.

*Table 4 - Electromagnetic pulse machine's specifications.*

Specification	Value
Max. stored energy	25 kJ
Max. discharge voltage	25 kV
Max. output current	400 kA
Capacitance	80 $\mu$ F
Resistance	19 m $\Omega$
Inductance	0.1 $\mu$ H



**Figure 31 - EMPT system used for the experimental procedures [51].**

#### 4.1.3 Coil and Workpiece Setup

The experimental setup is represented in Figure 32. As mentioned before, a single-turn coil was used for the experimental tests. It was machined from 40 CrMnNiMo 7 steel and its most relevant characteristics for the experiment are presented in Table 5.

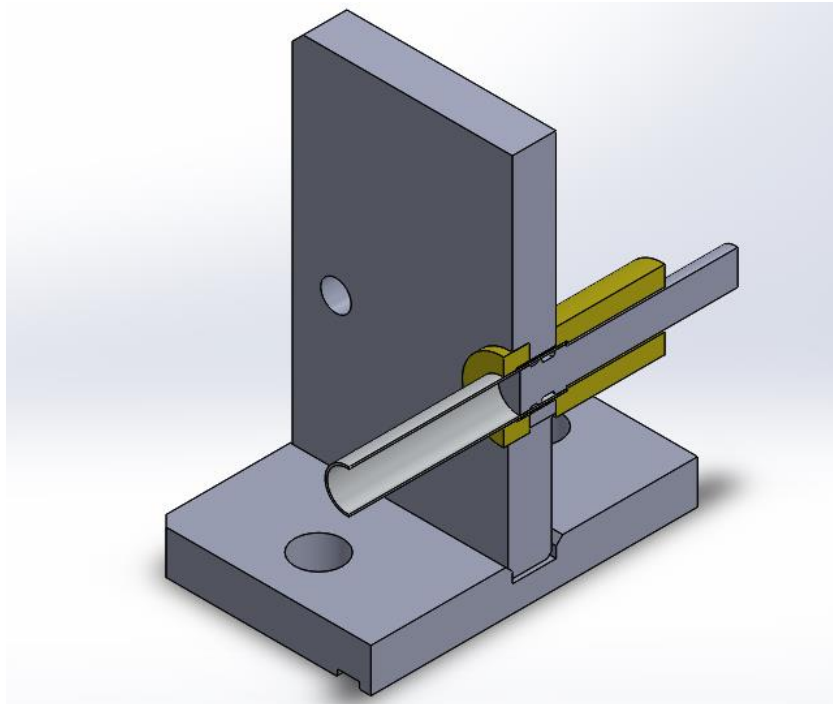


**Figure 32 – Cut-view of the SolidWorks model for the coil and workpieces assembly.**

**Table 5 - Electrical and geometrical properties of the coil.**

<b>Material</b>	Steel 40 CrMnNiMo 7
<b>Electrical conductivity</b>	2 MS/m
<b>Diameter</b>	21.42 mm
<b>Active length</b>	12 mm

Two extra pieces (represented in yellow in Figure 32) are made of an electrical insulating polymer and are used to position and constraint the workpieces. The positioning of the tube is straightforward, as it slides until hitting the right-hand side component. The positioning of the mandrel is performed by a third component that slides into the tube and acts as a stopper for the composite bar (Figure 33). This stopper has a specific length in order to align the center of the groove with the center of the coil's active zone.

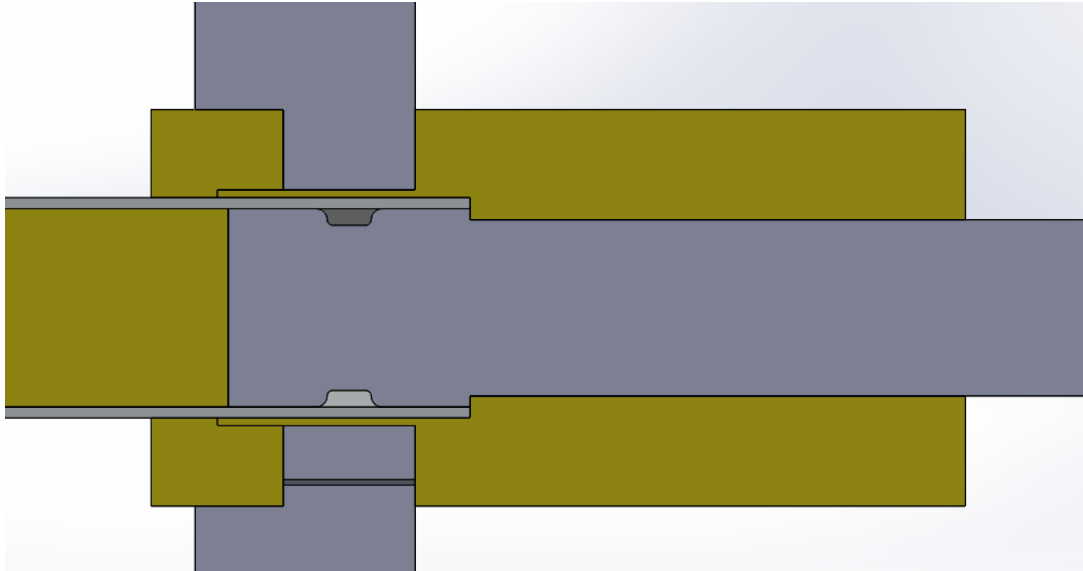


*Figure 33 - Detail of the positioning and constraining system.*

**NOTE 1:**

The tube-mandrel overlapping zone of the composite mandrel has an 18 mm diameter, the following section was designed with 16 mm diameter in account of the already existing positioning system of the EMPT coil. The schematic SolidWorks assembly shown in Figure 34 presents the experimental setup for joint 1 in cut-view.

However, when the mandrels were received after the machining operations, none of the designs featured the previously mentioned feature that allowed for the proper assembly of the components. Faced with said inconvenient, the positioning system had to be redesigned to accommodate the defective mandrels. Figure 34 presents the adapted positioning system, with changes to the right-side support, increasing from an inside diameter of 16 mm to 18 mm.

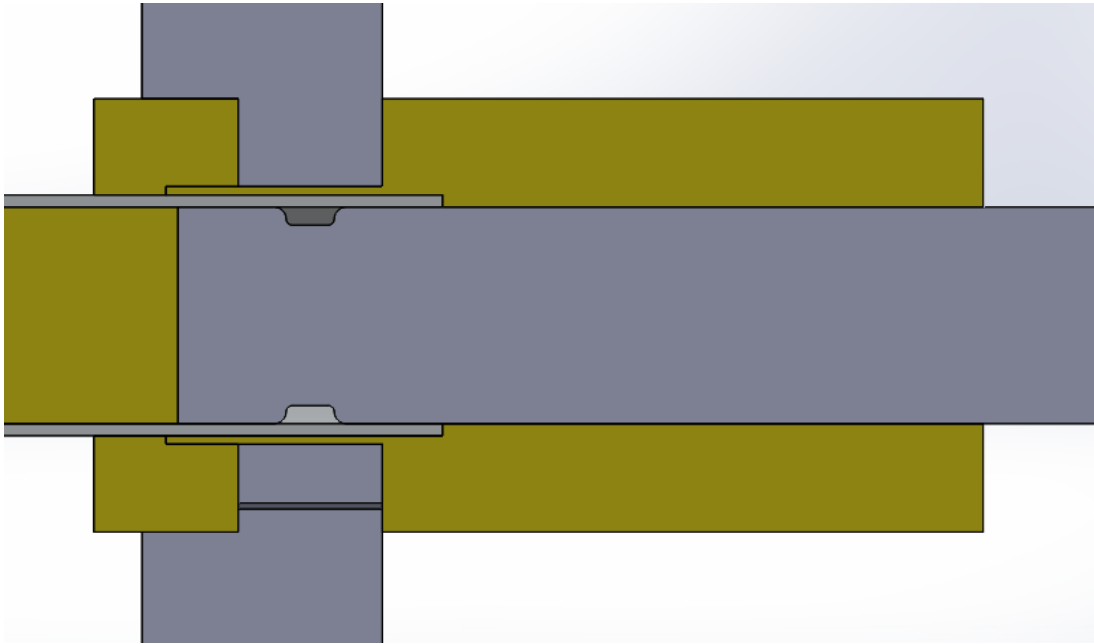


*Figure 34 - Detail of the adapted positioning system.*

NOTE 2:

Due to the geometry intended for joint 2, the total length of its features exceeds the coil's length by 1 mm. Not much importance was given to this since the non-overlapping area is limited to 0.5 mm on the edge radii of each extremity of the feature. It is expected that inertial forces will drag the tube portion unaffected by the magnetic pressure. A cut view featuring the overlapping is shown in Figure 35.

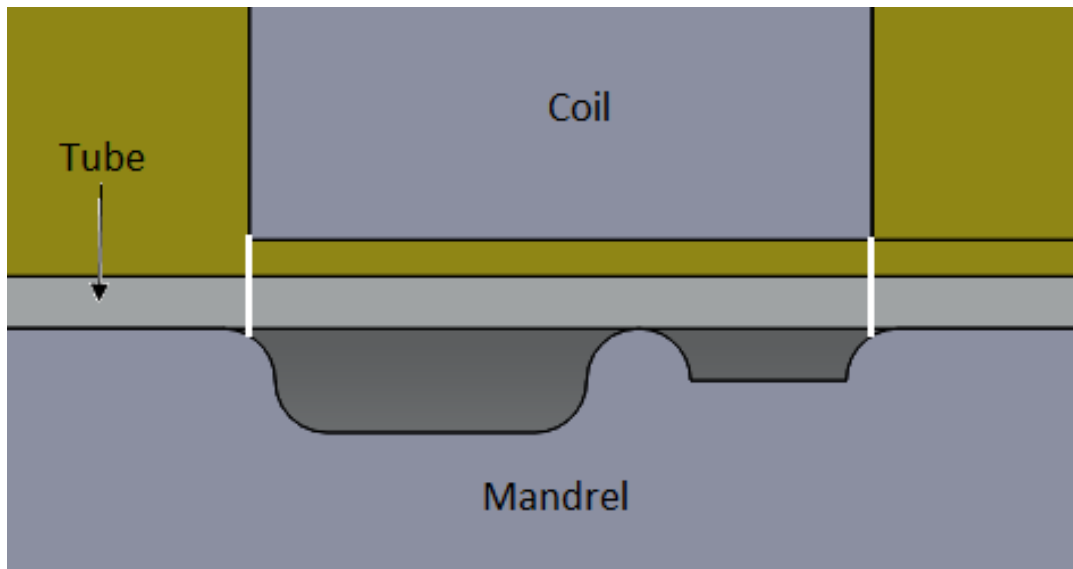


*Figure 35 - Cut view of the coil-groove overlapping area (SolidWorks).*

## 4.2 Design of the Experiment

Since little or no experiments such as these have been performed between a metal tube and a composite mandrel, preliminary tests were executed. These tests allowed to set maximum discharge energy to use to prevent damage to the composite. In this sense, two specimens of joint 2 were used in the EMPT joining process with 14 kV and 16 kV. Figure 36 presents the end result of said tests.

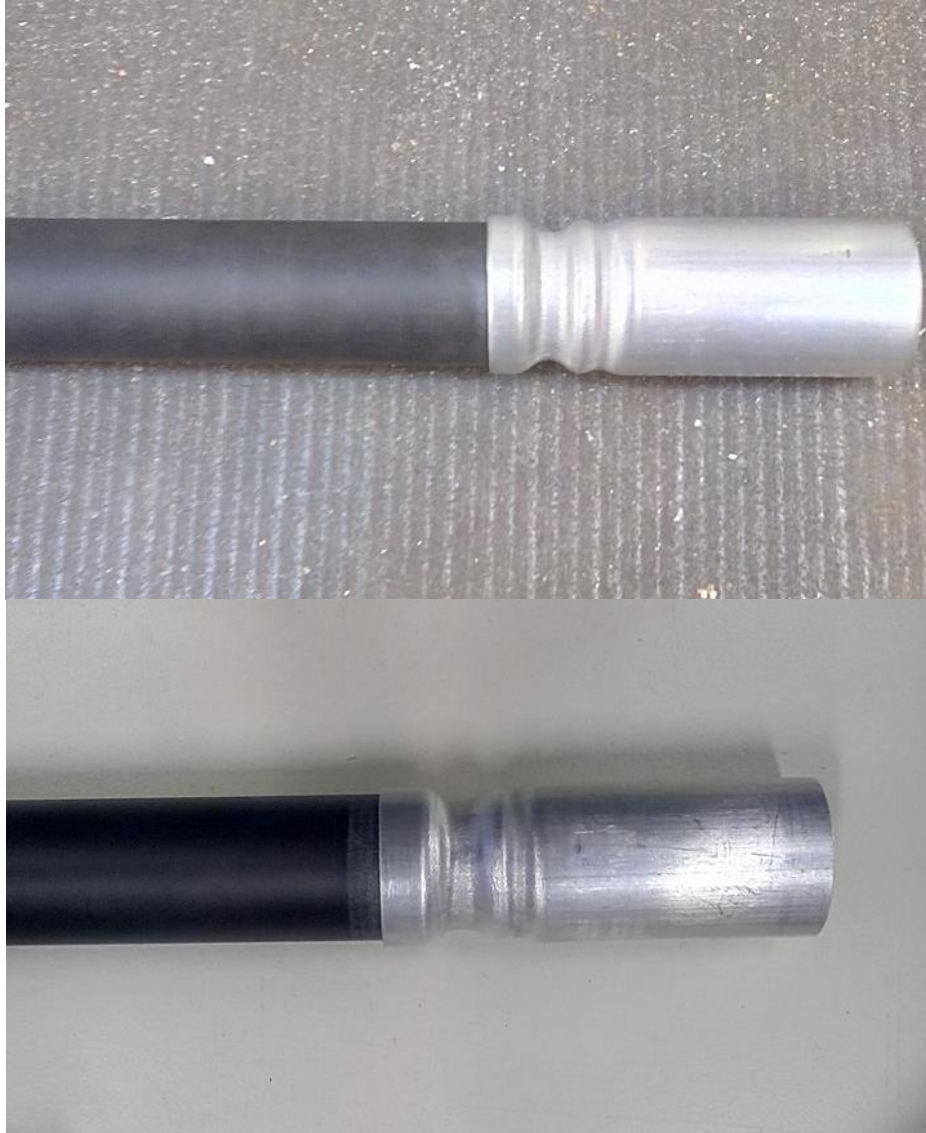


*Figure 36 - Result of the preliminary test at 14 kV (top) and 16 kV (bottom).*

From a first analysis of Figure 36 the only apparent difference is the increased contact area at the deepest groove, visible through the appearance of a flatter deformed surface. This is consistent with previous experiments involving metal to metal form-fit joining with increasing energy levels already referred in the state of the art review [25, 31, 39, 42, 43, 52].

Both joints were removed from the EMPT setup without any problems. however, after applying minimal force to the joint produced with 16 kV, the composite broke through the middle of the deepest groove (Figure 37).

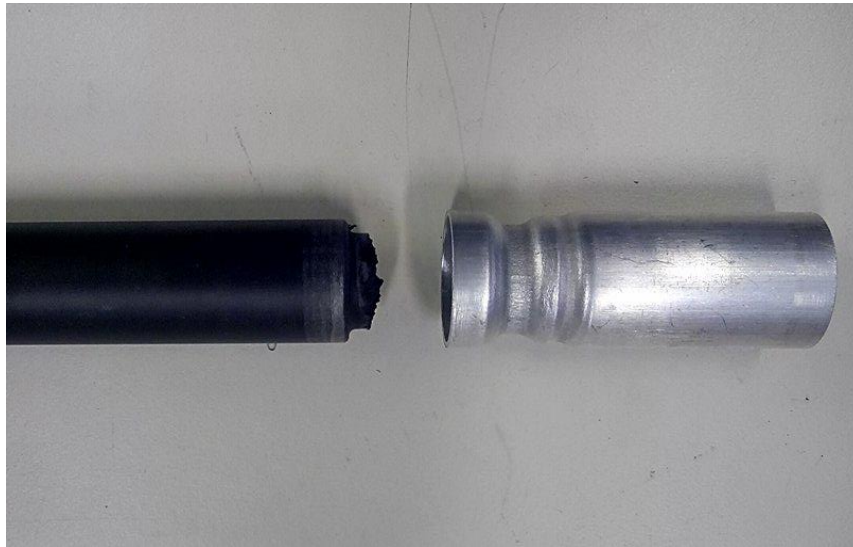


**Figure 37 - Broken joint produced at 16 kV.**

The other test specimen was cut along its revolution axis (Figure 38) in order to examine the integrity of the mandrel as well as the filling capacity of the joint produced at 14 kV. Through the analysis of Figure 39, no cracking or damage is visible. Complete filling of both grooves is achieved, the exception being the deeper groove's bottom corners (Figure 40).



**Figure 38 - Scheme for the cut of the specimens.**



**Figure 39 - Test specimen produced at 14 kV after a longitudinal cut with no visible cracks and with almost complete filling of the cavity.**



**Figure 40 - Detail of the groove region of the cut specimen.**

This preliminary test using just two specimens allowed to establish the maximum energy level to 15 KV. The other energy levels used are 12.5 KV and 14 KV. It is expected that these values will be enough to characterize the form-fit joining of metal and composite tubes, hence the design of the experiment can be laid out (Table 6). Considering the three energy levels chosen and the three joint designs proposed, a total of 9 possible combinations are manufactured and tested. In order to verify the repeatability of these tests, three samples are produced for each combination. One of them will be cut to visually analyze groove filling capabilities and damage while two others will be subjected to tensile tests.

**Table 6 - Design of experiments proposed to evaluate the EMPT form-fit joining.**

<b>Voltage</b>	<b>Design 1</b>	<b>Design 2</b>	<b>Design 3</b>
<b>Level 1 12.5 KV</b>	L1D1-1	L1D2-1	L1D3-1
	L1D1-2	L1D2-2	L1D3-2
	L1D1-3	L1D2-3	L1D3-3
<b>Level 2 14 KV</b>	L2D1-1	L2D2-1	L2D3-1
	L2D1-2	L2D2-2	L2D3-2
	L2D1-3	L2D2-3	L2D3-3
<b>Level 3 15 KV</b>	L3D1-1	L3D2-1	L3D3-1
	L3D1-2	L3D2-2	L3D3-2
	L3D1-3	L3D2-3	L3D3-3

Figure 41, Figure 42 and Figure 43 show the end result of the electromagnetic tube joining process for the three joint types proposed, with the energy level corresponding to 15 kV. They all appear to be in good condition as it is visible from the figures bellow.



*Figure 41 - Example of a form-fit joint for design 1.*



*Figure 42 - Example of a form-fit joint for design 2.*



*Figure 43 - Example of a form-fit joint for design 3.*

## 4.3 Results

### 4.3.1 Cross-Section Analysis

In this section, the analysis of the cut specimens takes place. The first specimen from each of the *energy-joint design* combinations was selected and was cut along its revolution axis. Several specimens appeared broken after the cutting process even though they all seemed to be in good conditions prior to this operation. Afterwards, taking advantage of an optical microscope, photographs were taken for analysis. Figure 44, Figure 45 and Figure 47 present the cut specimens' microscope view with a 0.5x objective.

The asymmetric tube deformation verified in several of these photographs is due to the nature of the coil used in the tests. Single turn coils (Figure 6) exhibit a gap so that the electric current can flow through it and around the workpiece. This material discontinuity implies that no magnetic fields are generated in that region and therefore there is no magnetic pressure [53].

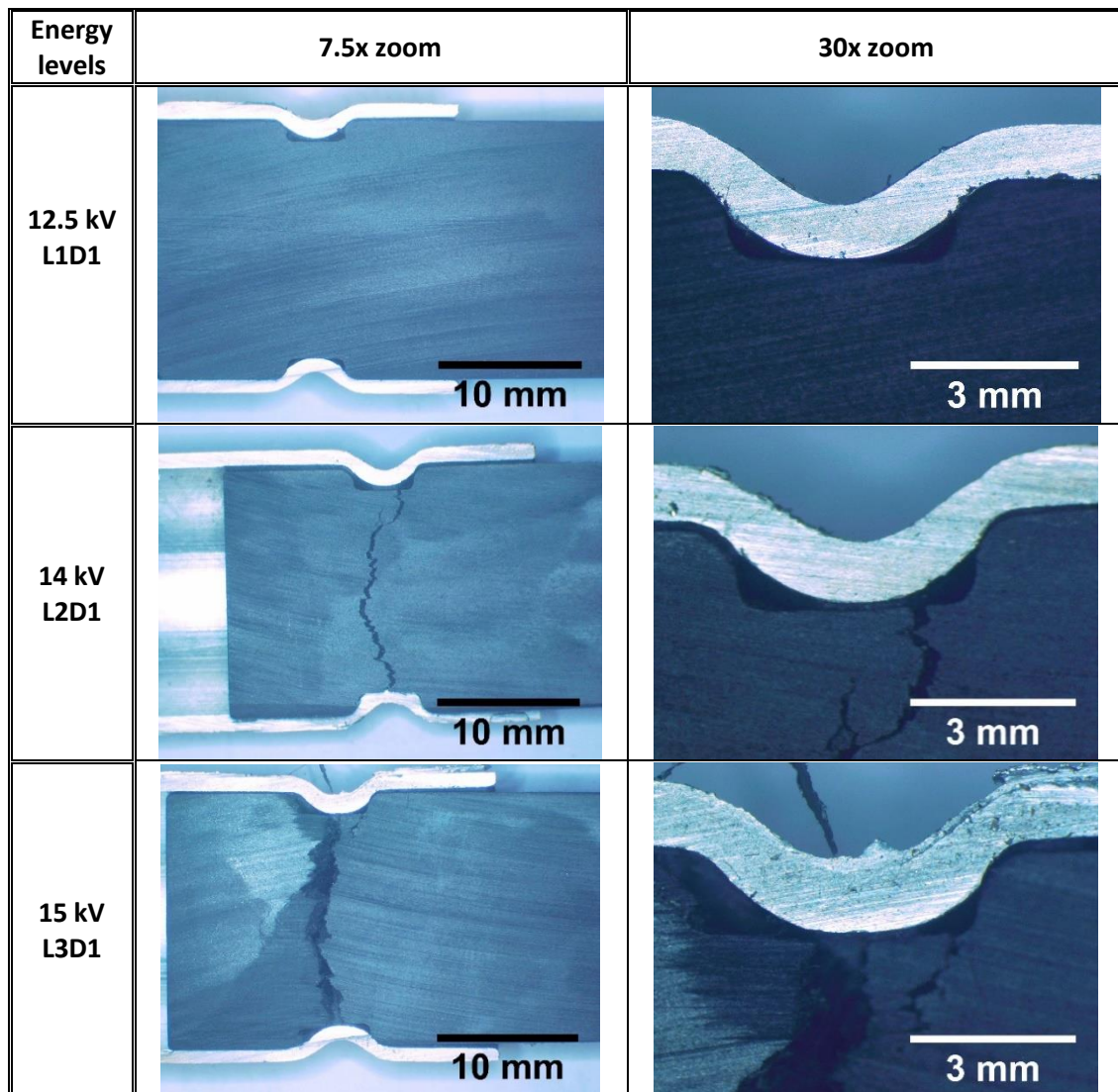
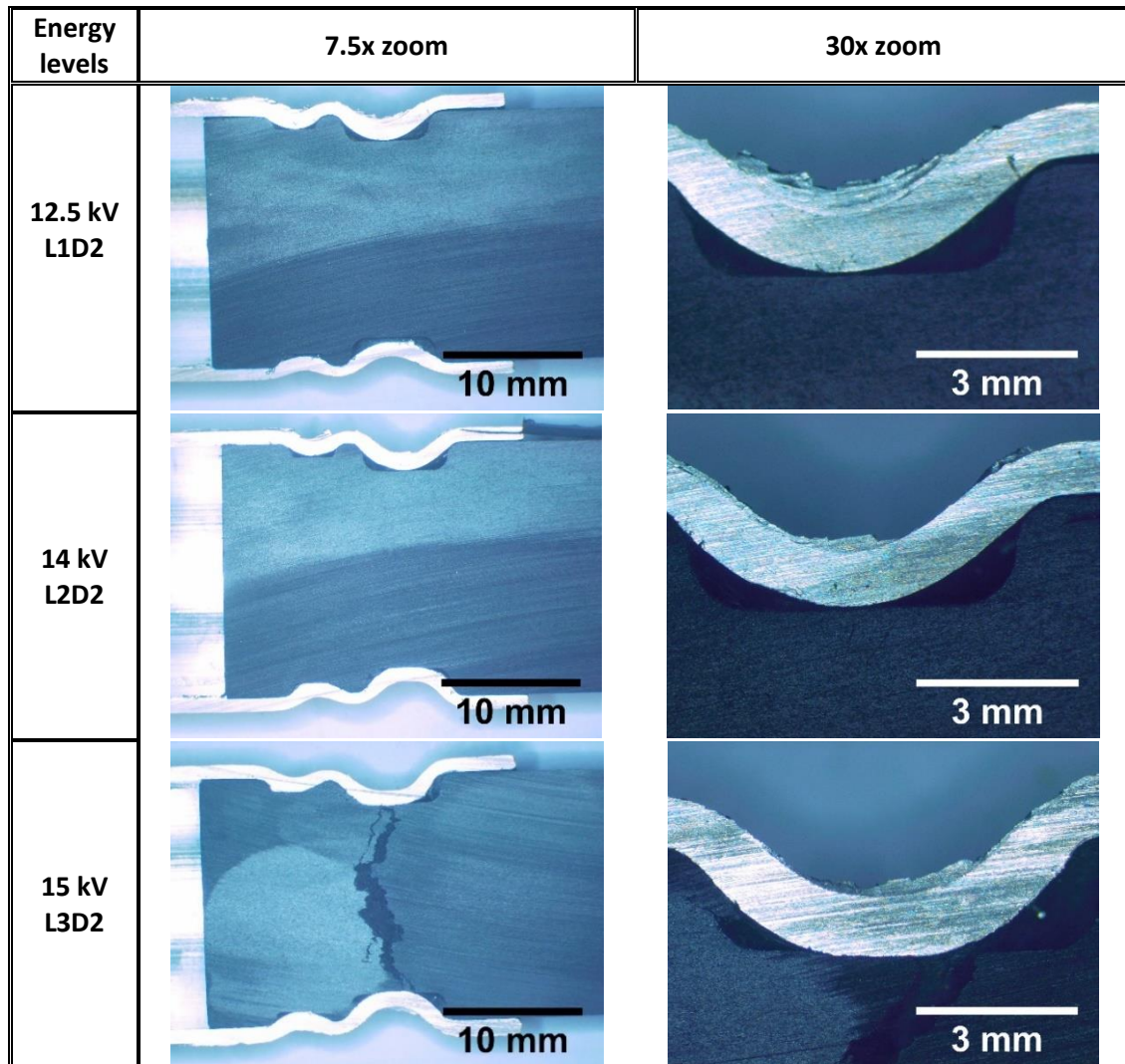


Figure 44 - Joint 1: microscope images of the groove's area with 7.5x zoom (on the left column) and detailed view of the top half-section with 30x zoom (on the right column) for the proposed energy levels.

The results for joint 1 present a single intact joint, formed with 12.5 kV. The tube does not touch the groove bottom (hence there is no complete filling) and no damage to the composite is visible. The other two specimens appear broken more or less in the middle of the groove. Similar damage is visible, although the fracture is more significant in the 15kV sample. The higher energy deformation presents damage to the groove edge radius region as well.



**Figure 45 - Joint 2: microscope images of the groove's area with 7.5x zoom (on the left column) and the detailed view of the top half section with 30x zoom, emphasizing the deeper groove (on the right column) for the proposed energy levels.**

Similarly to the analysis for joint 1, joint 2 produced with 12.5 kV is visually acceptable since neither excessive deformation in the tube nor cracking in the composite exist, although the tube barely touches the groove bottom. The specimens formed with the two other energy levels on the other hand, display different degrees of damage in the composite mandrel: the joint produced with 15 kV was fractured to the point of detachment; the one produced with 14 kV, although looking acceptable at first sight, presents composite cracking on the bump between the first and second grooves (Figure 46).

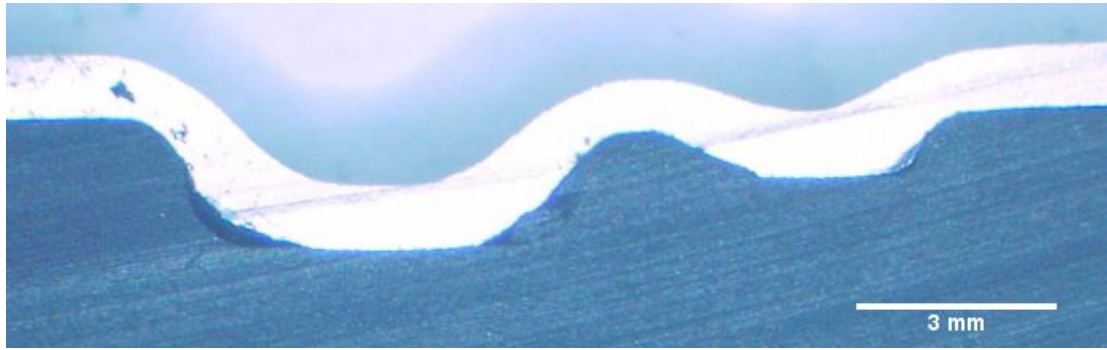


Figure 46 - Cracked region in joint L2D2.

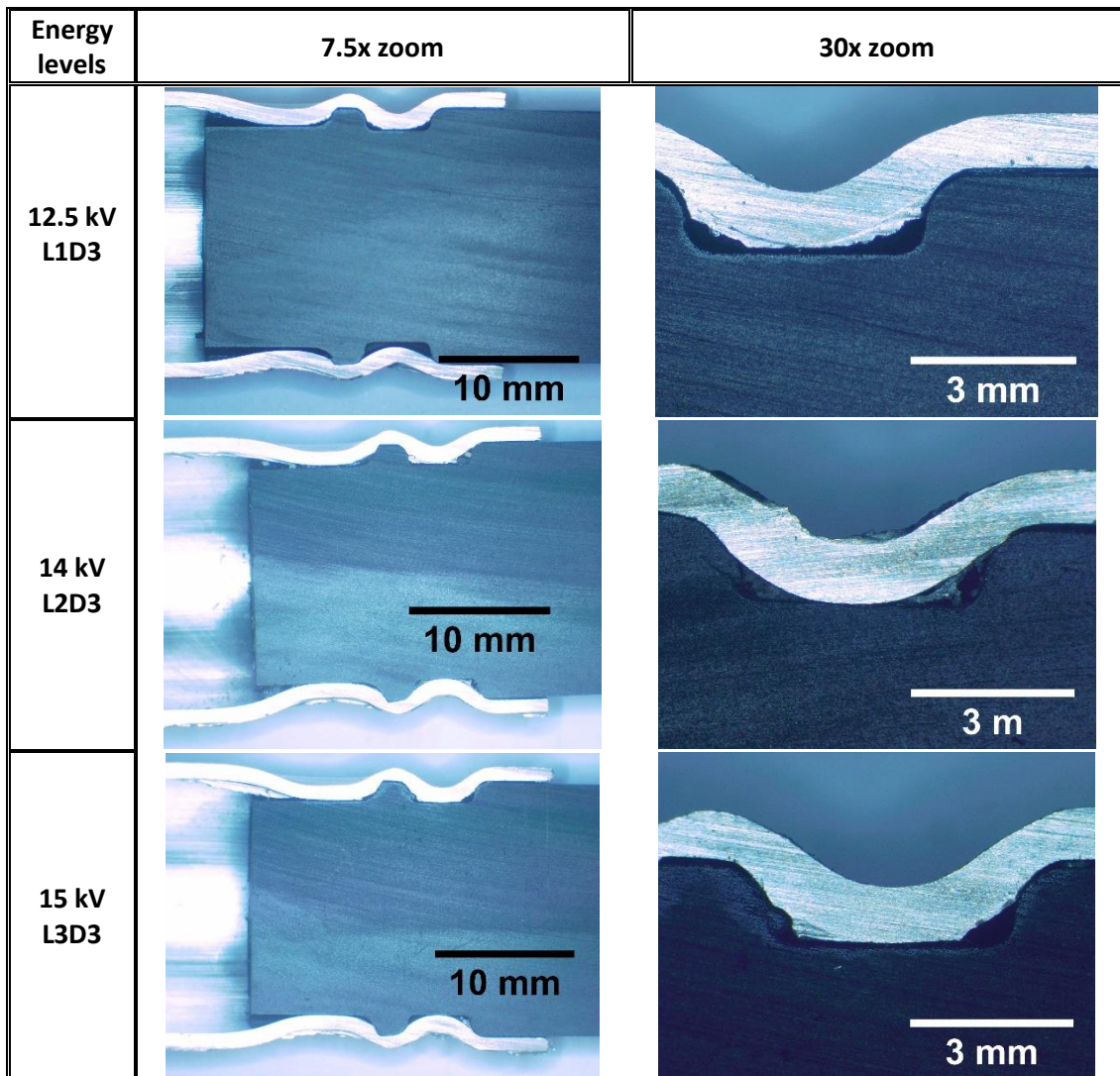
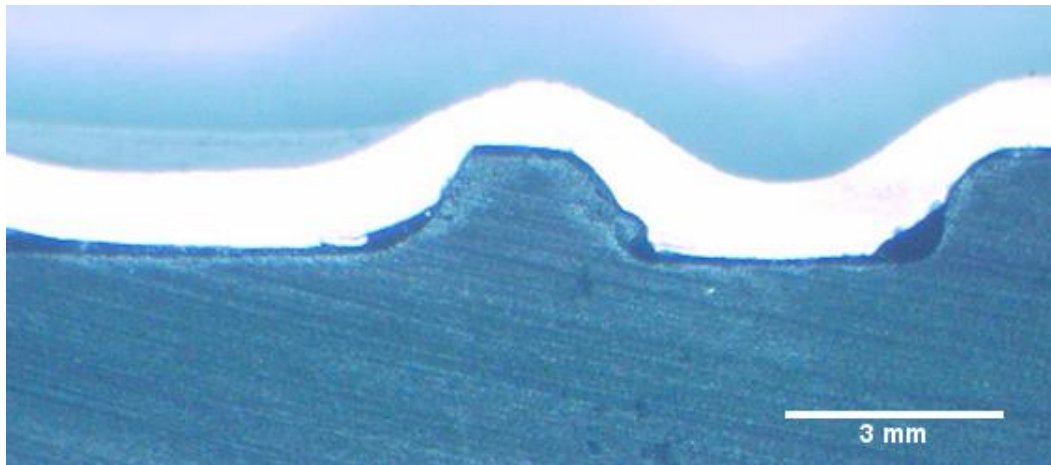


Figure 47 - Joint 3: microscope images of the groove's area with 7.5x zoom (on the left column) and the detailed view of the top half section with 30x zoom, emphasizing the deeper groove (on the right column) for the proposed energy levels.

Joint 3 was the only design that did not appear completely fractured for any energy level of forming. However, the only specimen to appear perfectly intact after cutting is the one formed with the lowest energy level (12.5 kV). The other two joints present minimal cracking in the region between the two grooves (Figure 47) which may or may not influence the tensile performance of these joints.

For this joint design, a higher degree of deformation (thinning) of the tube is visible in the region where the axial groove's edge radius is located (Figure 48). This is a zone where no concordance has been designed due to the manufacturer's demands.



*Figure 48 - Detail of the most damaged region for joint L3D3.*

#### **4.3.1.1 Discussion**

As for all mechanical tests procedures, deviations may occur in this analysis: the handling and cutting operations may have altered the joint's characteristics after the joining process. Excessive feed force or cutting speeds may have increased minor superficial cracks until they reached the other side of the specimen, for example. Some of the cut specimens also show the presence of burrs and rough edges originated from the cutting process that make them harder to analyze.

The fact that only one joint of each type was used for this evaluation does not allow to prove that all joint produced with each of the parameter combination will behave or look like the one selected for this analysis.

Considering the results obtained from this microscopic analysis, several conclusions may be taken regarding the joints' behaviour with increasing energy levels:

- Increasing damage is visible with increasing energy level for all joints that are fractured;
- Problems in the composite and not the tube;
- The lowest energy level seems to be the most adequate in this experiment if we assume one single optimal pressure for all the joint designs, as it always provides acceptable groove filling and no damage;
- Fracture always occurs in the zone where the highest impact velocity is located (deeper groove);
- Joint 3 has an evident region that could use optimization. However, it was the only one that did not appear fractured through thickness in any of the specimens;
- The fact that the three joints behave differently during forming may be due to the increased contact area originated from the double grooved features or to the increased deformation.

### 4.3.2 Tensile Tests

In order to study the feasibility of electromagnetically formed joints between metal and composite tubes, two of each of the previously produced joints were tensile tested at a rate of 2 mm/min. The ASTM A370 standard for testing of steel products [54] was adapted in order to test the tensile behaviour of the joints in question. A servohydraulic testing machine was used, equipped with hydraulic clamps able to apply 100 bar of pressure for holding the cylindrical specimens. The joint was assembled to the testing machine as presented in Figure 49: the composite bar fixed to the lower clamp with a holding pressure of 100 bar (the maximum possible) and the aluminum tube to the upper side, with a holding pressure of 70 bar. In order to hold the hollow tube without compromising its integrity, a snug-fitting metal plug is inserted on that side as proposed in the previously mentioned ASTM standard (Figure 50).

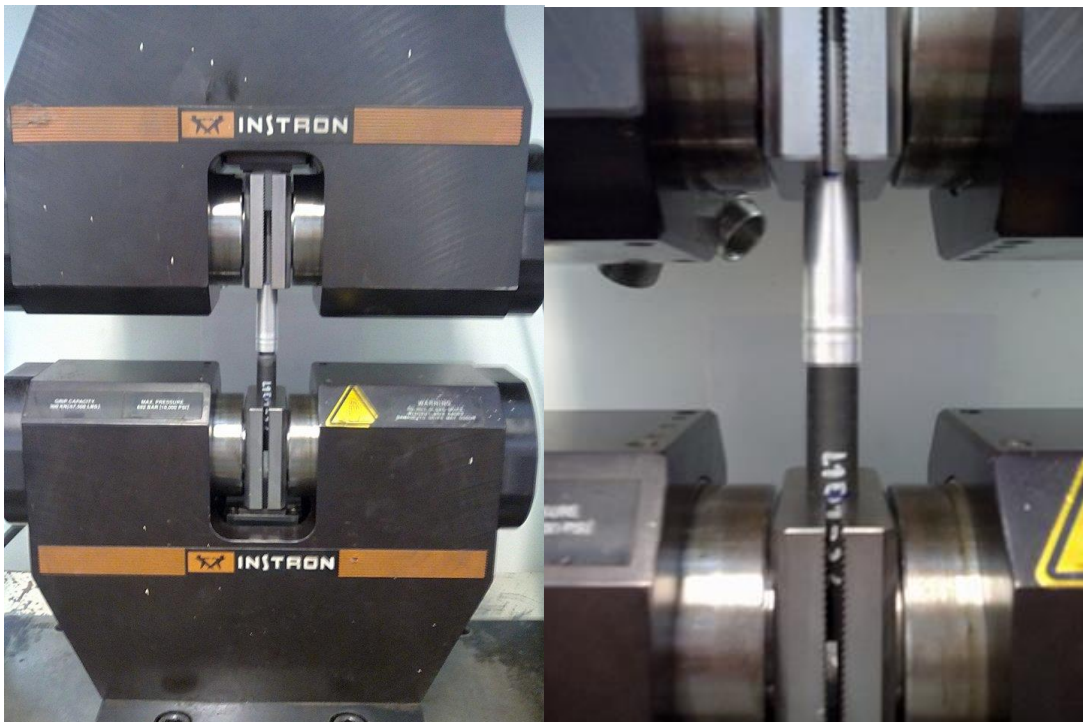


*Figure 49 - Setup of the tensile testing.*

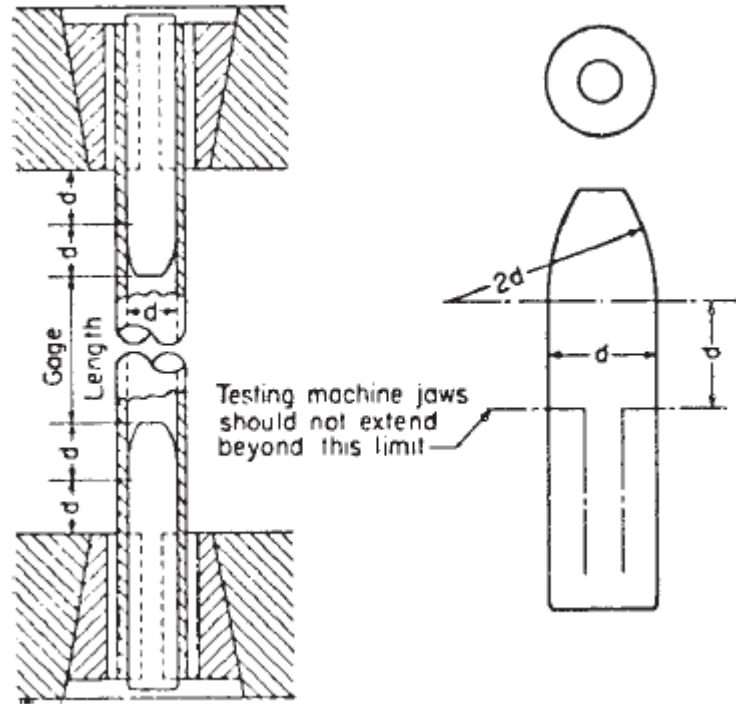


Figure 50 - Snug-fitting metal plug inserted in the tube's ending [ASTM a370] [54].

In this chapter, the results obtained from the tensile tests of the joints will be presented and discussed.

### 4.3.2.1 Joint 1

#### 4.3.2.1.1 12.5 kV

Figure 51 presents the results obtained for the two samples of Joint 1 formed with 12.5 kV in the form of a load-displacement curve.

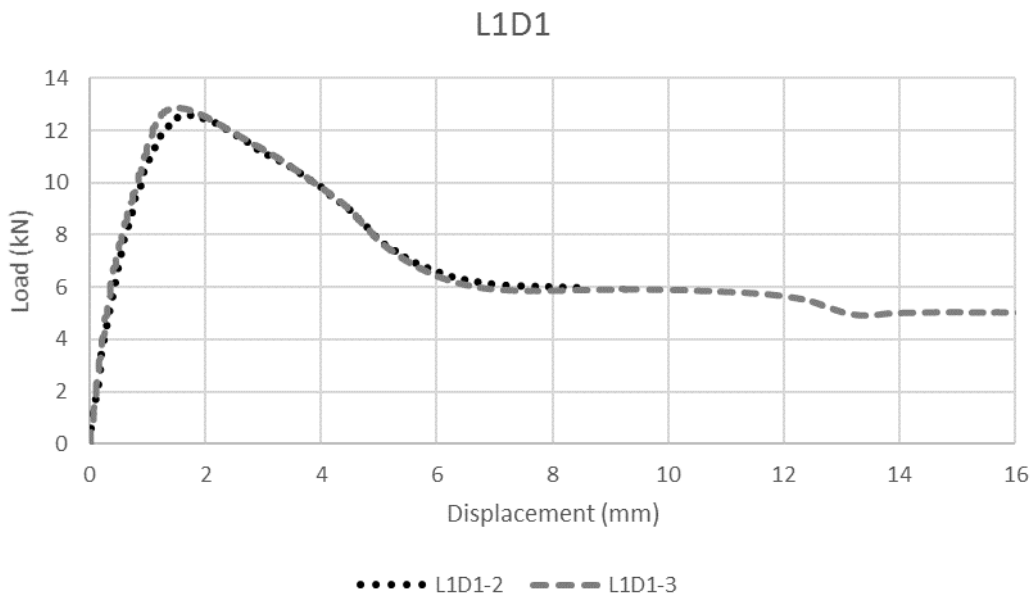


Figure 51 - Load-displacement curves for joint L1D1.

The two specimens from this combination behaved similarly, as the joint failed because of localized deformation in the aluminum where it was previously formed into the rod's groove (Figure 52). After the load peak, when the aluminum starts to yield, the two components start slipping. Residual resistance is still noticeable after a 6 mm displacement (around 6 kN) due to the force-fit mechanism.



*Figure 52 - Joints L1D1-2 (bottom) and L1D1-3 (top) after tensile testing. Notice the plastic deformation of the aluminum tube out of the groove.*

Table 7 presents the maximum loads achieved in the L1D1 joints tests and respective displacement.

*Table 7 - Maximum load and corresponding displacement for the L1D1 joints.*

Trial	Max load (kN)	Displacement at max load (mm)
L1D1-2	12.872	1.464
L1D1-3	12.608	1.664

#### 4.3.2.1.2 14 kV

Figure 53 presents the results obtained for the two samples of Joint 1 formed with 14 kV in the form of a load-displacement curve.

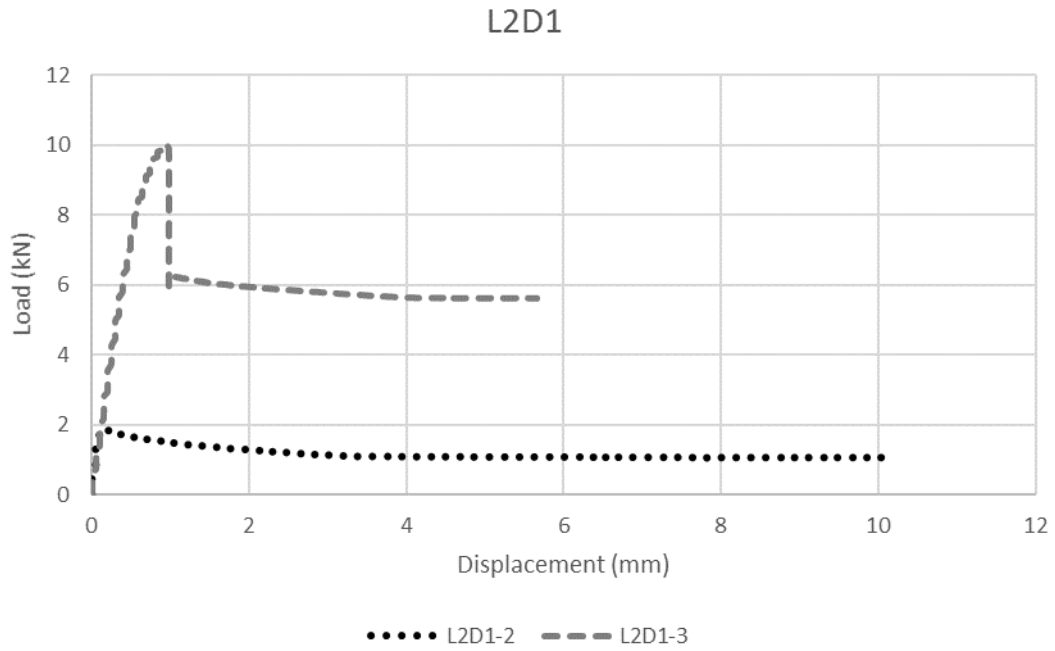


**Figure 53 - Load-displacement curves for joint L2D1.**

Unlike the first analysis, the two specimens exhibit distinct behaviors. The first specimen, L2D1-2, seems to have been already fractured before testing, reaching a maximum load of only 1.872 kN and maintaining residual resistance (again due to the force-fit mechanism's contribution). On the other hand, the specimen L2D1-3 endured the test almost until 10 kN where it violently broke, evidencing the brittle characteristics of short glass fiber filled polymers. Table 8 presents the maximum loads achieved in the L2D1 joints and their respective displacements.

**Table 8 - Maximum load and corresponding displacement for the L2D1 joints.**

Trial	Max load (kN)	Displacement at max load (mm)
L2D1-2	1.872	0.144
L2D1-3	9.992	0.928



*Figure 54 - Joints L2D1-2 (bottom) and L2D1-3 (top) after tensile testing.*

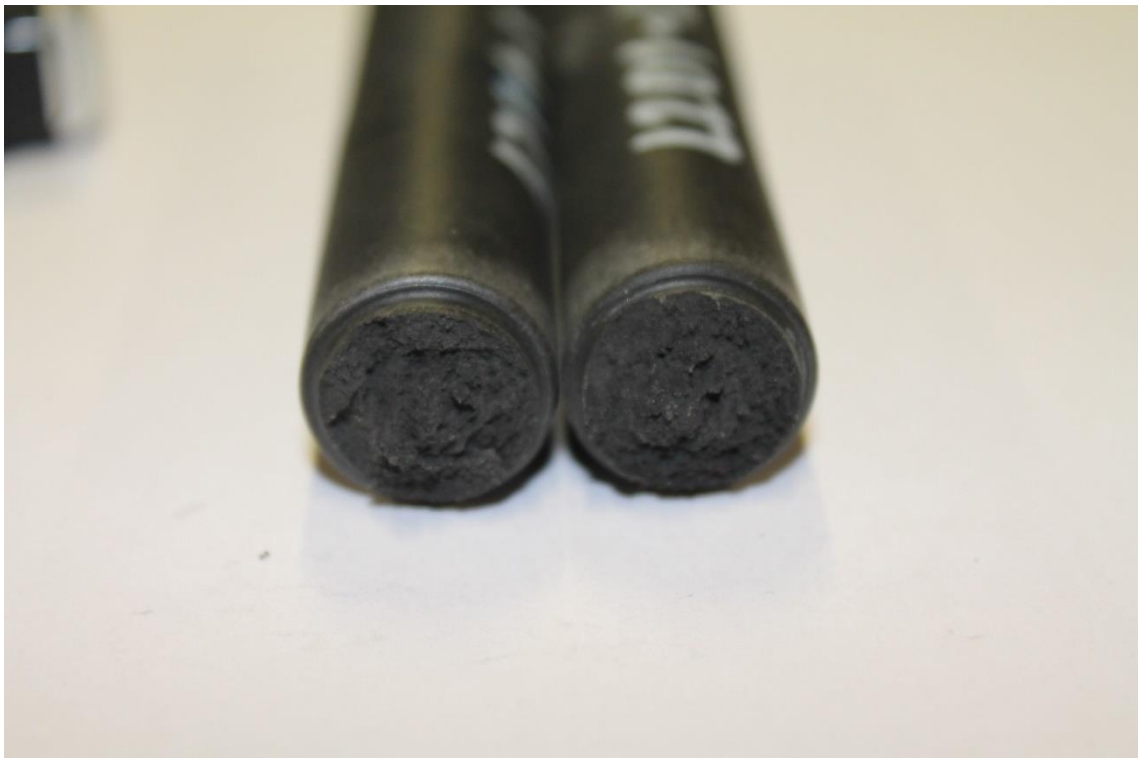


*Figure 55 - Detail of the fracture surface for joints L2D1-2 (right) and L2D1-3 (left).*

When analyzing Joint 1 manufactured with 14 kV, it is possible to conclude that the composite rod may have been already damaged since the maximum load for joints L1D1 (around 12 kN) was not reached. Less load than the necessary for mode 1 failure of the joint (deformation of the aluminum tube out of the groove) has caused composite fracture.

## 4.3.2.1.3 15 kV

Figure 56 presents the results obtained for the two samples of Joint 1 formed with 15 kV in the form of a load-displacement curve.

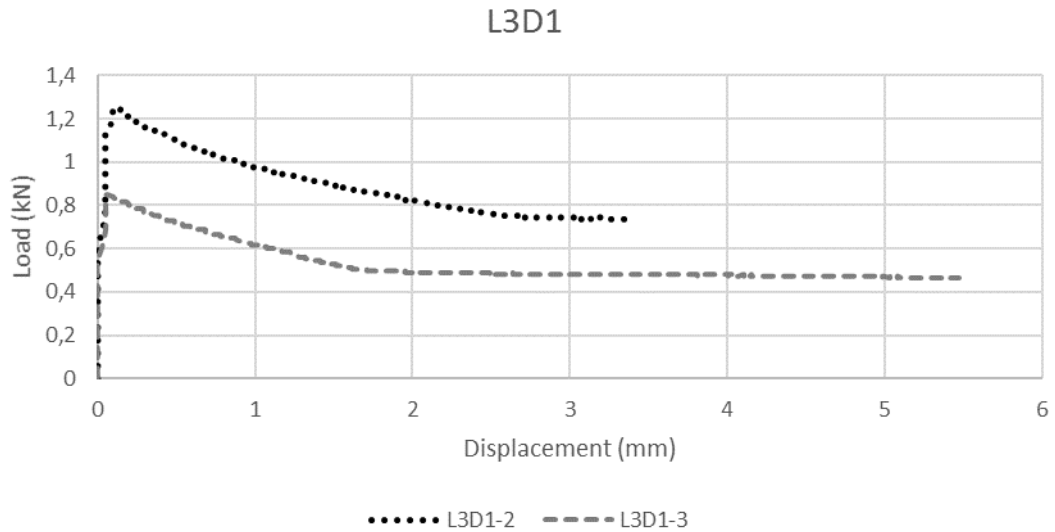


**Figure 56 - Load-displacement curves for joint L3D1.**

Both specimens were broken in the beginning of the tests, providing minimal resistance (around 1 kN), suggesting that excessive energy was used. Table 9 presents the maximum loads achieved in the L3D1 joints and their respective displacements.



**Figure 57 - Joints L3D1-2 (bottom) and L3D1-3 (top) after tensile testing.**

*Table 9 - Maximum load and corresponding displacement for the L3D1 joints.*

Trial	Max load (kN)	Displacement at max load (mm)
L3D1-2	1.248	0.096
L3D1-3	0.848	0.052

### 4.3.2.2 Joint 2

#### 4.3.2.2.1 12.5 kV

Figure 58 presents the results obtained for the two samples of Joint 2 formed with 12.5 kV in the form of a load-displacement curve.

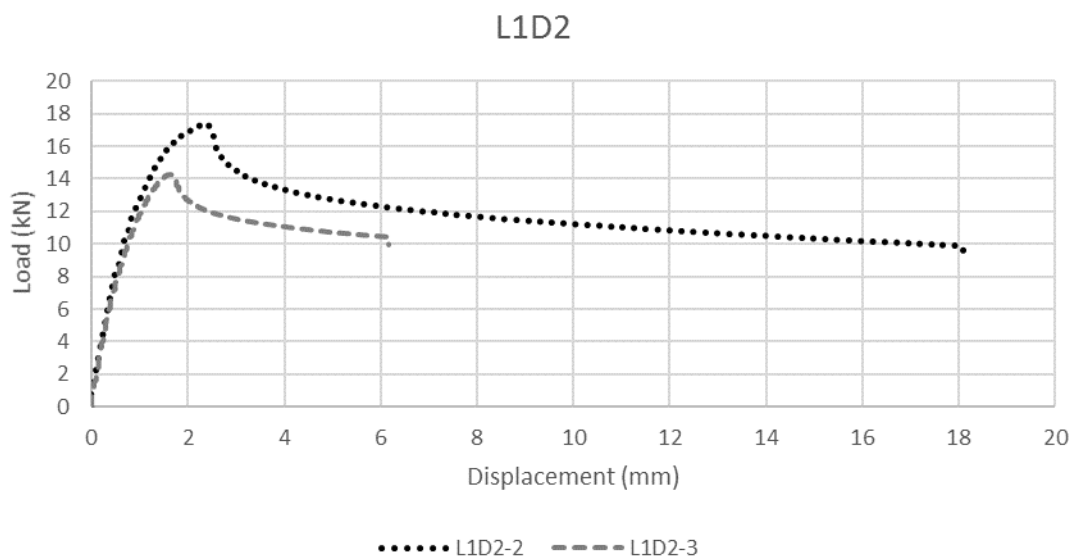


*Figure 58 - Load-displacement curves for joint L1D2.*

During the tensile testing of this joint, the apparent maximum load does not represent the actual failure of the joint: it is due to the inability of the setup to hold the composite side of the joint. Noticeable slippage started to occur when the load value started to decrease. The reason for this appears to be the lack of roughness on the composite's surface. As the maximum holding force was already being applied, the tests could not be performed until the ultimate admissible load. However, the joint is resistant to loads of at least 14 kN. Tube yield starts to occur for specimen L1D2-2 between 14 and 16 kN, visible from the transition from a linear elastic behavior to the plastic regimen (Figure 58). Figure 59 shows these joints after the tensile tests were finished, without any visible damage.



*Figure 59 - Joints L1D2-2 (bottom) and L1D2-3 (top) after tensile testing.*

Table 10 presents the maximum loads achieved in the L1D2 joints and their respective displacements.

*Table 10 - Maximum load and corresponding displacement for the L1D2 joints.*

<b>Trial</b>	<b>Max load (kN)</b>	<b>Displacement at max load (mm)</b>
<b>L1D2-2</b>	17.360	2.388
<b>L1D2-3</b>	14.280	1.612

#### 4.3.2.2.2 14 kV

Figure 60 presents the results obtained for the two samples of Joint 2 formed with 14 kV in the form of a load-displacement curve.

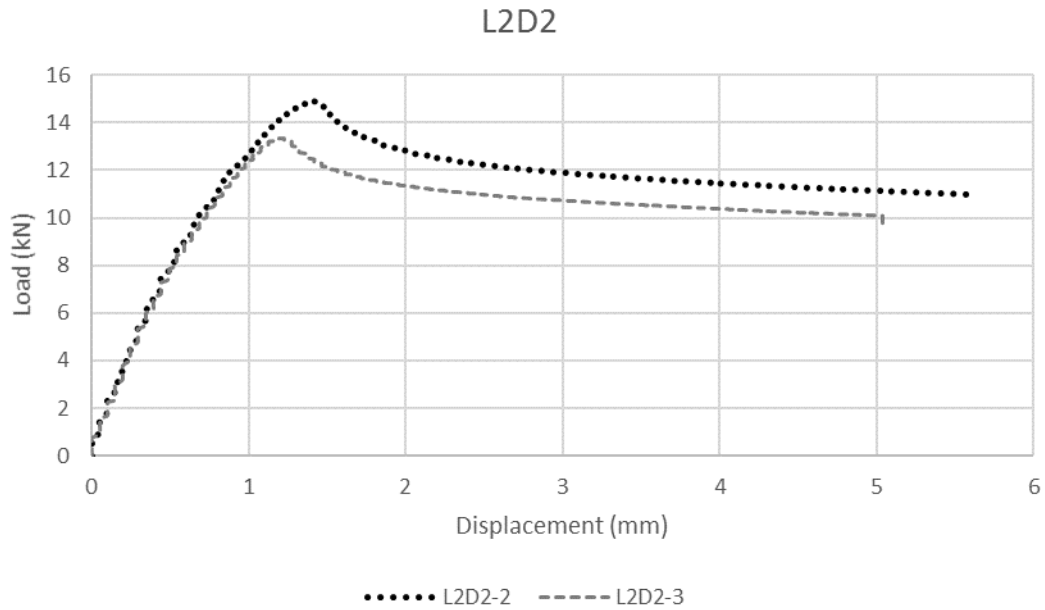


**Figure 60 - Load-displacement curves for joint L2D2.**

The same problem related to the slipping of the composite's side occurs in joint type L2D2 and therefore no failure load is possible to reach. However, force values above 13 kN are reached.

Table 11 presents the maximum loads achieved in the L2D2 joints and their respective displacements.

**Table 11 - Maximum load and corresponding displacement for the L2D2 joints.**

Trial	Max load (kN)	Displacement at max load (mm)
L2D2-2	14.920	1.416
L2D2-3	13.328	1.212

#### 4.3.2.2.3 15 kV

Figure 61 presents the results obtained for the two samples of Joint 2 formed with 15 kV in the form of a load-displacement curve.

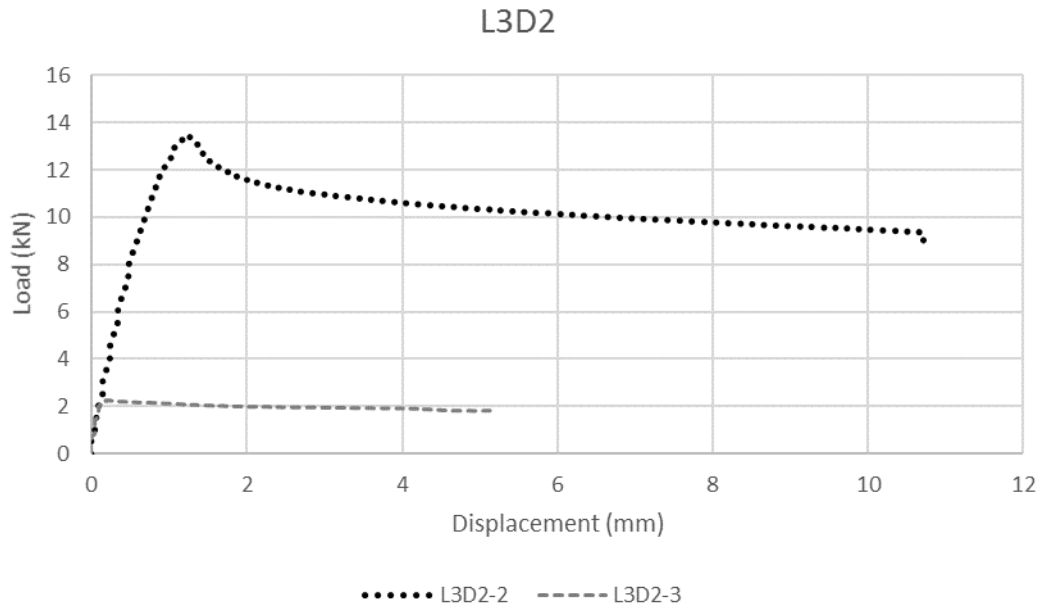


**Figure 61 - Load-displacement curves for joint L3D2.**

The first sample suffered from the same slippage problem before failure. The second one was already fractured since the assembly of the joint due to excessive magnetic pressure and did not exceed 2.248 kN after minimal displacement. For the other sample, the load reached 13.432 kN before sliding. The two specimens can be seen in Figure 62.



**Figure 62 - Joints L3D2-2 (bottom) and L3D2-3 (top) after tensile testing.**

Table 12 presents the maximum loads achieved in the L3D2 joints and their respective displacements.

*Table 12 - Maximum load and corresponding displacement for the L3D2 joints.*

Trial	Max load (kN)	Displacement at max load (mm)
L3D2-2	13.432	1.220
L3D2-3	2.248	0.196

### 4.3.2.3 Joint 3

#### 4.3.2.3.1 12.5 kV

Figure 63 presents the results obtained for the two samples of Joint 3 formed with 12.5 kV in the form of a load-displacement curve.

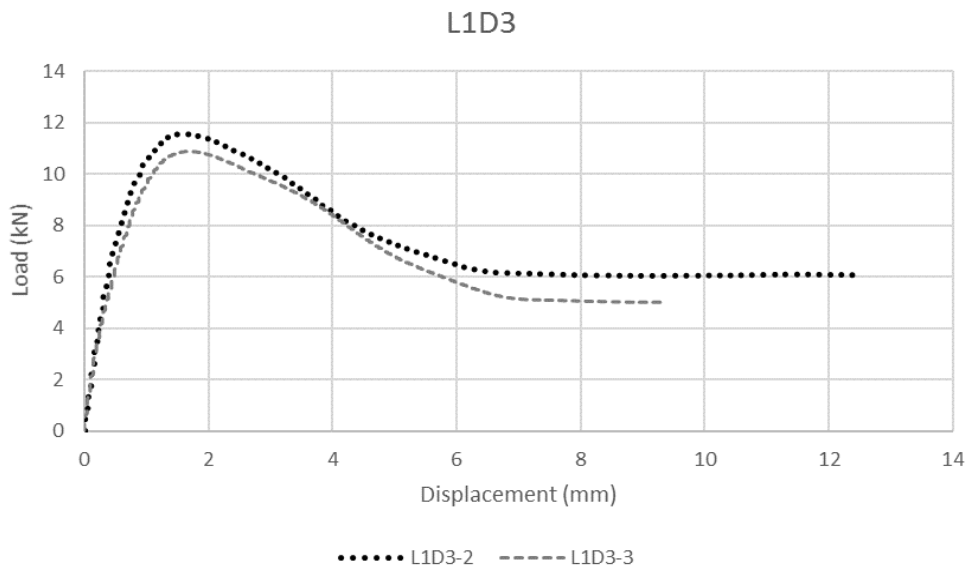


*Figure 63 - Load-displacement curves for joint L1D3.*

Joint 3 formed with the lowest discharge energy suffered from the same failure mechanism as joint 1 for the same energy level: localized tube deformation out of the tube, followed by slippage, without composite damage. This failure mechanism is evidenced in Figure 64.



*Figure 64 - Joints L1D3-2 (bottom) and L1D3-3 (top) after tensile testing.*

Table 13 presents the maximum loads achieved in the L1D3 joints and their respective displacements.

*Table 13 - Maximum load and corresponding displacement for the L1D3 joints.*

Trial	Max load (kN)	Displacement at max load (mm)
L1D3-2	11.568	1.616
L1D3-3	10.904	1.684

#### 4.3.2.3.2 14 kV

Figure 65 presents the results obtained for the two samples of Joint 3 formed with 14 kV in the form of a load-displacement curve.

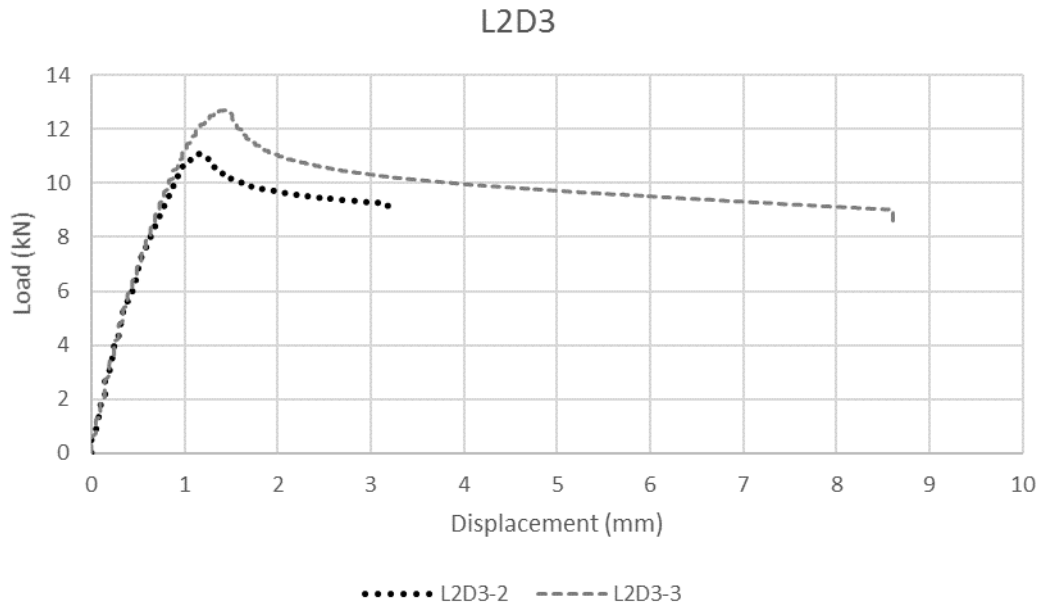


**Figure 65 - Load-displacement curves for joint L2D3.**

Again, the machine is not able to hold the composite in place when loads above 10 kN are reached. However, it is possible to say that the failure load would exceed the maximum load measured from the tests if slippage did not occur.



**Figure 66 - Joints L2D3-2 (bottom) and L2D3-3 (top) after tensile testing.**

Table 14 presents the maximum loads achieved in the L2D3 joints and their respective displacements.

*Table 14 - Maximum load and corresponding displacement for the L2D3 joints.*

Trial	Max load (kN)	Displacement at max load (mm)
L2D3-2	11.112	1.168
L2D3-3	12.712	1.416

#### 4.3.2.3.3 15 kV

Figure 67 presents the results obtained for the two samples of Joint 3 formed with 15 kV in the form of a load-displacement curve.

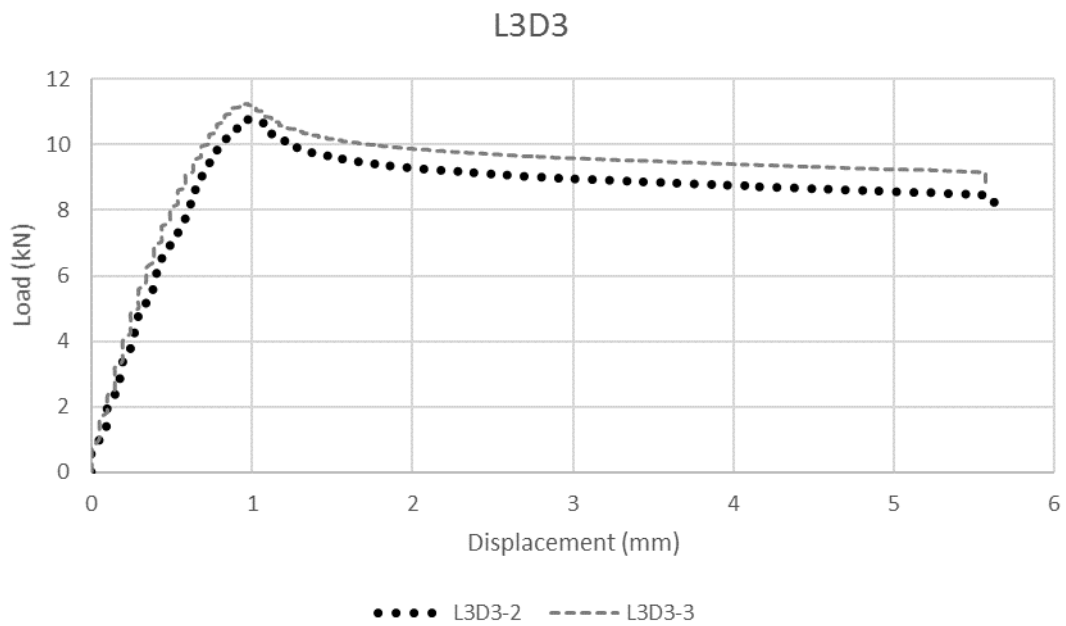


*Figure 67 - Load-displacement curve for joint L3D3.*

The peak exhibited in Figure 67 is once more due to the unwanted relative movement between workpiece and holding system and not the load responsible for the failure of the joint itself.



Figure 68 - Joints L3D3-2 (bottom) and L3D3-3 (top) after tensile testing.

Table 15 presents the maximum loads achieved in the L3D3 joints and their respective displacements.

Table 15 - Maximum load and corresponding displacement for the L3D3 joints.

Trial	Max load (kN)	Displacement at max load (mm)
L3D3-2	10.784	0.976
L3D3-3	11.256	0.972

#### 4.3.2.4 Discussion

First of all, it is important to analyse the tensile behaviour of the joints' constituents, since the connection's resistance is expected to be lower than that of the weakest component. A calculation is performed using the formula for uniaxial normal stress:

$$\text{Stress} = \frac{\text{Load}}{\text{Area}} \quad (4.1)$$

When analysing the tube, with a proof stress of 250 MPa and outer and inner radii of 10 and 9 mm respectively, this equation leads to:

$$\begin{aligned} \text{Load} &= \text{Proof Stress} \times \pi \cdot (r_o^2 - r_i^2) = \\ &= 250 \cdot e^6 \times \pi \cdot (0.01^2 - 0.009^2) = 14922 \text{ N} \cong 15 \text{ kN} \end{aligned}$$

When analysing the composite rod, with a tensile stress at break of 85 MPa and considering a minimum radius of 7.5 mm:

$$\begin{aligned} \text{Load} &= \text{Stress} \times \pi \cdot r^2 = \\ &= 85 \cdot e^6 \times \pi \cdot 0.075^2 = 15020 \text{ N} \cong 15 \text{ kN} \end{aligned}$$

These calculations allow to establish the maximum tensile load of approximately 15 kN for both the yield of the aluminum tube and the fracture of the composite rod. It is expected that this is the limit value for the admissible load before the joints' failure.

Although it was not possible to test the most resistant joints until fracture, which would enhance even further the understanding of the behaviour of metal-composite form-fit joints and would without a doubt complement this work, several conclusions can be taken for the set of experiments performed. The results for the tensile tests performed are summarized in Table 16 - Rearrangement of the tensile tests results with respective failure modes..

*Table 16 - Rearrangement of the tensile tests results with respective failure modes.*

Energy Level	Sample number	Joint 1	Joint 2	Joint 3
1 (12.5 kV)	2	Failure at 12 kN Mode 1	$\geq 17$ kN Tube yield around 15 kN	Failure at 11 kN Mode 1
	3	Failure at 12 kN Mode 1	$\geq 14$ kN	Failure at 10 kN Mode 1
2 (14 kV)	2	Broken	$\geq 14$ kN	$\geq 11$ kN
	3	Failure at 9 kN Mode 2	$\geq 13$ kN	$\geq 12$ kN
3 (15 kV)	2	Broken	$\geq 13$ kN	$\geq 10$ kN
	3	Broken	Broken	$\geq 11$ kN

For joint 1 formed with the two highest energy levels (14 and 15 kV), the joint appeared broken in the microscopical analysis, while the 12.5 kV joint did not appear completely filled. When comparing this data with the tensile tests performed in the joint 1 specimens, the same behaviour (fracture before the tensile test) occurs for the 14 and 15 kV, with the exception of one of the specimens formed with 14 kV that was able to endure almost 10 kN before breaking. For the lowest energy level, good correlation is found: in the tensile test, both samples failed at 12 kN, with a failure mode consistent with incomplete groove filling. It is thought that the optimal energy level to enhance this joint's performance is located between 12.5 and 14 kV.

For joint 2, the results obtained from the two tests match well as in the first case: the microscopic analysis indicates that no fracture occurs until the last energy level (15 kV). The tensile tests' results follow that same trend, as only one of the specimens for the highest energy level was fractured right after the joining operation. The remaining samples were

able to withstand significant impact. This may be due to a higher amount of energy (in the form of the magnetic pressure) being dissipated in the form of plastic deformation, leaving a lesser portion for the impact.

For joint 3, none of the tested joints (either through visual examination and tensile testing) fails in the composite mandrel. For the lowest energy level, both specimens used in the tensile tests failed through mode 1 (yield in the aluminum tube). The joints formed with the other two energy levels (14 and 15 kV) show no evident damage that would affect the joints tensile resistance. The tensile tests performed prove exactly that, as none of them fails before withstanding significant load.

An increase in joint strength is visible when comparing joints 1 and 2 (the exclusively axial joints). When formed with 12.5 kV, the distribution of stresses mentioned in the state of the art chapter delays the mode 1 failure present in Joint 1, allowing it to resist at least a couple more kN (maybe more). It also provides increased resistance in terms of the joint formation, allowing for the use of the 14 kV pulse.

When comparing the two single grooved joints, Joints 1 and 3, the first major difference is that none of the specimens from Joint 3 broke during the joint formation and they were all able to withstand at least 10 kN, while the specimens formed with 14 and 15 kV for joint 1 were either completely fractured or at least damaged. However, the joints formed with 12.5 kV show significant resemblance, failing through the same failure mode at identical loads.

Variations in the results for the same joint types can also be explained through several factors which may be due to the tensile test itself as well as with the joint creation process or the machining steps that took place prior to the assembly. Said factors can be summarized as:

- Residual/concentrated stresses or damage originating from the machining processes that the composite rod endured;
- Residual stresses or cracking originating from the EMPT joining processes;
- Errors in the tensile testing procedure/equipment: uncalibrated machines, incorrect specimen placement, workpiece misalignments, or differences between samples (surface roughness, for example) may potentialize the existence of pre-loads, turning an uni-axial tensile test into a different kind of sollicitation, which may lead to a loss in material behaviour repeatability.

The cutting process can also influence the joints characteristics, as minimal surface cracking may have expanded due to the process parameters (cutting speed and feed force).

#### **4.4 Summary and Outlook**

This chapter is focused on the experimental component of this dissertation. After the joint design process, a review on the materials being used in the experiments as well as on the EMPT machine's properties is performed. Preliminary tests executed allowed to estimate a critical forming energy for the composite rod's fracture. The experimental work consists on the manufacture of form-fit connections using three joint designs and three forming

energies. A total of twenty-seven specimens were produced (three samples of each *joint type – energy level* combination) in order to prove repeatability of the process. The manufactured joints are then evaluated through tensile tests and the analysis of micro-cuts. The results are presented in this chapter along with the main conclusions, which can be summarized as:

- Although the tests could not be performed until the rupture of the joint, the achieved forces are in the order of 10 to 20 kN;
- Joints 2 and 3 are able to resist to higher energy levels than joint 1. This is probably due to the increased tube deformation or contact area compared to joint 1;
- Experiments prove the increased load resisting ability of the double grooved design, when compared to the single grooved design. When formed with 12.5 kV, the distribution of stresses mentioned in the state of the art chapter delays the mode 1 failure present in Joint 1, allowing it to resist at least a couple more kN;
- Single grooved joints manufactured with low forming energies tend not to be properly filled and to fail by plastic deformation on the aluminum tube;
- When comparing the results from the tensile tests with the pictures obtained using the microscope, a good correlation can be found for all the *joint type – energy level* combinations.

All the results presented in this chapter have proven the viability of the EMPT in the joining process of metal and composite tubes. Although the resisting joints could not be tested until failure, the achieved forces are in the order of 10 to 20 kN.

# 5 NUMERICAL MODELLING OF EMPT JOINING

Numerical simulations provide a unique way of understanding the physics involved in most forming processes. They allow to predict necessary parameters for the process as well as to optimize them. The numerical modelling of the EMPT is extremely difficult due to the interaction of electromagnetic, thermal and mechanical effects [52], as represented in Figure 69 - Interactions between the electromagnetic, mechanical and thermal problems [55]. A common simplification is the omission of thermal phenomena, which is known as the least influencing between the three.

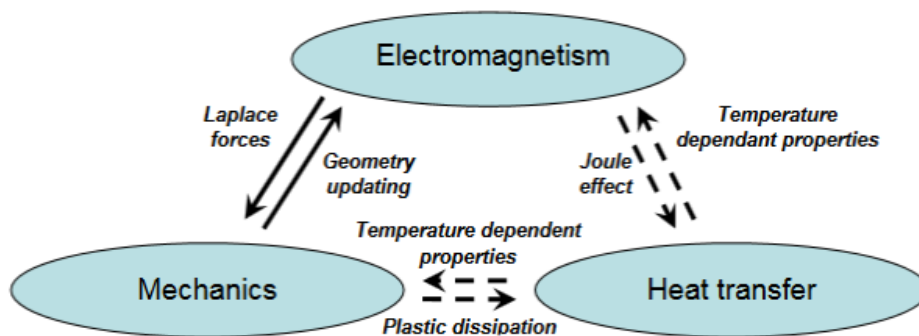


Figure 69 - Interactions between the electromagnetic, mechanical and thermal problems [55].

There are three approaches when simulating the EMPT:

- Non-coupled approach: this is the simplest approach, as it solves the electromagnetic and mechanical problems independently, incorrectly describing the problem. Maxwell's equations for the electromagnetic field are solved without taking the workpiece velocity and deformation into account. The acting pressure is then estimated and used in order to solve the mechanical problem. Although it is not the most accurate approach, it provides satisfying results with the best computational times [52];
- Loosely-coupled approach: in each step of the simulation, the electromagnetic pressure is calculated and fed as input into the mechanical problem. As that step's deformation is calculated and the workpiece is updated, it is sent back to the electromagnetic model to calculate the pressure distribution in the next step. This process is repeated iteratively until the end of the process time has been reached.

It provides accurate results with weak computational times as at each step, the forces are calculated based on the previous step's workpiece geometry [52]. As the electromagnetic part of the system is influenced by the spatio-temporal evolution of the deformation of the workpiece, recent efforts have been done to simulate these complex coupled methods [56];

- Fully-coupled approach: in each step of the simulation, the effects of electromagnetic, mechanical, and thermal fields are calculated through a complex set of electromagnetic-mechanical equations. It is without a doubt the most complex approach and the one that requires the highest computation times, being similar to the loosely-coupled approach [52].

## 5.1 Review on EMPT Modelling and Simulations

In [57], ABAQUS is used to simulate the electromagnetic joining of aluminum tubes. In this simulation, the dependency between workpiece geometry and the solution of the electromagnetic problem at each time step was implemented (loosely-coupled algorithm) without, however, taking thermal effects into consideration. The finite element model is axisymmetric and composed by the die (assumed rigid) and the tube (with wire elements) and the pressure application is performed through a subroutine written in FORTRAN. The Johnson-Cook material model is used for the AL110-H12 aluminum tube due to the high strain rate and a Coulomb friction coefficient of 0.15 was implemented [57].

In [58] a simulation of an uncoupled electromagnetic tube expansion against a mold was performed using ABAQUS and compared to experimental tests. The mold is considered rigid and the tube is modelled as a shell due to a diameter to thickness ratio of 47. The material properties used refer to Al 7075. For the simulation of contact, the penalty method is used with a coefficient of friction of 0.15. The pressure applied in the inner walls of the tube is obtained through external calculations and then used as input in the ABAQUS deformation analysis. A good agreement is found between experimental tests and the finite element results [58].

Nassiri et al. [59] also take advantage of ABAQUS to numerically simulate the electromagnetic tube forming process. Their 2D axisymmetric model (Figure 70) followed the analytical model previously executed in [53] and its boundary conditions were consistent with the experimental tests performed. However, thermal effects were not taken into account. They find a good agreement when comparing the analytical and FE simulation pressure distributions, workpiece radial deformation and velocity.

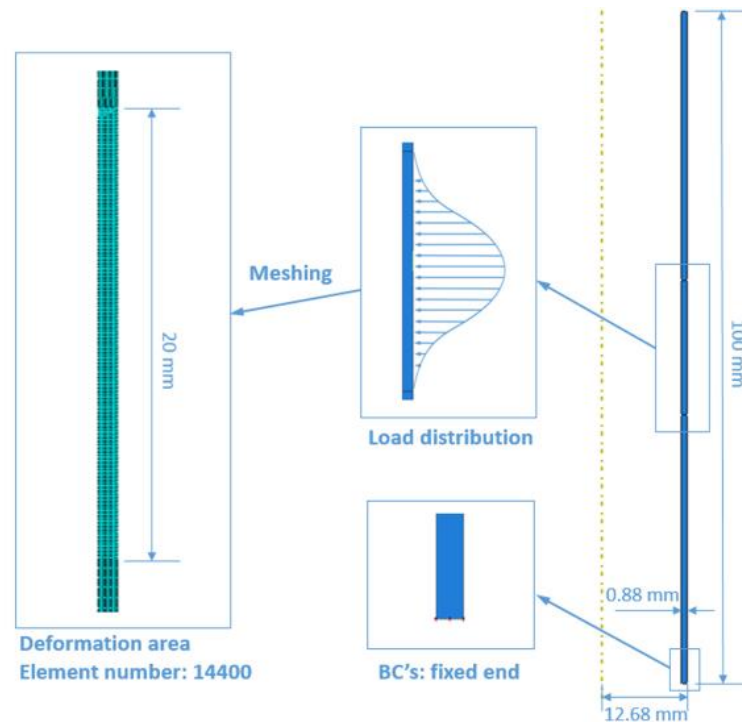


**Figure 70 - Scheme of the FEA model performed by Nassiri et al. [59].**

In [52], the three main EMPT operations are simulated: metal sheet bulging, tube expansion and compression. Each model is compared to experimental data for validation. Extensive analysis is then performed regarding the influence of process parameters. The springback mechanism is also focus of examination, comparing the EMPT with the deep-drawing process, evidencing the reduced plastic restoration in high speed deformation processes.

Karch and Roll [60] take advantage of ANSYS to model the electromagnetic tube forming with a fully coupled approach, including thermal effects due to Joule heating in the workpiece. The Johnson-Cook material model is once more used for the aluminum tube. The electromagnetic field, temperature, stress and deformation are calculated using this model and acceptable results are obtained when compared to experimental data obtained from the University of Dortmund [60].

In [55], a fully coupled 3D numerical model for the electromagnetic forming process is developed, ignoring thermal effects. A combination of two softwares is used, SYSMAGNA (useful for solving the electromagnetic part of the problem) and PAMSTAMP (dedicated to stamping process simulations). The Johnson-Cook law is used to govern the plastic behaviour of aluminum tubes and metal plates due to the need to include high strain rate effects. A good correlation is verified when comparing simulation results with experimental tests. Figure 71 provides data regarding tube diameter reduction in EMPT tube compression from the work developed by Conraux et al. [55].

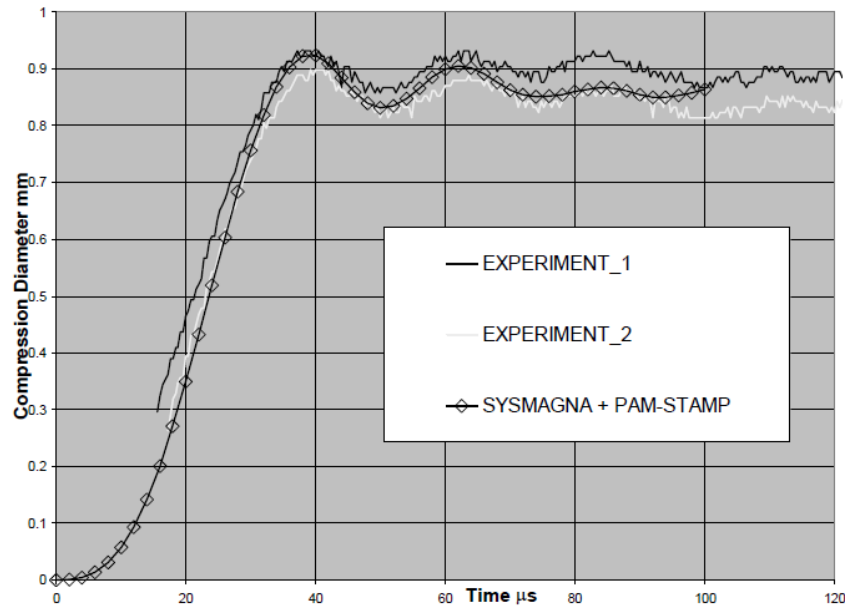


Figure 71 - Comparison between simulation and experimental data developed by Conraux et al. regarding EMPT tube compression [55].

## 5.2 Creation of the Form-Fit Joining Model

In this sub-chapter, the process for the development of the FE model for the EMPT joining of metal-composite tubes is presented. Thermal effects are not considered and a non-coupled approach is used, dividing the process into two distinct problems: the electromagnetic and the mechanical problems. As explained before, the non-coupled approach ignores the relation between pressure evolution and the shape of the workpiece and solves the mechanical problem in a single step, using data from the solution of the electromagnetic model as input. It is intended that this model provides a suitable methodology for the optimization of the form-fit joining process by EMPT.

### 5.2.1 Assumptions

In order to simplify the complex EMPT process, several assumptions are made:

- Considering the axisymmetric of the aluminum tube and the fact that the coil can be modelled by a coaxial single turn loop, an axisymmetric configuration for the numerical solution to the electromagnetic problem has been used for both workpiece and coil. Assuming this boundary condition, the magnetic field and the corresponding magnetic pressure that acts on the tube, does not vary in the circumferential direction. This assumption implies the use of a cylindrical coordinate system for the problem and, so, the computed magnetic field, Lorentz force and Eddy current have only radial and axial components [52, 61];
- The workpiece's permeability, that accounts for the ease in the induction of a magnetic field  $\mathbf{B}$  due to the presence of an external electrical field  $\mathbf{H}$ , is assumed to be very close to the vacuum permeability,  $\mu_0$  ( $\mu \approx \mu_0 = 4\pi \cdot 10^{-7} \text{ H/m}$ );
- Temperature is assumed constant and thermal effects are neglected. No significant changes in the electrical properties of the material due to temperature rise are

considered because of the short time for the heat transfer to occur. In practical situations and considering repeated shots, temperature rise may be significant and may influence process repeatability;

- The mutual inductance between coil and tube is considered constant during the entire process in account of the process' speed;
- As the process occurs in an extremely short time period, it is considered that the workpiece's velocity has no influence on the magnetic field. Therefore, the electromagnetic model can be described using the quasi-static Maxwell's equations [62].

### 5.2.2 The Electromagnetic Model

Numerical simulations were performed using the FEMM [63] software in order to obtain the solution for the electromagnetic problem. The simulation describes the electromagnetic tube compression process. The simplification related to the axisymmetric property of the workpiece allows the reduction of computational time and renders the geometrical parameters as Figure 72 presents.

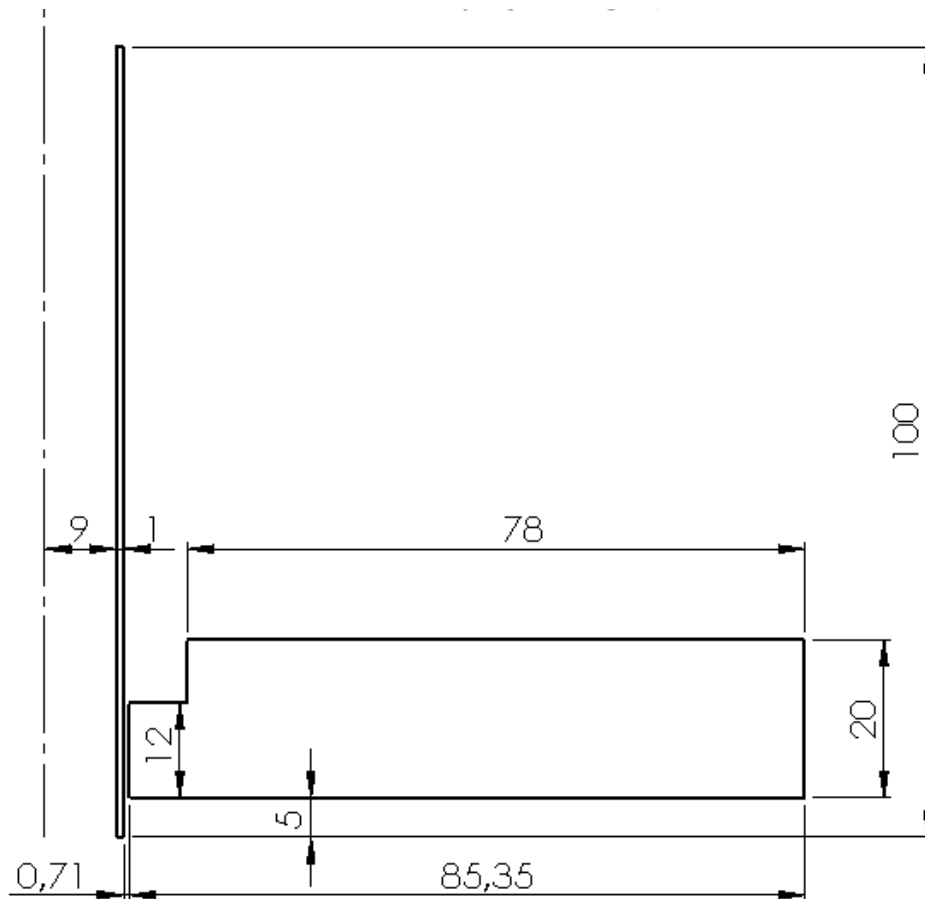


**Figure 72 - Geometry input for the electromagnetic simulation in FEMM.**

The simulations performed try to replicate the experimental procedure presented in the previous chapter. However, in order to consider the model as axisymmetric, the region of the coil where the gap is located in neither represented nor considered for the calculations.

Only doing so allows for the axisymmetric definition of the problem. The material and geometric properties used in the simulation are presented in Table 17.

*Table 17 - Material, machine and geometric properties used in the FEMM simulation.*

<b>Workpiece</b>	<b>Material</b>	Aluminum	AW 6082
	<b>Electrical conductivity</b>	$\sigma_w$	36 MS/m
	<b>Thickness</b>	t	1 mm
	<b>Outer diameter</b>	d	20 mm
<b>Coil</b>	<b>Material</b>	Steel	40 CrMnNiMo 7
	<b>Electrical conductivity</b>	$\sigma_c$	2 MS/m
	<b>Gap</b>	g	0.71 mm
<b>Air</b>	<b>Electrical conductivity</b>	$\sigma_{air}$	0 MS/m
	<b>Magnetic permeability</b>	$\mu_0$	$4\pi \cdot 10^{-7}$ H/m
<b>EMPT Machine</b>	<b>Capacitance</b>	C	40 $\mu$ F
	<b>Total inductance</b>	$L_t$	2.86 $\mu$ H
	<b>Total resistance</b>	$R_t$	28.5 m $\Omega$
	<b>Charging voltage</b>	$V_0$	2 kV

Solving the electromagnetic problem also requires the definition of the machine's discharge curve,  $I(t)$ , specifically the values for the maximum current and its frequency. These parameters can be analytically calculated using the equations below:

$$I(t) = I_0 \cdot e^{-\frac{t}{\tau}} \cdot \sin(\omega t) \quad (5.1)$$

$$I_0 = V_0 \sqrt{\frac{C}{L_t}} \quad (5.2)$$

$$\tau = \frac{2 \cdot L_t}{R_t} \quad (5.3)$$

$$\omega_0 = \frac{1}{\sqrt{L_t \cdot C}} \quad (5.4)$$

Where  $I_0$  is the maximum current,  $\omega$  is the current frequency,  $\tau$  is the wave damping factor and  $V_0$ ,  $C$  and  $L_t$  are, respectively, the circuit's charging voltage, capacitance, and total

inductance. The skin depth, representing the penetration of the “eddy current” into the workpiece can also be defined:

$$\delta = \sqrt{\frac{2\rho}{\mu_0 \omega}} \quad (5.5)$$

Where  $\rho$  is the workpiece’s electrical resistivity [52]. The discharge current’s curve is presented in Figure 73.

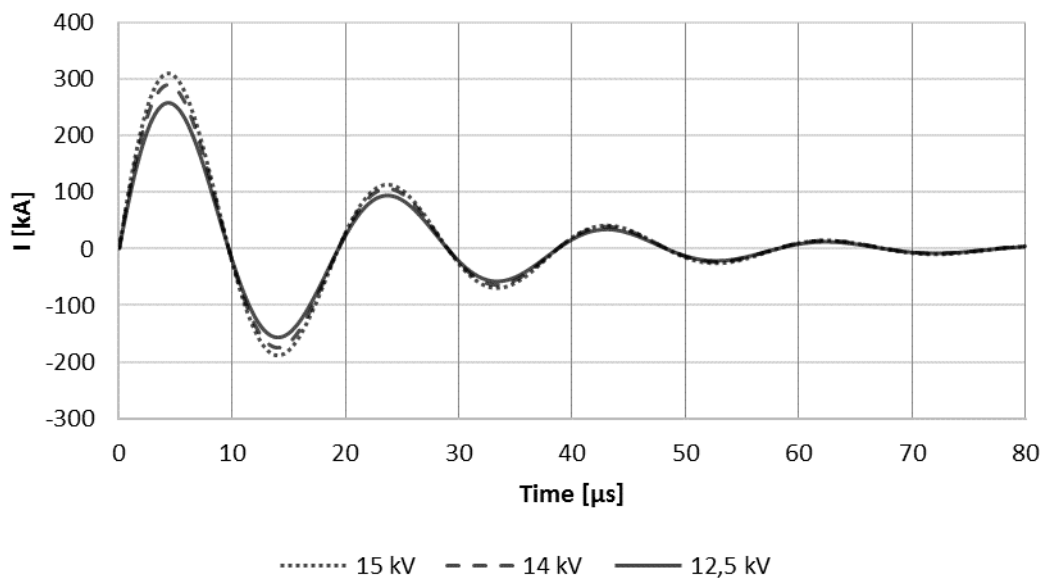


**Figure 73 - Current curves calculated using the machine parameters referred above.**

Through the analysis of Figure 73, the maximum values for the current for each of the energy levels as well its frequency can be obtained for further calculations.

For the numerical simulation of the electromagnetic problem through the FEMM software, several steps have been performed in order to describe and optimize the problem (Figure 74).

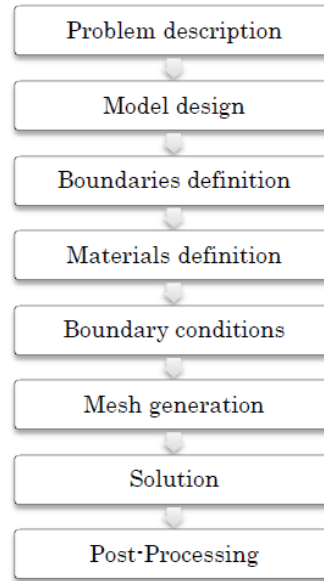


**Figure 74 - Flowchart of the modelling steps in FEMM [51].**

Using the geometrical parameters and process conditions, the model was implemented in the FEMM software [63]. A view of the electromagnetic model is shown in Figure 75.

An axisymmetric boundary condition is imposed. The outer cylindrical boundary is defined far away from the assembly in order to assure that the magnitude of the magnetic vector potential can be considered near zero in the boundary line. The properties of this region are the same as vacuum.

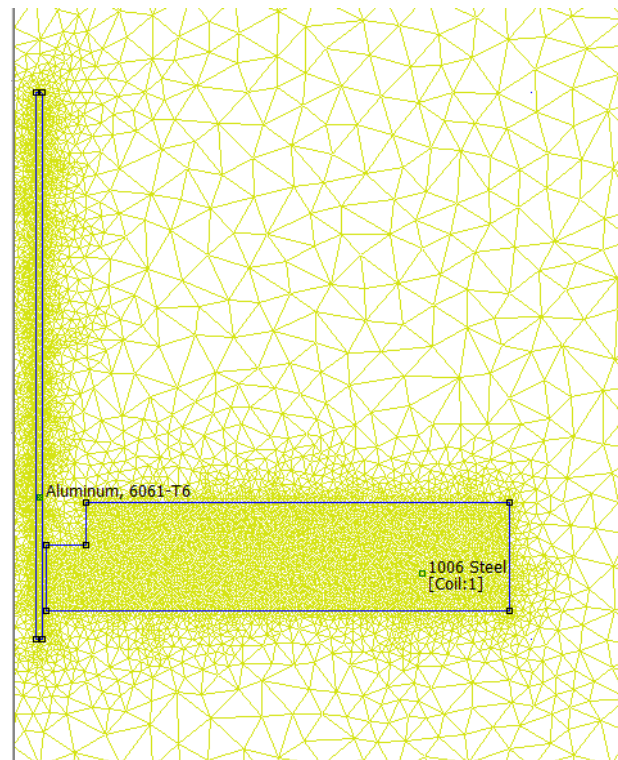


**Figure 75 - Screen-shot of the FEMM model.**

Model discretization was performed with triangular elements, using a total of 11535 nodes and 22795 elements. Elements of different sizes are used with increased element density near the coil and workpiece area as shown in Figure 75, in order to provide accurate results in the main area of interest without influencing the computational time.

After the mesh definition, the problem was solved using the finite element method. The outputs of the FEMM software [63] retrieved from the simulation were the magnetic field density distribution, with its corresponding axial ( $B_z$ ) and radial ( $B_r$ ) components, as well as the source and induced Eddy current density ( $J_\theta$ ). Figure 76 presents an example of the magnetic field density distribution, for the case of a 12.5 kV discharge.

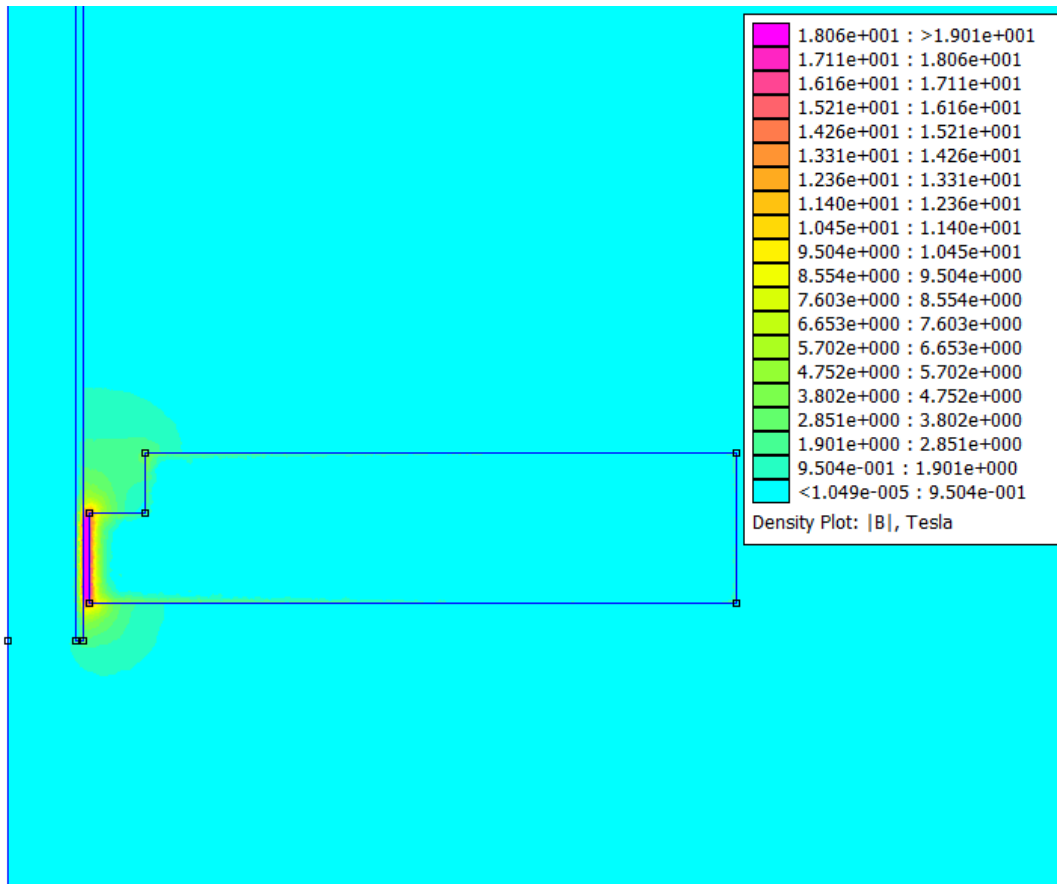


**Figure 76 - Magnetic field density for a 12.5 kV discharge.**

By analyzing the magnetic field density distribution, a concentration of the magnetic field is clearly visible in the region where the tube and coil are closer.

The radial and axial Lorentz force components can be calculated from the equations:

$$F_r = J_\theta \cdot B_z \quad (5.6)$$

$$F_z = -J_\theta \cdot B_r \quad (5.7)$$

The magnetic pressure components in the radial and axial directions ( $P_r$  and  $P_z$ ) are calculated through the integration of the Lorentz force in the radial ( $F_r$ ) and axial ( $F_z$ ) directions as well, along the thickness of the workpiece:

$$P_r = \int_{z=0}^{z=t} F_r \cdot dz \quad (5.8)$$

$$P_z = \int_{z=0}^{z=t} F_z \cdot dz \quad (5.9)$$

Where  $B_r$  and  $B_z$  represent the magnetic field's radial and axial components, and  $J_\theta$  the circumferential component of the induced current [51].

Using the circuit parameters previously depicted, the FEMM software calculates the magnetic field density and circumferential eddy current. The magnetic pressure is then calculated in the post-processing step. Figure 77 presents the magnetic pressure evolution along the length of the tube for the three energy levels tested.

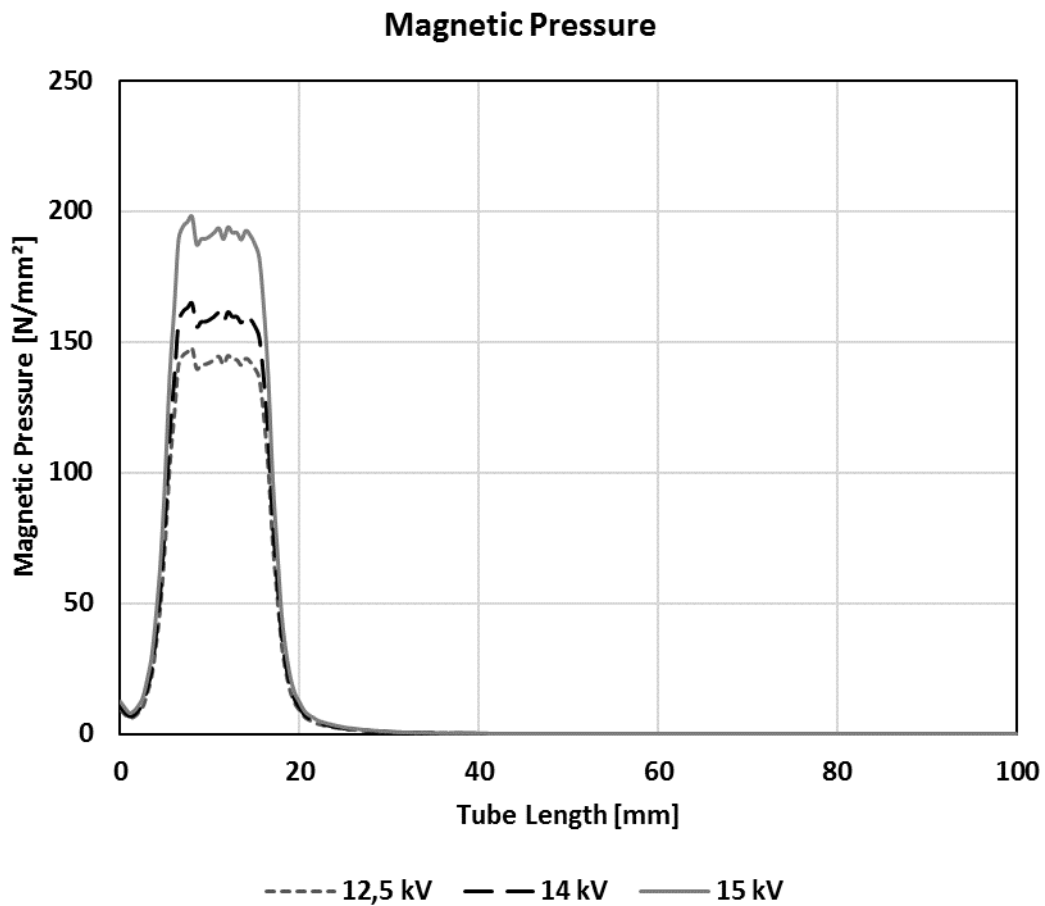


Figure 77 - Magnetic pressure distribution along the tube length for the three energy levels.

### 5.2.3 The Mechanical Model

The Abaqus software allows the modelling of distinct processes using two fundamental methods of formulating the problem and time integration. For simpler, quasi-static problems, the static implicit method is usually applied. The dynamic explicit modelling strategy show particular use for solving problems involving more complex contact and sliding conditions, greater element deformations, and when non-linear material behaviour is dealt with. Considering that the EMPT process takes place at high speeds and that inertial effects cannot be disregarded [6, 8, 52], a dynamic approach is the obvious path to model the mechanical problem.

In order to input the non-uniform and time dependent electromagnetic pressure characteristic for the EMPT processes that is calculated using the FEMM software [63], a user-defined subroutine was implemented. A VDLOAD allows the definition of the variation of a distributed load as a function of position, time, velocity, etc. for a group of points [64].

Both the aluminum tube and composite mandrel are modelled as shell parts in order to reduce the number of elements and to be able to implement the Hashin damage model for composites. The mechanical properties used to define the tube in the mechanical model relate to a generic aluminum alloy and not specifically to the alloy used in the experiments and are listed in Table 18 and Table 19.

*Table 18 - Density and elastic properties for the aluminum tube [65].*

Density (ton/mm <sup>2</sup> )	Young's Modulus (GPa)	Poisson's Ratio
2.7 e <sup>-9</sup>	70	0.3

*Table 19 - Johnson-Cook plastic properties for the aluminum tube [65].*

A (MPa)	B (MPa)	n	m	Melting Temp (°C)	Transition Temp (°C)
265	426	0.3	1	600	23

The material model for the composite rod was harder to implement, due to the complex microstructure and mechanical behaviour of fiber filled polymers. The Hashin model for long fiber reinforced laminates was used due to the lack of a better suiting model for the type of materials being tested.

The properties used for the composite are shown in Table 20.

*Table 20 - Density, elastic and Hashin damage properties used in the composite modelling.*

Density [ton/mm <sup>2</sup> ]	1.635 e <sup>-9</sup>	Longitudinal Tensile Strength [MPa]	1500
E1 [MPa]	140000	Longitudinal Compressive Strength [MPa]	1200
E2 [MPa]	10000	Transverse Tensile Strength [MPa]	50
Nu12	0.3	Transverse Compressive Strength [MPa]	250
G12 [MPa]	5000	Longitudinal Shear Strength [MPa]	70
G13 [MPa]	5000	Transverse Shear Strength [MPa]	70
G23 [MPa]	5000	-	-

A single step is used for the FE simulation. The step time chosen was 350  $\mu\text{s}$  which includes the application of the electromagnetic force (which has a peak around 10  $\mu\text{s}$  as well as some time for the springback and stabilization of the deformed tube wall to occur.

General contact was defined between the outer mandrel's surface and the node region defined by the aluminum tube. Tangential frictionless behaviour was selected for contact definition.

The pressure is applied through the use of a VDLOAD which imports the load data from the electromagnetic solver. The area for the application of pressure is partitioned and is 12 mm long like in the experimental setup. Boundary conditions define the tube's endings as an encastre.

The mandrel and tube are meshed using shell S4R quad elements with minimized mesh transition. The element size chosen for the tube was 0.2 mm. For the mandrel, different element sizes were used because of the varying level of detail present. Joint 1 was not modelled because of its similarities with Joint 2.

The objective of this numerical model is to provide a fast and accurate prediction of the EMPT tube joining process in order to easily design, implement and optimize form-fit tube joints between metallic and composite materials. The desired outputs for evaluation included at first:

- Nodal displacement in the tube, to evaluate the radial reduction;
- Thinning of the tube wall, to assess the critical regions of the tube;
- Mandrel damage, to define critical energy.

Because of certain of the model's characteristics, the relevant outputs were reduced to the nodal displacements:

- Due to the use of shell elements, thinning in the tube cannot be evaluated. On the other hand, a significant reduction in computational time allows to complete a simulation in less than an hour;
- The inability to create a complete material model for the composite that included not only the elastic properties but also brittle damage would allow to obtain conclusions regarding the rod's fracture often encountered in the experimental procedure for higher voltage.

### 5.3 Results for the FE Simulation

This sub-chapter presents the results obtained from the FE simulations regarding the nodal displacements along the tube length and groove filling.

#### 5.3.1 Diameter Reduction

Results for the magnitude of displacement calculated using the Abaqus model developed are presented here for joints 2 and 3 and all energy levels (12.5, 14 and 15 kV) for later comparison with measurements from the obtained samples. Figure 78 and 79 present the node sets chosen for the analysis for both the tube and the target for each of the joints.

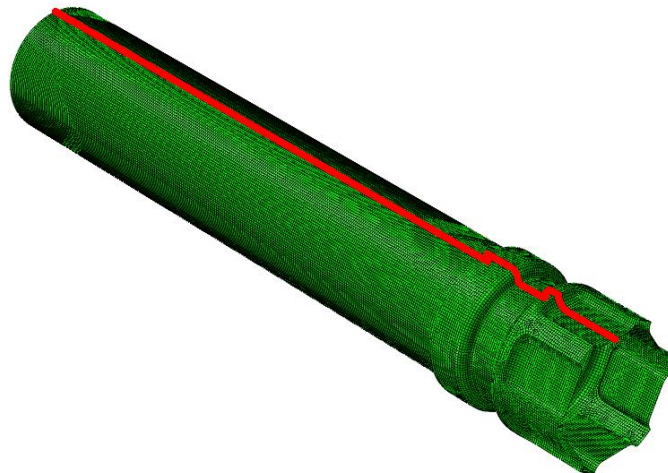
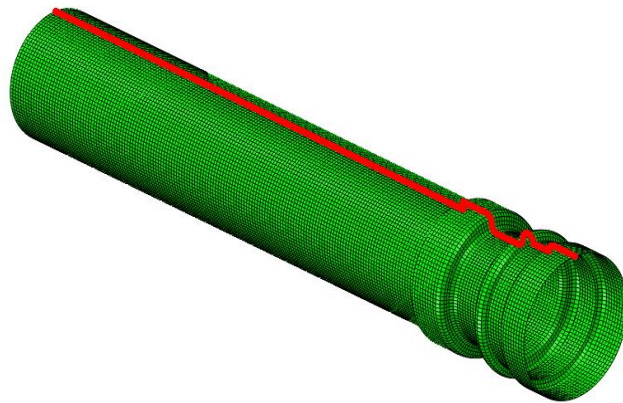


*Figure 78 - Node sets chosen for the target for joints 2 and 3.*

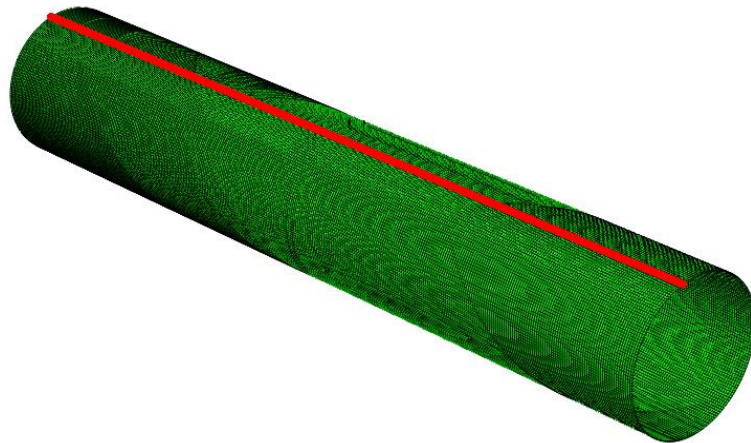


*Figure 79 - Representation of the node set chosen for the tube analysis.*

The last frame of the simulations for joints 2 and 3, displaying the displacement output is presented in Figure 80 and Figure 81.

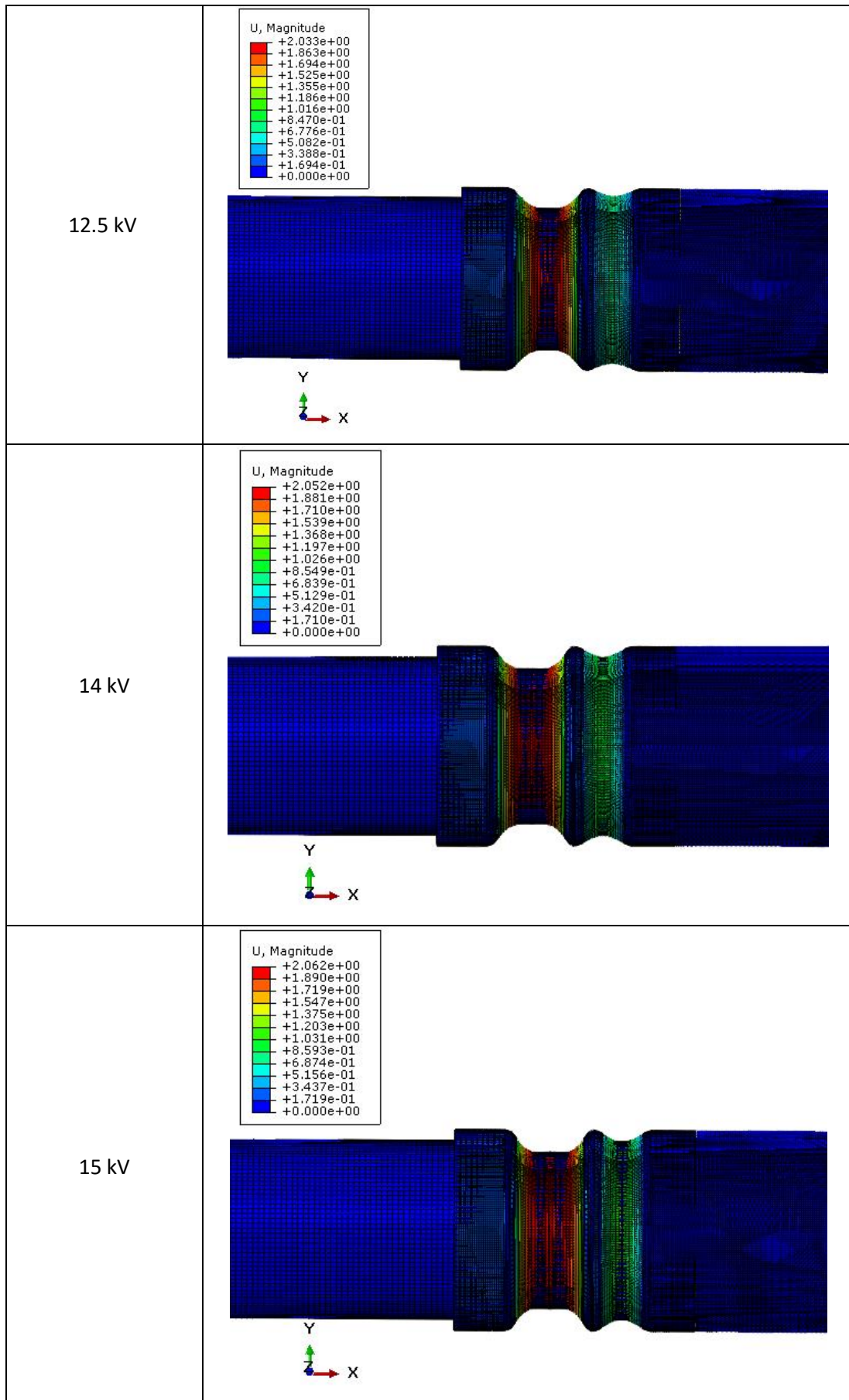


Figure 80 - Final frame of Joint 2's simulation with plot contours representing displacement (magnitude).

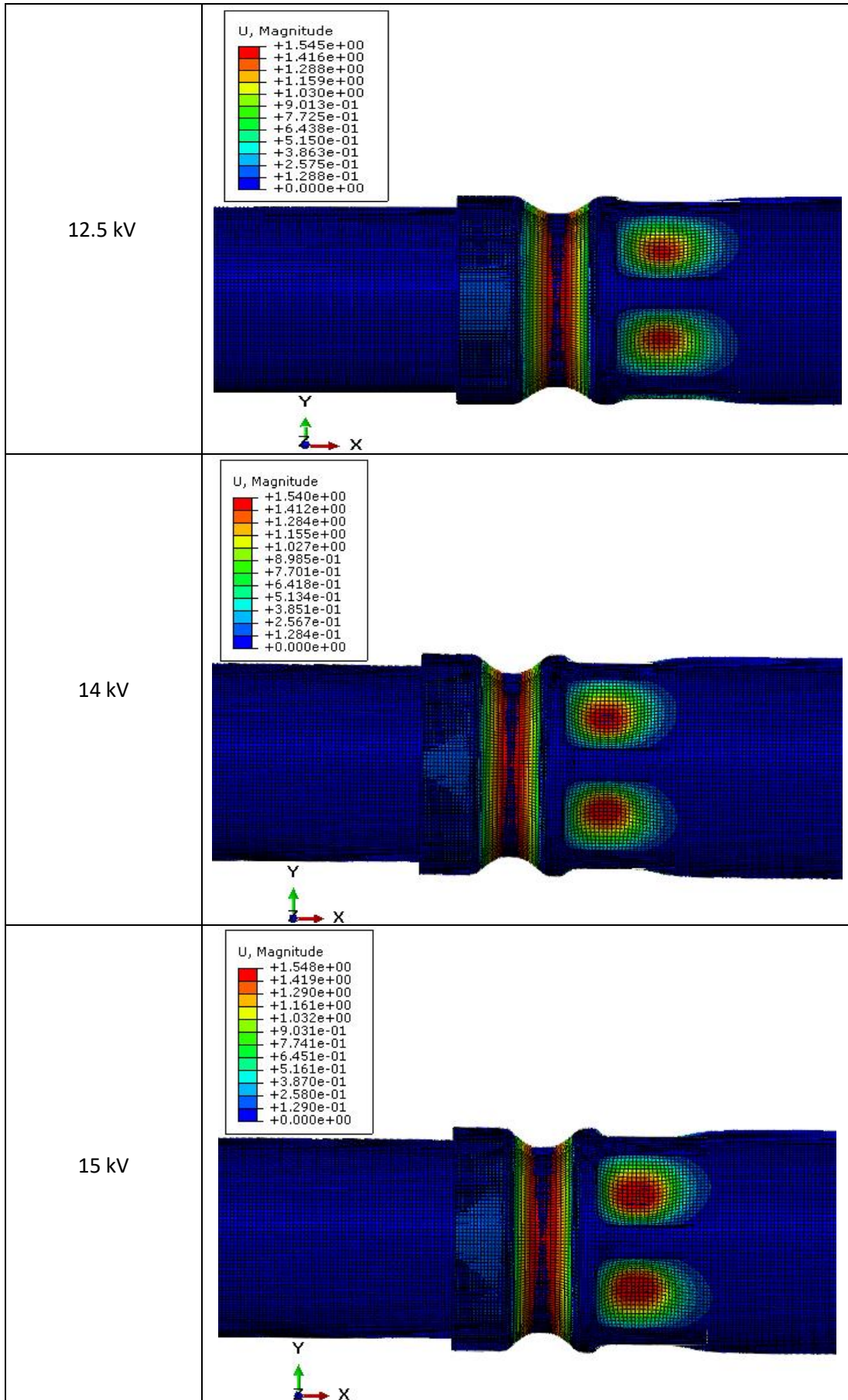


Figure 81 - Final frame of Joint 3's simulation with plot contours representing displacement (magnitude).

The graphics presented in Figure 82, Figure 83 and Figure 84 present the evolution of the tube's radius along a line of nodes through the length of the tube for Joint 2. The target geometry is also represented and it refers to the composite mandrel's geometry in the beginning of the simulation (frame 0).

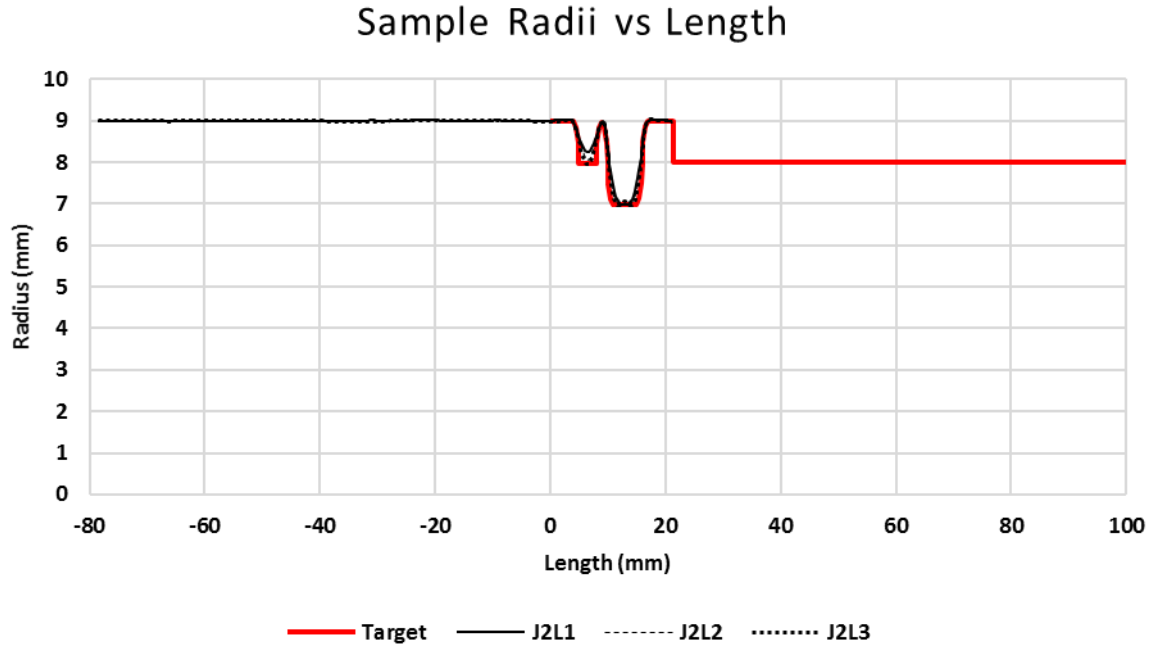


Figure 82 - Evolution of the radius for the full length of the sample for different energy levels in Joint 2.

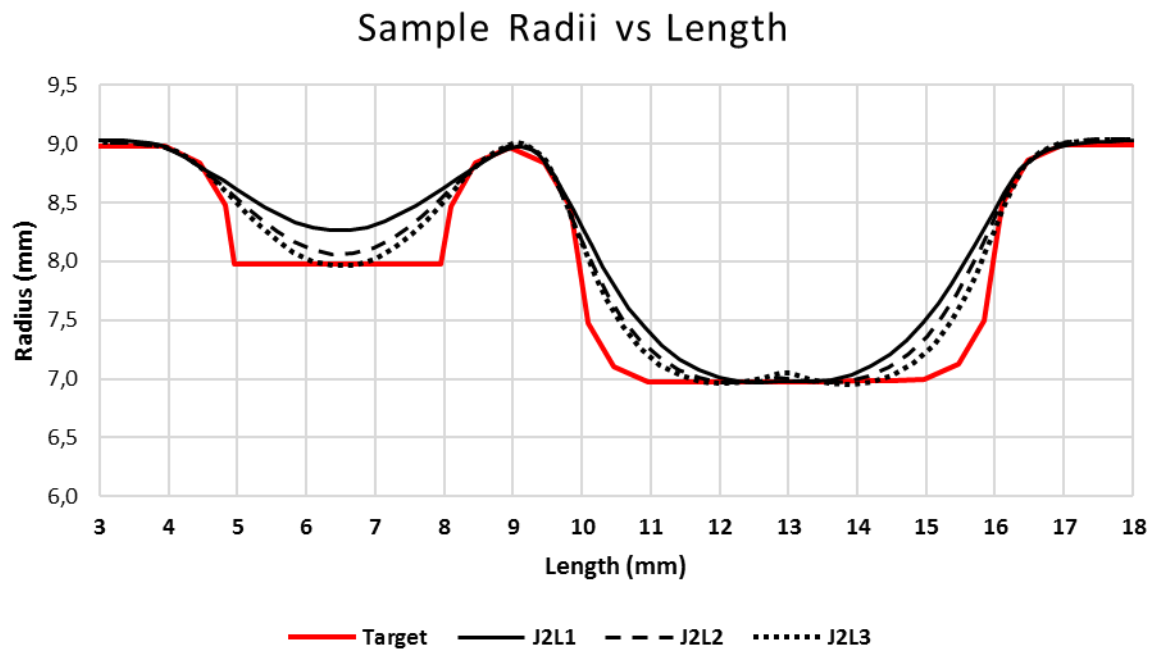


Figure 83 - Zoomed evolution of the radius for the samples in Joint 2.

**Table 21 - Minimum radius detected in the simulation at each groove for the different energy levels (Joint 2).**

Discharge energy	Groove 1 (shallow)	Groove 2 (deep)
12.5 kV	8.26 mm	6.97 mm
14 kV	8.06 mm	6.97 mm
15 kV	7.96 mm	6.96 mm

The results presented in Table 21 relate to the minimum radius values calculated for each of the grooves. Through the analysis of the final frame of the simulation, it is visible that although the deeper joint presents adequate groove filling for all discharge energies, the same does not occur for the shallower groove.

Another relevant aspect has been found regarding the groove filling in the simulation: when complete groove filling is achieved, the tube tends to rebound, as it shown in Figure 84. This rebound increases with increasing forming energy.

### Sample Radii vs Length (deeper groove)

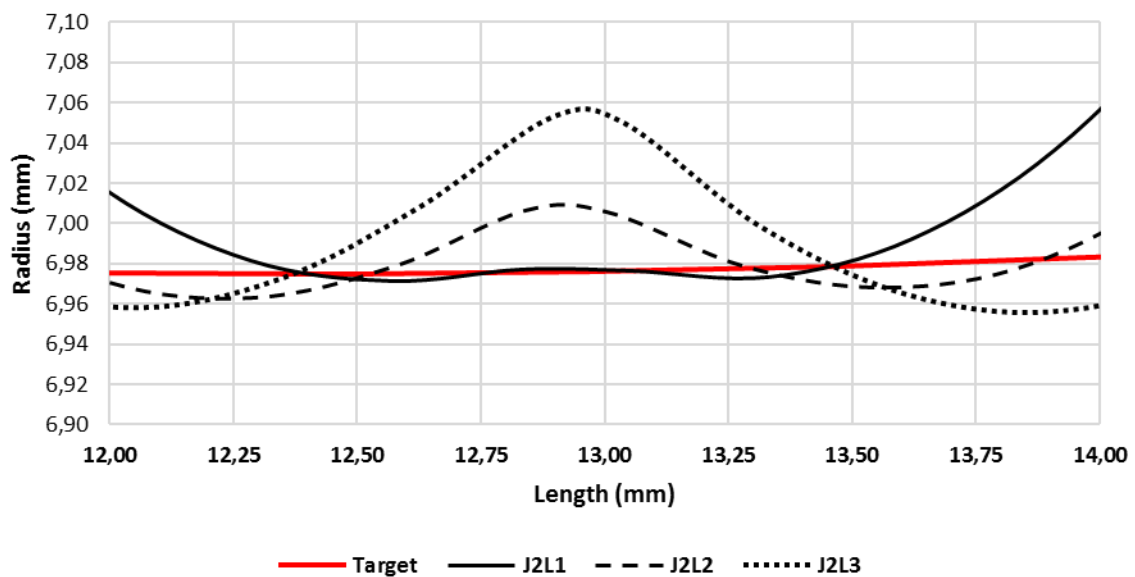


**Figure 84 - Nodal distribution emphasizing the rebound phenomena occurring in the simulation.**

A review regarding the rebound effect in the EMPT has shown that this is a common effect, both in simulations and experimental work. It usually occurs when the impact energy and velocity are excessive [66, 67]. When the workpiece contacts the die, a part of the kinetic energy is dissipated in the form of plastic deformation. If there is energy excess that is not dissipated, then the rebound effect occurs [67].

Due to the implementation of a non-coupled approach, and since the electromagnetic force decays with increasing distance between coil and workpiece, the acting force is usually overestimated [68]. This results in a more violent collision than the experimental work that may also account for the rebound.

The same analysis is performed for Joint 3. The evolution of the tube radius is presented in Figure 85 through Figure 88.

Table 22 presents the minimum radius values calculated for each of the grooves. Adequate groove filling is observed for all discharge energies.

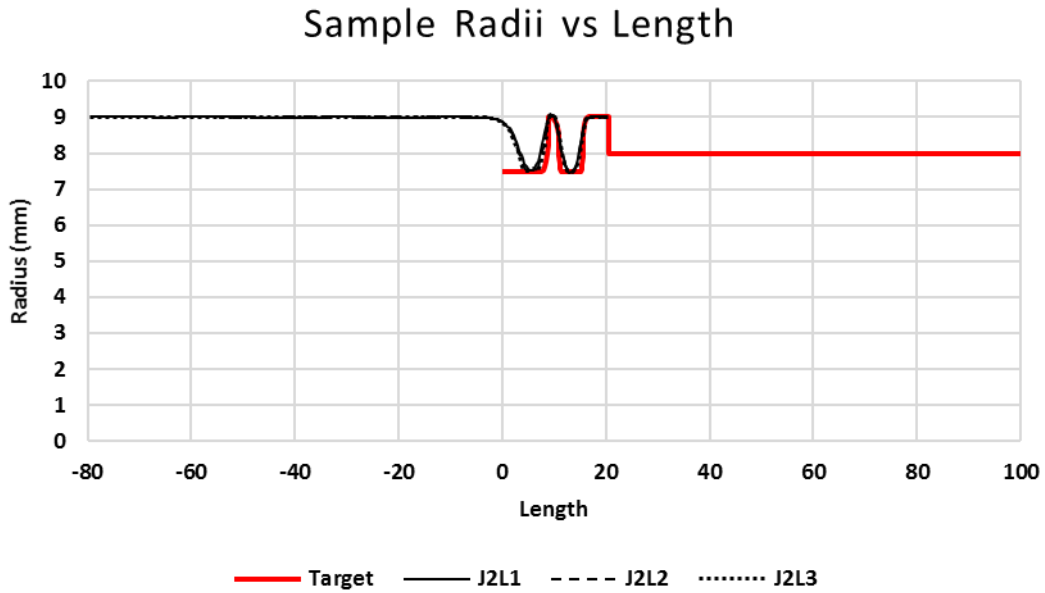


Figure 85 - Evolution of the radius for the full length of the sample for different energy levels in Joint 3.

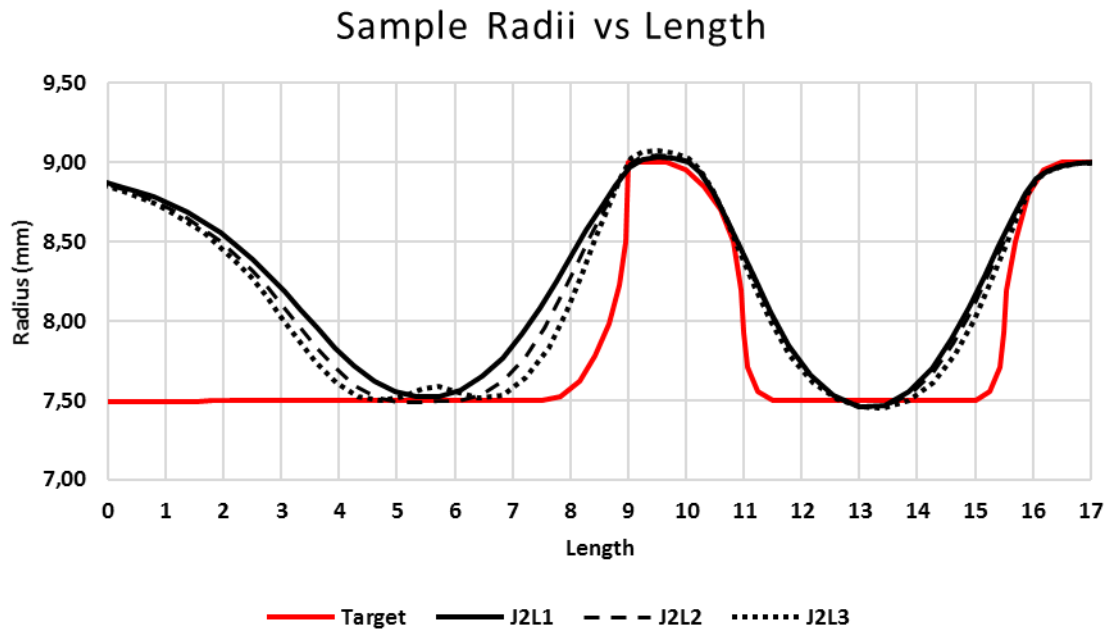


Figure 86 - Detail of the evolution of the radius with the length of the sample for different energy levels in Joint 3.

The same rebound effect observed for Joint 2 occurs, but it is located in the torque groove. The detail of both regions is presented in Figure 87 and Figure 88.

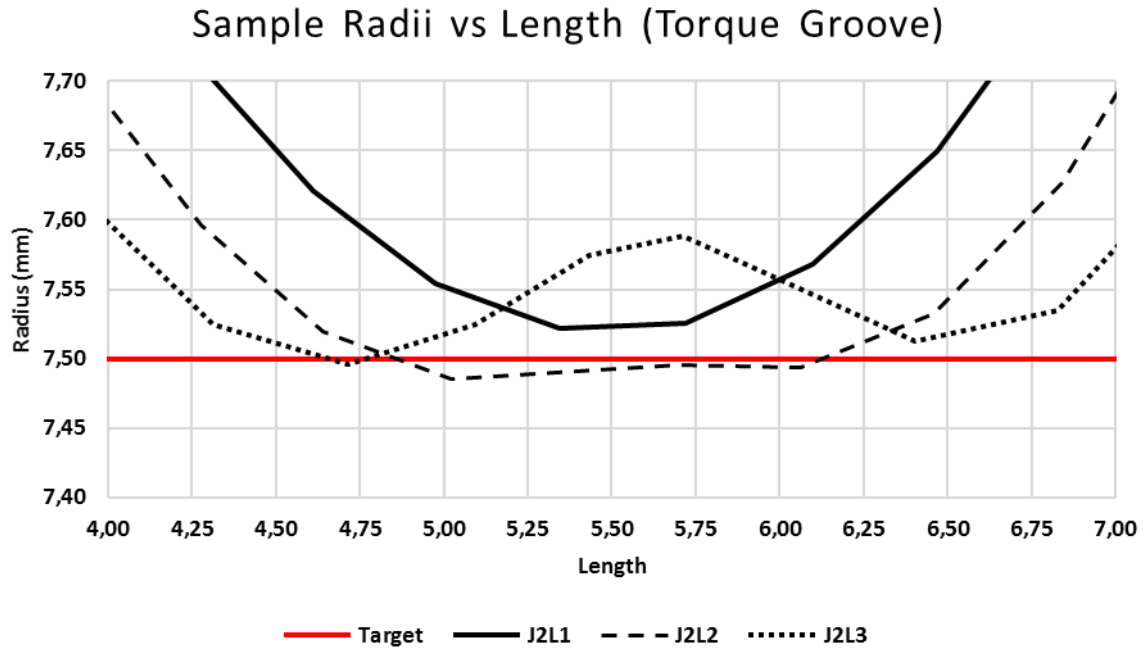


Figure 87 - Detail of the evolution of the radius with the length of the sample for different energy levels in Joint 3 (torque groove).

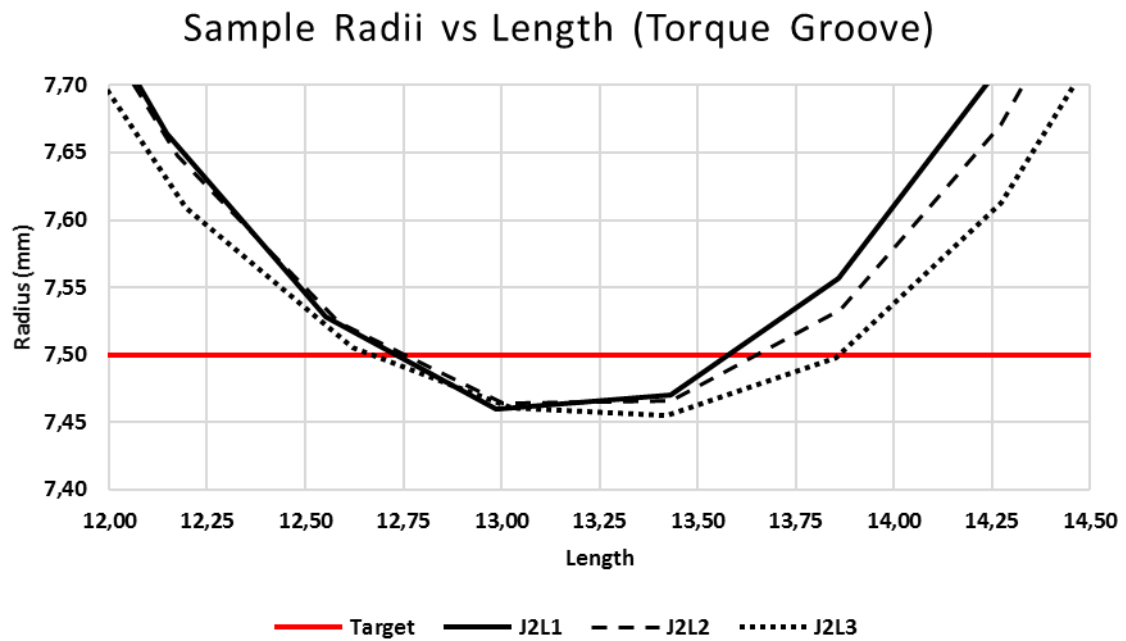


Figure 88 - Detail of the evolution of the radius with the length of the sample for different energy levels in Joint 3 (radial groove).

**Table 22 - Minimum radius detected in the simulation at each groove for the different energy levels (Joint 3).**

Discharge energy	Groove 1 (axial)	Groove 2 (torque)
12.5 kV	7.46 mm	7.52 mm
14 kV	7.46 mm	7.48 mm
15 kV	7.46 mm	7.50 mm

## 5.4 Discussion and Conclusions

In order to validate the EMPT joining FE model developed, displacements measured from the physical samples are compared to the results obtained from the numerical simulations. In order to compare the outer tube diameter measured from the samples with the shell surface's displacement, representing the inner tube wall, it is assumed that minimal tube thinning occurs in that region, maintaining its 1 mm thickness.

Table 23 and Table 24 present the minimum diameters measured for the samples produced at each of the energy levels for Joint 2 and 3 respectively, and the results obtained from the numerical simulations.

**Table 23 - Numerical and experimental values for the minimum external diameter in the tube for joint 2.**

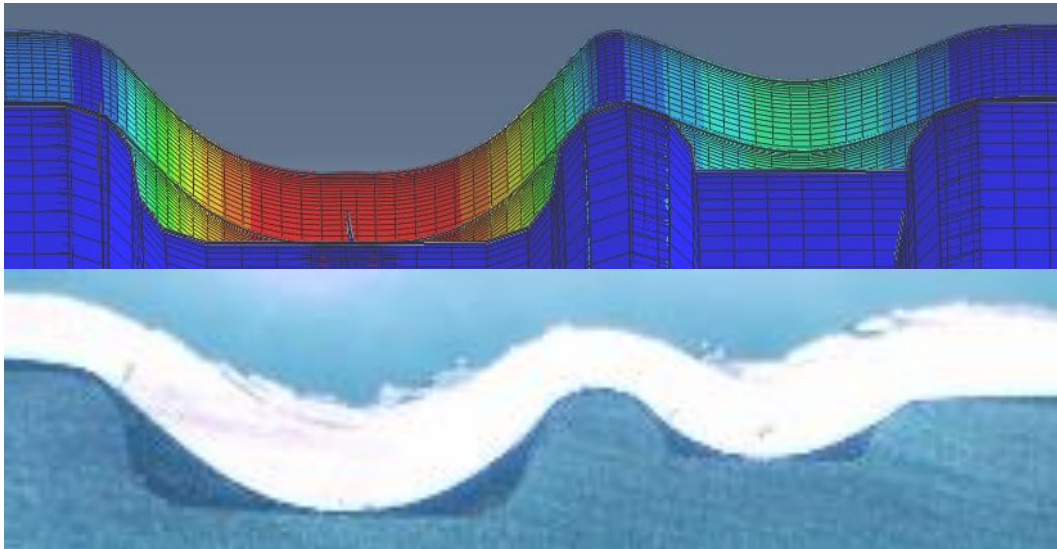
Discharge energy	Numerical (mm)		Experimental (mm)		Error (%)	
	G1	G2	G1	G2	G1	G2
12.5 kV	15,94	18,52	16,6	18,2	3,97	1,75
14 kV	15,94	18,12	15,9	18	0,25	0,66
15 kV	15,92	17,92	15,7	17,9	1,40	0,11

**Table 24 - Numerical and experimental values for the minimum external diameter in the tube for joint 3.**

Discharge energy	Numerical (mm)	Experimental (mm)	Error (%)
12.5 kV	16,92	17,2	1,62
14 kV	16,92	17,3	2,19
15 kV	16,92	17	0,47

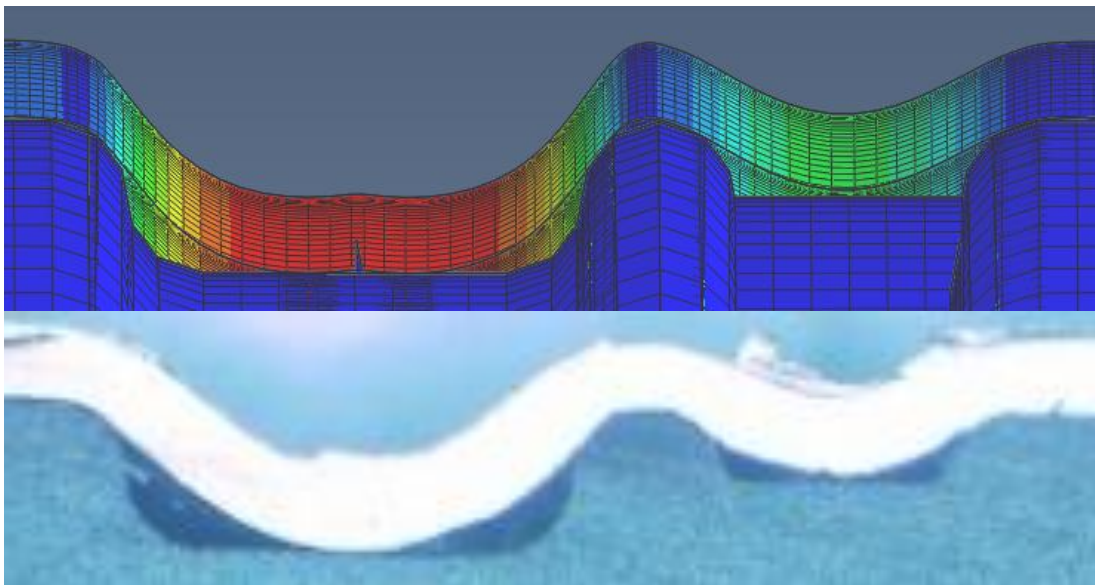
A good agreement is found when comparing the numerical and experimental results in terms of the minimal diameters at each of the grooves.

A visual analysis was also performed in order to evaluate the model's accuracy. Figure 89 through Figure 94 provide a close-up comparison between the simulation and the micro-cuts performed in the experimental analysis. Note that, in some of the micro-cuts, the tube's surfaces are not very clear due to appearance of burrs and rough edges due to the cutting operation.



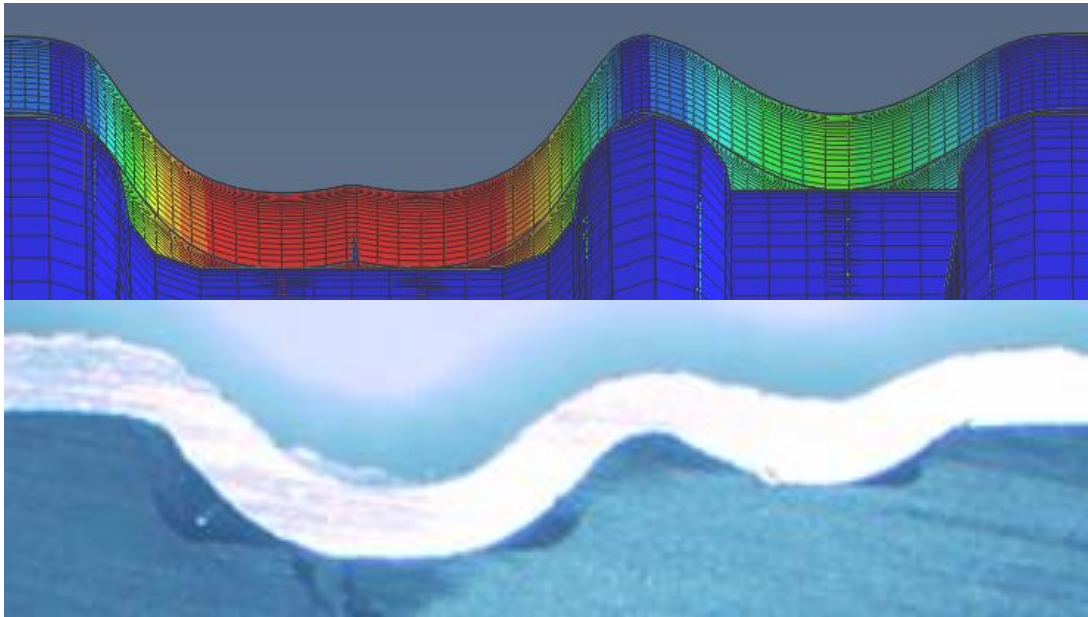
**Figure 89 - Comparison between the numerical simulation and the cut views for Joint 2 formed with 12.5 kV.**

Figure 89 presents close-ups of the grooves for Joint 2 formed with 12.5 kV. The narrower groove reveals differences, since the simulation predicts that the tube will not reach the groove bottom while in reality it does. When analyzing the deeper groove however, similarities regarding groove filling are clearly visible. Both images show that the tube reaches the bottom and the void on the left side is slightly larger as exhibited on the micro-cut.



**Figure 90 - Comparison between the numerical simulation and the cut-views for Joint 2 formed with 14 kV.**

When comparing the simulations with the experimental results for the 14 kV discharge, an increased resemblance is found in the shallower groove, as it is visible in Figure 90. For the deeper groove, however, a higher degree of deformation and groove filling is present in the simulations: there is a bigger contact area and smaller voids than in the experimental micro-cut.



**Figure 91 - Comparison between the numerical simulation and the cut views for Joint 2 formed with 15 kV.**

In the case of Joint 2 formed with 15 kV, the shallow groove presents similar groove filling on both the simulation and micro-cut. For this energy level, the simulation presents the previously described variation when the displacement results were presented. As it is visible in the micro-cut, the composite mandrel has fractured both on the deeper groove's bottom as well as on the separation between both grooves. Although this behaviour was not replicated, and increased tube deformation is clearly visible.

The same type of analysis is performed for joint 3. Shell thickness was not displayed since it affected the model's visualization and characterization.

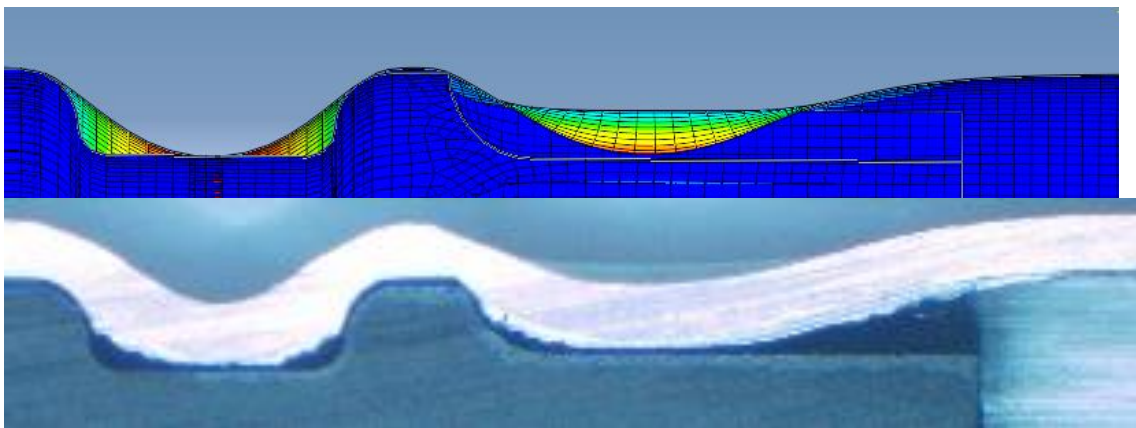


**Figure 92 - Comparison between the numerical simulation and the cut views for Joint 3 formed with 12.5 kV.**

When analyzing Joint 3 formed with 12.5 kV (Figure 92), a good approximation is achieved, especially on the radial groove (left): this zone features similar groove filling and deformation in both the micro-cut and simulation. On the torque groove (right side), increased deformation is visible in the micro-cut. This is due to the fact that deformation through thickness is not represented with the use of shell elements. This allows to show localized deformations and an improved filling of the torque groove for all energies.

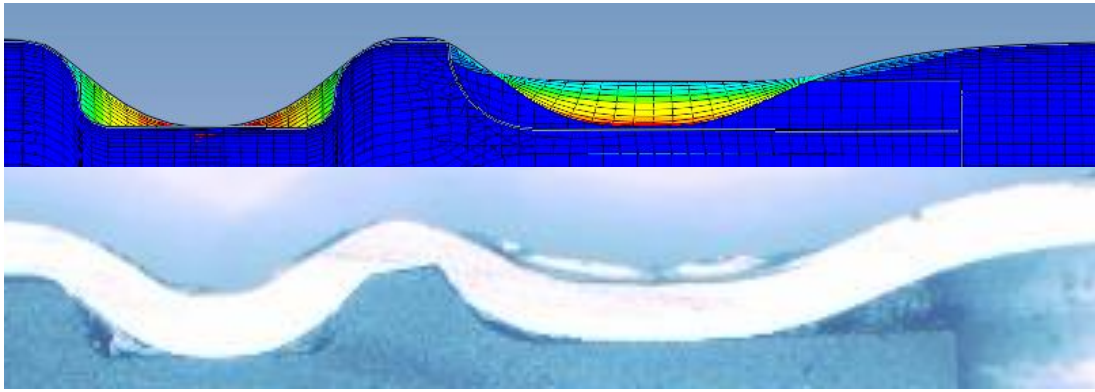


*Figure 93 - Comparison between the numerical and the cut-view for Joint 3 formed with 14 kV.*

Good approximation in terms of groove filling are observed in Figure 93 for both grooves, although the same problems existing in are exhibited: localized tube deformation (shearing) is not visible in the simulation, and is responsible for the differences in voids.

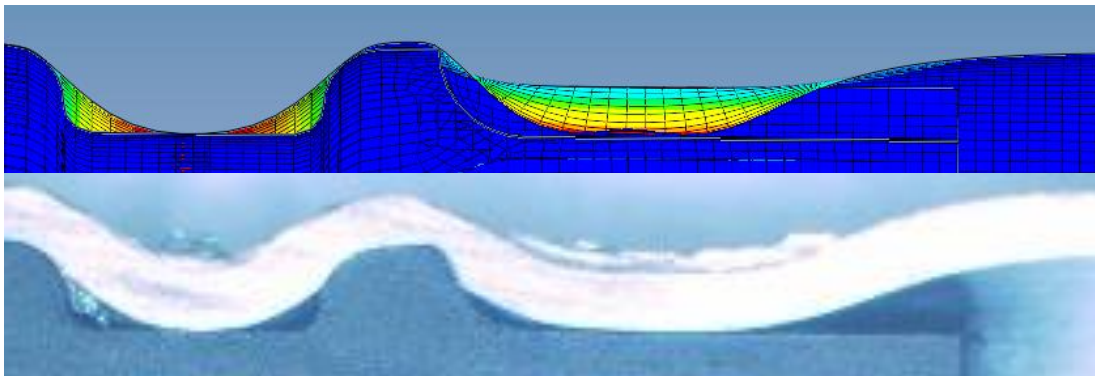


*Figure 94 - Comparison between the numerical simulation and the cut-view for Joint 3 formed with 15 kV.*

When analyzing Figure 94, although localized deformation on the right side of the separation between grooves present in the micro-cut was not represented in the simulation, it is quite like the experiments. Besides that, both grooves show very similar groove filling when compared with the physical specimen.

The comparisons between the simulation results and the micro-cuts suggest that in terms of displacements, a valid model has been developed. Although some of the features exhibited in the micro-cuts, such as thinning and composite damage are not modelled, moderately accurate results can be obtained in terms of the groove filling.

## **5.5 Summary and Outlook**

In this chapter, a finite element model is developed with the objective to replicate the joint creation process by EMPT tube compression in order to allow fast and accurate predictions for tube joining operations by EMPT. After a review regarding the most common techniques to model the tube joining process, the simulation is divided into two main problems: the electromagnetic component, solved using the FEMM software taking into consideration the geometry of the setup, the machine's characteristics and the tube's electrical properties; the mechanical component, solved using the Abaqus software and includes the tube and rod's mechanical properties as well as the magnetic pressure

calculated from the previous step. An uncoupled approach and the use of shell elements in the mechanical simulation allow reduction in computational time. The model is then compared with the experimental results obtained for validation.

First, a comparison between the minimal radii at each groove on both the simulation and the experiments has been performed. The values obtained are in the same order of magnitude, providing errors under 4% for the tested specimens

A visual analysis was also performed, comparing the geometries obtained from the simulations with the micro-cuts. Although there are some visible differences between them, a clear evolution in tube deformation with increasing forming energy is verified.

Both the visual resemblances between the developed model and the micro-cuts as well as the analysis of the nodal coordinates allow to conclude that acceptable results can be obtained from the numerical model, making it possible to predict the behaviour of the aluminum tube in the joining process for tubular workpieces. Further improvement to the model, more precisely in the composite's material model and in the interaction between the two workpieces, may make it possible to predict not only the tube's behaviour, but the composite rod's as well, allowing for a more accurate prediction of the critical pressure at which it breaks.

# 6 CONCLUSIONS

---

## 6.1 Conclusions

The production of lighter frames and more efficient structures is possible due to combination of different types of materials with specific properties. However, one of the main difficulties in the creation of such structures relates to the ability to join them. Conventional methods, such as mechanical fastening or the use of adhesives already allow the design this type of structures; however, they feature specific limitations, such as the material addition and weight increase in the case of mechanical fastening, or the requirement for surface preparation and inability to disassemble the joint without its destruction, in the case of adhesive bonding. The EMPT provides a unique way to join similar or dissimilar materials while overcoming the conventional methods' flaws. The work developed in this thesis intends to present experimental results in order to investigate the viability of the form-fit joining process between tubular metal-composite workpieces.

In order to study the applicability of the EMPT in the joining process of composite to metal tubes, a set of three joints was designed to withstand both axial and torque solicitations. After the joint creation, using three different discharge energies, the specimens were analyzed using micro-cuts and tensile tests. Joint behaviour for different energy levels was evaluated and the following conclusions can be taken regarding the experimental analysis:

- Although the connections could not be tested until rupture, the achieved forces are in the order of 10 to 20 kN.
- The improved geometry, using two axial grooves instead of a single groove, allows for a better distribution of stress when solicited and withstands higher loads.
- The geometry of the grooves appears to be critical to prevent composite fracture and to create a successful joint creation. The differences in the behaviour of the three designs may be due to the increased contact area originated from the double grooved features or to the increased tube deformation, since both factors increase from joint 1 to joint 3.
- Good correlation has been found between the results from the tensile tests and the micro-cut analysis. Joints that showed inadequate groove filling, corresponding to

the lowest energy level, tend to fail through Mode 1 (deformation of the aluminum tube out of the groove). On the other hand, most of the joints that appeared fractured in the micro-cuts displayed a behaviour consistent with a broken sample.

The creation of a numerical model was considered useful for the prediction of process outputs and for further optimization of electromagnetic tube joining technique. The most influencing phenomena were considered, dividing the process into the electromagnetic and the mechanical components. A non-coupled approach to the problem was implemented. Maxwell's magnetostatic equations are used to describe the electromagnetic problem and solved using the electrical and magnetic FE software FEMM, and the magnetic pressure due to Lorentz forces is calculated. The magnetic pressure distribution is then used as input the Abaqus 3D mechanical model in order to compute the tube deformation. Numerical simulations are performed using the machine and material parameters that replicate the experimental procedure performed. Nodal displacements were analyzed to study the evolution of the tube's radius along its length and were compared with measurements made on the physical joint specimens. A visual analysis was also performed, comparing the micro-cuts and the simulation's last frame in order to validate the model in terms of groove filling and general appearance. A good correlation has been found between the experimental and numerical results, indicating the validity of the developed model, and possible optimization of the joint design process.

Taking advantage of the work developed in this thesis, it is concluded that the EMPT is a suitable process for the form-fit joining of metal and composite tubular workpieces. When adequate energy is used in the discharge (meaning that the electromagnetic pressure is neither high enough for the immediate breaking of the composite rod, nor too low that the metal tube is not formed into the groove), and when the geometrical groove parameters are properly calculated and optimized, viable, resistant joints can be created.

## 6.2 Future Work

The execution of this document lead to the interest in further studying the electromagnetic pulse technology and its applications. Some topics that showed relevance to this subject were not included either due to the lack of resources or the lack of time to execute such operations.

- Parameters other than the magnetic pulse intensity can be tested in order to better assess the applicability of this technology to the creation of form-fit joints between dissimilar materials. These parameters include groove dimensions, the number of axial grooves in the case of torque joints and the use of other material combinations that could be parametrically tested in order to discover the optimal parameter combinations.
- Two more joints were designed but were not studied in this thesis due to the lack of equipment for torsion tests. These joints, now presented as joints 4 and 5, featured grooves for torque resistance.
  - Joint 4 was designed to withstand torsional forces exclusively. It was based from the work developed in [34] and it would be useful as a comparison between the effectiveness of single purpose joints (resistant to either axial or toque solicitations) or multi-purpose joints (resistant to both solicitations) along with joint 1.
  - Joint 5 followed the idea of joint 3 in the way that it is designed to resist to both axial and torsional forces. The difference is that the radial gap is positioned in the center of the effective area of the coil used in the experimental tests instead of having both groove types separated.

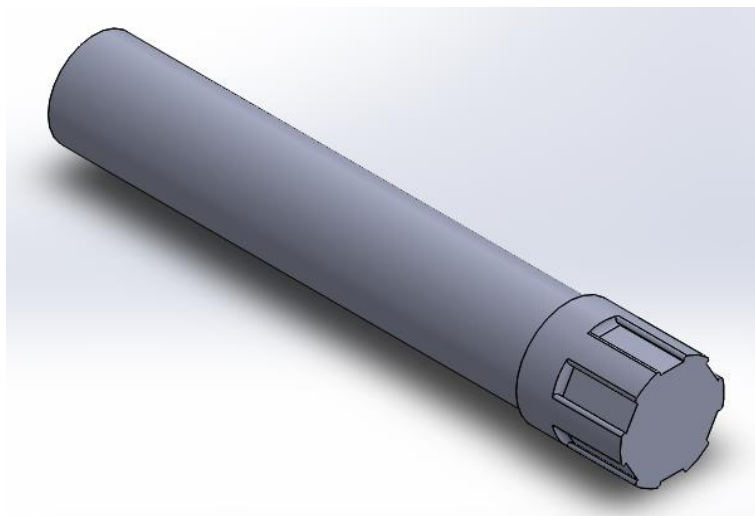


*Figure 95 - Joint design 4 (from SolidWorks).*

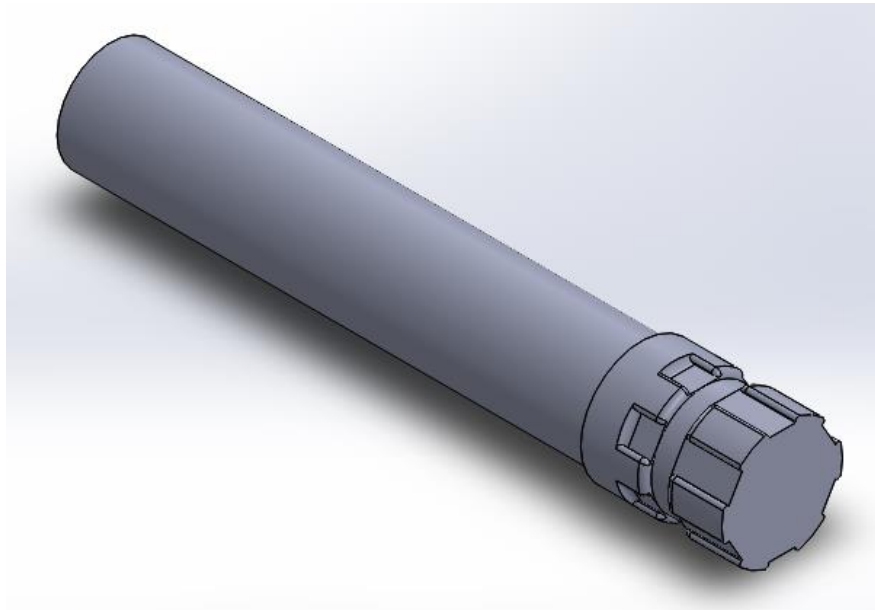


*Figure 96 - Joint design 5 (from SolidWorks).*

- Due to sliding between the support system and the composite rod, the complete behaviour could not be studied from the beginning of the tensile tests until the rupture of the joint. The repetition of these tests with could improve joint characterization. Changes in the rod's roughness or in the support system could allow to obtain the load responsible for the joints' mode 2 failure. Such changes may include the use of clamps with threaded surfaces to improve the interlock.
- Although the FE model developed provided rather accurate predictions in terms of groove filling, several improvements could be performed in the mechanical model. These include better tube and rod's material models that accurately describe the high-velocity deformations, impact and fracture behaviors. The use of 3D solid elements for the tube definition would also be interesting since it would allow for the analysis of tube thinning and localized deformation.
- The simulation of the joints' tensile tests may also be a useful for the prediction of their tensile behaviour. This would allow to use the FE methods for the prediction of the joining process itself but also to predict failure loads and critical regions.

## 7 REFERENCES

---

1. Amancio-Filho, S.T. and J.F. dos Santos, *Joining of polymers and polymer–metal hybrid structures: Recent developments and trends*. Polymer Engineering & Science, 2009. **49**(8): p. 1461-1476.
2. Barnes, T.A. and I.R. Pashby, *Joining techniques for aluminium spaceframes used in automobiles: Part II — adhesive bonding and mechanical fasteners*. Journal of Materials Processing Technology, 2000. **99**(1–3): p. 72-79.
3. Kah, P., et al., *Techniques for joining dissimilar materials: metals and polymers*. Reviews on Advanced Materials Science, 2014. **36**(2): p. 152-164.
4. Massey, S. *Composite to Metal Joining: Engineered Bonded Systems*. 2013 28/09/2016]; Available from: <https://ewi.org/composite-to-metal-joining-engineered-bonded-systems/>.
5. Buxton, A.L. *Welding technologies for polymers and composites*. 2012 6/09/2016]; Available from: <http://www.twi-global.com/technical-knowledge/published-papers/welding-technologies-for-polymers-and-composites>.
6. Gayakwad, D., et al., *A Review on Electromagnetic Forming Process*. Procedia Materials Science, 2014. **6**: p. 520-527.
7. Marré, M., A. Brosius, and A.E. Tekkaya, *Joining by Compression and Expansion of (None-)Reinforced Profiles*. Advanced Materials Research: Flexible Manufacture of Lightweight Frame Structures, 2008. **43**: p. 57-68.
8. Psyk, V., et al., *Electromagnetic forming—A review*. Journal of Materials Processing Technology, 2011. **211**(5): p. 787-829.
9. Zittel, G., *A Historical Review of High Speed Metal Forming*. 2010.
10. Broekaert, F. and M.D. Ketele, *An exploratory study into the feasibility of magnetic pulse forming*, in *Faculty of Engineering*. 2009, Gent University.
11. Kamal, M., *A Uniform Pressure Electromagnetic Actuator for Flat Sheet Forming*. 2005, The Ohio State University.
12. Paese, E., *Estampagem eletromagnética de chapas finas: viabilidade técnica*. 2010, Escola de Engenharia - Universidade Federal do Rio Grande do Sul.
13. Weddeling, C., *Electromagnetic Form-Fit Joining in Faculty of Mechanical Engineering*. 2014, Dortmund University of Technology: Dortmund, Germany.
14. Plum, M., *Electromagnetic Forming, Forming and Forging*. Vol. 14. 1988: ASM International.
15. *ASM Handbook*. 9th ed. Vol. 14: Forming and Forging, Sheet Forming. 1988: ASM International.
16. *ASM Handbook*. Vol. 14B: Metalworking, Sheet Forming. 2006: ASM International.

17. Davis, J.R., *ASM Specialty Handbook: Tool Materials*. 1995: ASM International.
18. Schafer, R., P. Pasquale, and S. Kallee, *Industrial Application of the Electromagnetic Pulse Technology*. PSTproducts GmbH, 2009.
19. Schäfer, R. and P. Pasquale, *The electromagnetic pulse technology (EMPT): forming, welding, crimping and cutting*, P. GmbH, Editor. 2014: Alzenau, Germany.
20. Suzuki, H., M. Murata, and H. Negishi, *The effect of a field shaper in electromagnetic tube bulging*. Journal of Mechanical Working Technology, 1987. **15**: p. 229-240.
21. Yu, H., et al., *Effect of fieldshaper on magnetic pressure in electromagnetic forming*. Journal of Materials Processing Technology, 2005. **168**: p. 245-249.
22. Dehra, M.S., *High velocity formability and factors affecting it*. 2006, The Ohio State University
23. Daehn, G.S., *High Velocity Metal Forming*. ASM Handbook Volume 14B Metalworking: Sheet Forming. 2006.
24. Barreiro, P., V. Schulze, and D. Löhe, *Influence of Process Parameters on Structure and Mechanical Properties of Joints Produced by Electromagnetic Forming and Friction Stir Welding*. Advanced Materials Research, 2008. **43**: p. 47-56.
25. Schulze, V., P. Barreiro, and D. Löhe, *Investigation of the Influence of Process Parameters on the Structure and the Mechanical Properties of Joints Produced by electromagnetic Compression*. Advanced Materials Research, 2006. **10**: p. 79-88.
26. Shirbman, V. and Y. Tomer, *Magnetic pulse technology for improved tube joining and forming*. Tube & Pipe Technology, 2006: p. 91-95.
27. Barreiro, P., et al. *Strength of Tubular Joints Made by Electromagnetic Compression at Quasi-static and Cyclic Loading*. in *Proceedings of the 2th International Conference on High Speed Forming*. 2006.
28. Beerwald, C., et al. *New Aspects of Electromagnetic Forming*. in *Advanced Technology of Plasticity*. 1999. Erlangen/Nuremberg, Germany.
29. Beerwald, C., M. Beerwald, and A. Henselek, *Design and Adaptation of EMF Equipment – From Direct Acting Multi-turn Coils to Separable Tool Coils for Electromagnetic Tube Compression in 1st International Conference on High Speed Forming*. 2004: Dortmund, Germany.
30. Zhang, P., *Joining enabled by high velocity deformation*. 2003, The Ohio State University
31. Kleiner, M., et al., *Investigation of force-fit joints produced by electromagnetic tube compression*. Annals of the German Academic Society for Production Engineering, WGP, 2006. **13**(1): p. 227-230.
32. Weddeling, C., et al., *Development of design principles for form-fit joints in lightweight frame structures*, in *4th International Conference on High Speed Forming*. 2010.
33. Homberg, W., et al., *Joining by Forming of Lightweight Frame Structures* Advanced Materials Research, 2006. **10**: p. 89-100.
34. Park, Y., H. Kim, and S. Oh, *Design of axial/torque joint made by electromagnetic forming*. Thin-Walled Structures, 2005. **43**: p. 826-844.
35. Eguia, I., P. Zhang, and G.S. Daehn, *Improved Crimp-Joining of Aluminum Tubes onto Mandrels with Undulating Surfaces* in *1st International Conference on High Speed Forming*. 2004.
36. Weddeling, C., et al., *Influence of groove characteristics on strenght of form-fit joints*. Journal of Materials Processing Technology, 2010.
37. Bühler, H. and E.v. Finckenstein, *Bemessung von Sickenverbindungen für ein Fügen durch Magnetumformung*, 104. *Werkstatt und Betrieb*. 1971.
38. Vanhulsel, P., et al., *Groove Design for Form-Fit Joints Made by Electromagnetic Pulse Crimping*. Sustainable Construction and Design, 2011.

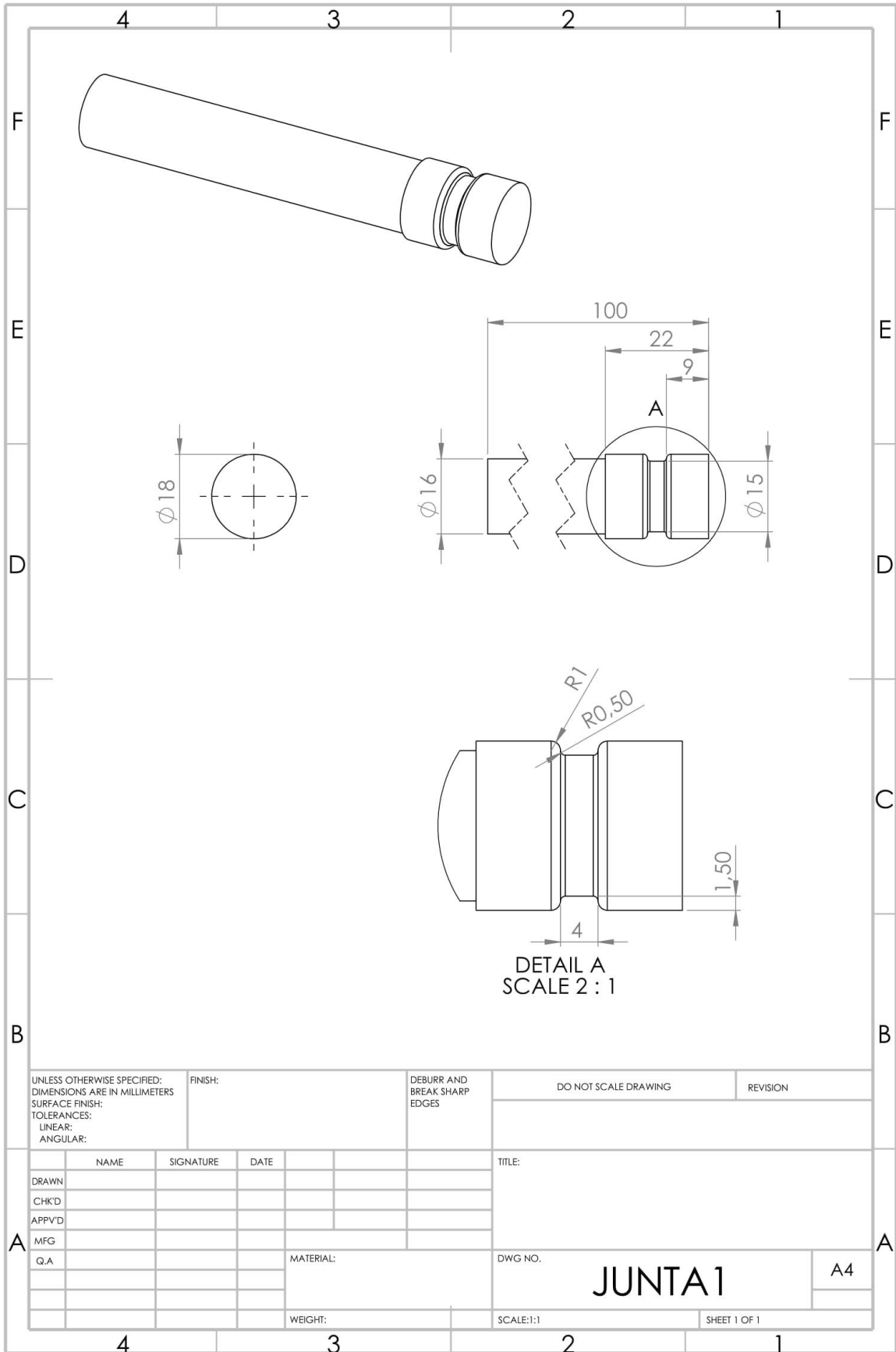
39. Faes, K., O. Zaitov, and W.d. Waele, *Electromagnetic pulse crimping of axial form fit joints*, in *International Conference of High Speed Forming*. 2012: Dortmund.
40. Bogaert, D., et al., *Torque resistance of joints made by magnetic pulse crimping*, in *Sustainable Construction and Design*. 2012.
41. Faes, K., et al., *Design of Electromagnetic Pulse Crimp Torque Joints*, in *International Conference of High Speed Forming*. 2014: Daejon, Korea.
42. Hulsel, P.V. and M.V. Wouterghem, *Magnetic pulse crimping of mechanical joints*. 2011, Ghent University.
43. METALMORPHOSIS.
44. AZOM. *Aluminium Alloys - Aluminium 6082 Properties, Fabrication and Applications, Supplier Data by Aalco*. 6/12/2016]; Available from: <http://www.azom.com/article.aspx?ArticleID=2813>.
45. AircraftMaterials. *Aluminium Alloy 6082*. 06/12/2016]; Available from: <https://www.aircraftmaterials.com/data/aluminium/6082.html>.
46. Aalco. *Aluminum Alloy 6082*. 7/12/2016]; Available from: [http://www.aalco.co.uk/datasheets/Aluminium-Alloy\\_6082-T6~T651\\_148.ashx](http://www.aalco.co.uk/datasheets/Aluminium-Alloy_6082-T6~T651_148.ashx).
47. Ltd, A.M., *Alluminum Alloy 6082 - T6 Extrusions*.
48. PolyLanema. *Ertalon PA66-GF30*. 05/12/2016]; Available from: <http://www.polylanema.pt/pt/produtos/plasticos-de-engenharia/pla-a1sticos-de-engenharia/ertalon-66---gf30a-ae.html>.
49. QuadrantPlastics. *Ertalon® 66-GF30*. 06/12/2016]; Available from: <http://www.quadrantplastics.com/eu-en/products/machinable-plastics/engineering-80-160-c/ertalon-R-and-nylatron-R-products/ertalon-R-66-gf30.html>.
50. QuadrantPlastics, *ERTALON® 66-GF30 DataSheet*.
51. Oliveira, I.V.d., *Electromagnetic Forming Process: Numerical Modelling and Analysis of Process Parameters*, in *Departamento de Engenharia Mecânica*. 2013, Faculdade de Engenharia da Universidade do Porto: Oporto, Portugal.
52. Siddiqui, M.A., *Numerical Modelling and Simulation of Electromagnetic Forming Process* 2009, University of Strasbourg: Luxembourg.
53. Nassiri, A., et al., *Analytical Model and Experimental Validation of Single Turn, Axisymmetric Coil for Electromagnetic Forming and Welding*. *Procedia Manufacturing*, 2015. **1**: p. 814-827.
54. ASTM, *Standard Test Methods and Definitions for Mechanical Testing of Steel Products*. 2003.
55. Conraux, P., et al., *3D Finite element modelling of electromagnetic forming processes*, in *2nd International Conference on High Speed Forming (ICHFS)*. 2006: Dortmund, Germany.
56. Unger, J., et al., *Strategies for 3D simulation of electromagnetic forming processes*. *Journal of Materials Processing Technology*, 2008. **199**(1–3): p. 341-362.
57. Zohoor, M. and B. Ghorbani, *Analytical and Numerical Investigation of Significant Parameters on Strength of Electromagnetically Assembled Aluminum Tube Joints* *Journal of Modern Processes in Manufacturing and Production*, 2014. **3**.
58. Mousavi, S.M.H. and M. Loh-Mousavi, *Comparison of Tube Formability in Electromagnetic Forming and High Speed Hydroforming*. *Advanced Design and Manufacturing Technology*, 2015. **8**.
59. Nassiri, A., et al., *Analytical and Numerical Investigation of Tube Compression with a Multi-Turn, Axisymmetric Coil* in *7<sup>th</sup> International Conference on High Speed Forming*. 2016.
60. Karch, C.K. and K. Roll, *Transient Simulation of Electromagnetic Forming of Aluminium Tubes*. *Advanced Materials Research*, 2005. **6**(8).

61. Takatsu, N., et al., *High-Speed Forming of Metal sheets by Electromagnetic Force*. The Japan Society of Mechanical Engineers, 1988. **31**(1): p. 142-148.
62. Manea, T.E., M.D. Verweij, and H. Blok. *The importance of velocity term in the electromagnetic forming process*. in *Proceedings of 27th General Assembly of the International Union of Radio Science*. 2002.
63. Meeker, D., *FEMM 4.2 Magnetostatic Tutorial*. 2006.
64. *Abaqus 6.14 Documentation - Abaqus User Subroutines Reference Guide*. 2014.
65. Lesuer, D., *Experimental Investigations of Material Models for Ti-6Al-4V and 2024-T3*. 1999, Lawrence Livermore National Laboratory.
66. Oliveira, I., P. Teixeira, and A. Reis, *Magnetic Pulse Welding of dissimilar metals: Influence of process parameters*, in *6th International Conference on High Speed Forming*. 2012.
67. Liu, X., L. Huang, and J. Li, *An experiment and simulation study of the rebound effect in electromagnetic forming process*, in *6th International Conference on High Speed Forming*. 2014.
68. Xiong, W., et al., *Effect of the Duration of Electromagnetic Pulse Force on the Rebound Suppression in V-Bending Experiment*, in *6th International Conference on High Speed Forming*. 2014.

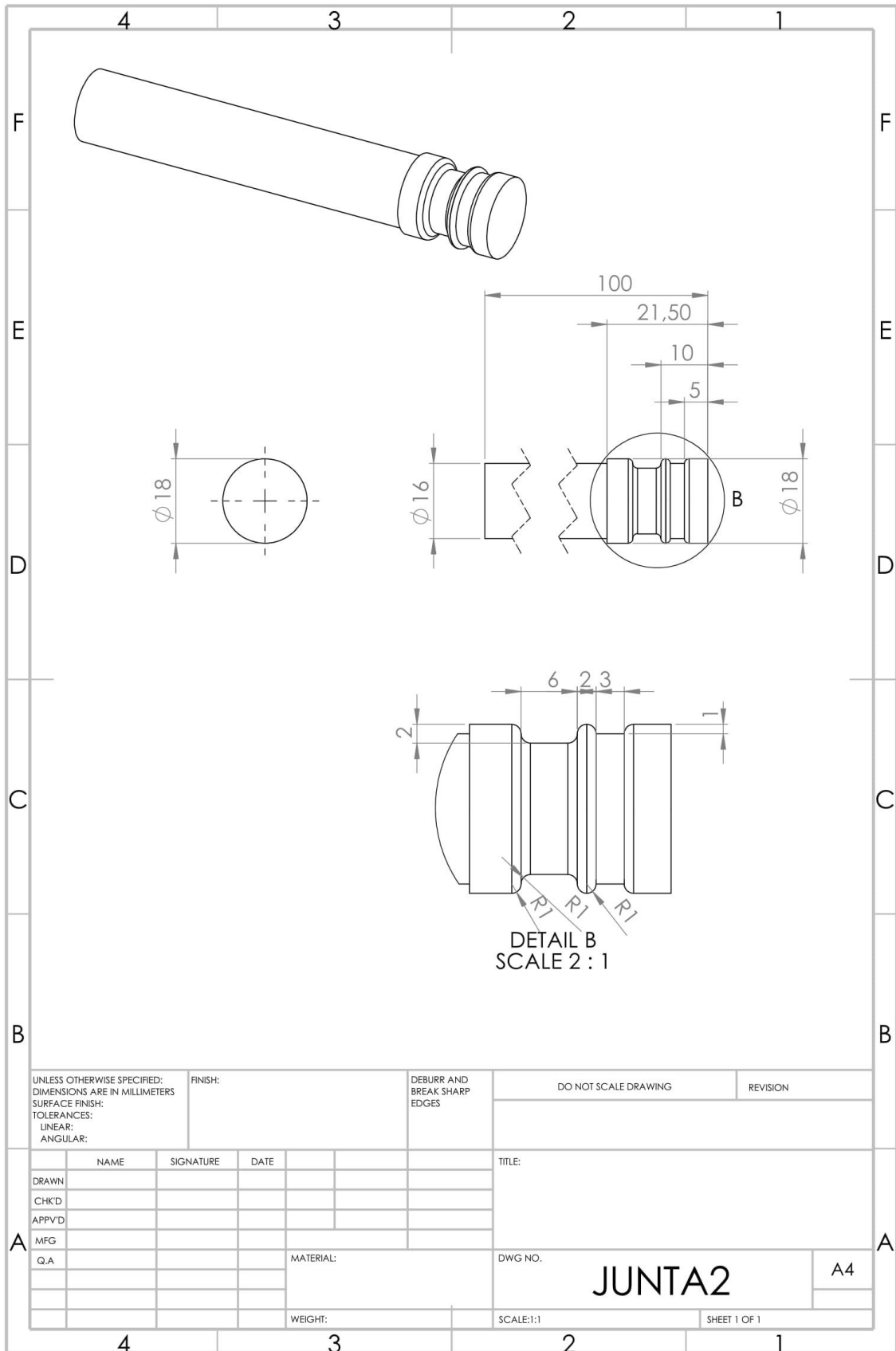
## 8 ANNEXES

---

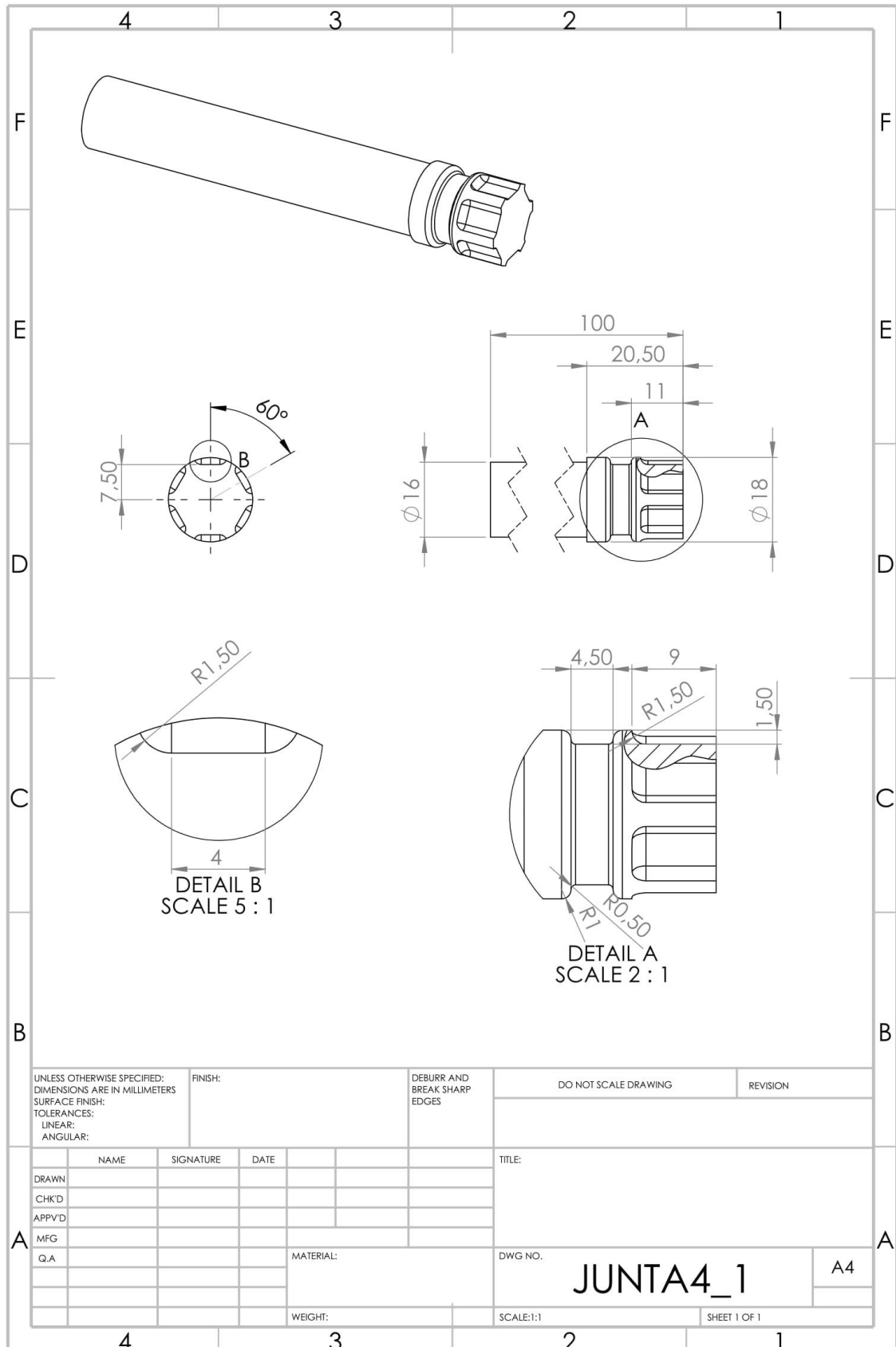
### 8.1 Joint design 1 (single axial groove)



### 8.2 Joint design 2 (double axial groove)



### 8.3 Joint design 3 (axial and torque grooves)



## 8.4 EN AW 6082 Data Sheet

### Aluminium Alloy 6082 - T6 Extrusions



#### SPECIFICATIONS

Commercial	6082
EN	6082

Aluminium alloy 6082 is a medium strength alloy with excellent corrosion resistance. It has the highest strength of the 6000 series alloys. Alloy 6082 is known as a structural alloy. In plate form, 6082 is the alloy most commonly used for machining. As a relatively new alloy, the higher strength of 6082 has seen it replace 6061 in many applications. The addition of a large amount of manganese controls the grain structure which in turn results in a stronger alloy. It is difficult to produce thin walled, complicated extrusion shapes in alloy 6082. The extruded surface finish is not as smooth as other similar strength alloys in the 6000 series.

In the T6 and T651 temper, alloy 6082 machines well and produces tight coils of swarf when chip breakers are used.

#### Applications

6082 is typically used in:

- ~ Highly stressed applications
- ~ Trusses
- ~ Bridges
- ~ Cranes
- ~ Transport applications
- ~ Ore skips
- ~ Beer barrels
- ~ Milk churns

#### CHEMICAL COMPOSITION

BS EN 573-3:2009 Alloy 6082	
Element	% Present
Silicon (Si)	0.70 - 1.30
Magnesium (Mg)	0.60 - 1.20
Manganese (Mn)	0.40 - 1.00
Iron (Fe)	0.0 - 0.50
Chromium (Cr)	0.0 - 0.25
Zinc (Zn)	0.0 - 0.20
Others (Total)	0.0 - 0.15
Titanium (Ti)	0.0 - 0.10
Copper (Cu)	0.0 - 0.10
Other (Each)	0.0 - 0.05
Aluminium (Al)	Balance

#### ALLOY DESIGNATIONS

Aluminium alloy 6082 also corresponds to the following standard designations and specifications but may not be a direct equivalent:

AA6082  
HE30  
DIN 3.2315  
EN AW-6082  
ISO: Al Si1MgMn  
A96082

#### TEMPER TYPES

The most common tempers for 6082 aluminium are:

- T6 - Solution heat treated and artificially aged
- O - Soft
- T4 - Solution heat treated and naturally aged to a substantially stable condition
- T651 - Solution heat treated, stress relieved by stretching then artificially aged

#### SUPPLIED FORMS

Alloy 6082 is typically supplied as Channel, Angle, Tee, Square bar, Square box section, Rectangular box section, Flat bar and Tube.

- Extrusions
- Bar
- Tube

#### GENERIC PHYSICAL PROPERTIES

Property	Value
Density	2.70 g/cm <sup>3</sup>
Melting Point	555 °C
Thermal Expansion	24 x10 <sup>-6</sup> /K
Modulus of Elasticity	70 GPa
Thermal Conductivity	180 W/m.K
Electrical Resistivity	0.038 x10 <sup>-6</sup> Ω .m

BS EN 755-2:2008  
Tube  
Up to 5mm Wall Thickness

Property	Value
Proof Stress	250 Min MPa
Tensile Strength	290 Min MPa
Elongation A50 mm	6 Min %
Hardness Brinell	95 HB
Elongation A	8 Min %

## 8.5 Ertalon 6.6 GF 30 Data Sheet

>> POLYAMIDE [PA 66-GF30]

# ERTALON® 66-GF30



PRODUCT DATA SHEET

Compared with virgin PA 66, this 30 % glass fibre reinforced and heat stabilised nylon grade offers increased strength, stiffness, creep resistance and dimensional stability whilst retaining an excellent wear resistance. It also allows higher max. service temperatures.

### Physical properties (indicative values <sup>■</sup>)

PROPERTIES	Test methods	Units	VALUES
Colour	-	-	black
Density	ISO 1183-1	g/cm <sup>3</sup>	1.29
Water absorption:			
- after 24/96 h immersion in water of 23 °C (1)	ISO 62	mg	30 / 56
- at saturation in air of 23 °C / 50 % RH	ISO 62	%	0.39 / 0.74
- at saturation in water of 23 °C	-	%	1.7
- at saturation in water of 23 °C	-	%	5.5
<b>Thermal Properties (2)</b>			
Melting temperature (DSC, 10 °C/min)	ISO 11357-1/3	°C	260
Glass transition temperature (DSC, 20 °C/min) - (3)	ISO 11357-1/2	°C	-
Thermal conductivity at 23 °C	-	W/(K.m)	0.30
Coefficient of linear thermal expansion:			
- average value between 23 and 60 °C	-	m/(m.K)	50 x 10 <sup>-5</sup>
- average value between 23 and 100 °C	-	m/(m.K)	60 x 10 <sup>-5</sup>
Temperature of deflection under load:			
- method A: 1.8 MPa	+ ISO 75-1/2	°C	150
Max. allowable service temperature in air:			
- for short periods (4)	-	°C	200
- continuously - for 5,000 / 20,000 h (5)	-	°C	120 / 110
Min. service temperature (6)	-	°C	-20
Flammability (7):			
- "Oxygen Index"	ISO 4589-1/2	%	-
- according to UL 94 (3 / 6 mm thickness)	-	-	HB / HB
<b>Mechanical Properties at 23 °C (8)</b>			
Tension test (9):			
- tensile stress at yield / tensile stress at break (10)	+ ISO 527-1/2	MPa	NYP / 85
	++ ISO 527-1/2	MPa	85
- tensile strength (10)	+ ISO 527-1/2	MPa	85
- tensile strain at yield (10)	+ ISO 527-1/2	%	NYP
- tensile strain at break (10)	+ ISO 527-1/2	%	5
	++ ISO 527-1/2	%	-
- tensile modulus of elasticity (11)	+ ISO 527-1/2	MPa	5000
	++ ISO 527-1/2	MPa	2700
Compression test (12):			
- compressive stress at 1 / 2 / 5 % nominal strain (11)	+ ISO 604	MPa	43 / 77 / 112
Charpy impact strength - Unnotched (13)	+ ISO 179-1/1eU	kJ/m <sup>2</sup>	50
Charpy impact strength - Notched	+ ISO 179-1/1eA	kJ/m <sup>2</sup>	6
Ball indentation hardness (14)	+ ISO 2039-1	N/mm <sup>2</sup>	165
Rockwell hardness (14)	+ ISO 2039-2	-	M 76
<b>Electrical Properties at 23 °C</b>			
Electric strength (15)	+ IEC 60243-1	kV/mm	27
	++ IEC 60243-1	kV/mm	18
Volume resistivity	+ IEC 60093	Ohm.cm	> 10 <sup>14</sup>
	++ IEC 60093	Ohm.cm	> 10 <sup>12</sup>
Surface resistivity	+ IEC 60093	Ohm	> 10 <sup>13</sup>
	++ IEC 60093	Ohm	> 10 <sup>12</sup>
Relative permittivity ε <sub>r</sub> - at 100 Hz	+ IEC 60250	-	3.9
	++ IEC 60250	-	6.9
- at 1 MHz	+ IEC 60250	-	3.6
	++ IEC 60250	-	3.9
Dielectric dissipation factor tan δ - at 100 Hz	+ IEC 60250	-	0.012
	++ IEC 60250	-	0.19
- at 1 MHz	+ IEC 60250	-	0.014
	++ IEC 60250	-	0.04
Comparative tracking index (CTI)	+ IEC 60112	-	475
	++ IEC 60112	-	475

Note: 1 g/cm<sup>3</sup> = 1,000 kg/m<sup>3</sup>; 1 MPa = 1 N/mm<sup>2</sup>; 1 kV/mm = 1 MV/m. NYP: there is no yield point

#### Legend:

- + : values referring to dry material
- ++ : values referring to material in equilibrium with the standard atmosphere 23 °C / 50 % RH (mostly derived from literature)

- (1) According to method 1 of ISO 62 and done on discs Ø 50 mm x 3 mm.
- (2) The figures given for these properties are for the most part derived from raw material supplier data and other publications.
- (3) Values for this property are only given here for amorphous materials and not for semi-crystalline ones.
- (4) Only for short time exposure (a few hours) in applications where no or only a very low load is applied to the material.
- (5) Temperature resistance over a period of 5,000/20,000 hours. After these periods of time, there is a decrease in tensile strength - measured at 23 °C - of about 50 % as compared with the original value. The temperature values given here are thus based on the thermal-oxidative degradation which takes place and causes a reduction in properties. Note, however, that the maximum allowable service temperature depends in many cases essentially on the duration and the magnitude of the mechanical stresses to which the material is subjected.
- (6) Impact strength decreasing with decreasing temperature, the minimum allowable service temperature is practically mainly determined by the extent to which the material is subjected to impact. The value given here is based on unfavourable impact conditions and may consequently not be considered as being the absolute practical limit.
- (7) These estimated ratings, derived from raw material supplier data and other publications, are not intended to reflect hazards presented by the material under actual fire conditions. There is no 'UL File Number' available for Ertalon 66-GF30 stock shapes.
- (8) The figures given for the properties of dry material (+) are for the most part average values of tests run on test specimens machined out of rods Ø 40 - 60 mm. Except for the hardness tests, the test specimens were then taken from an area mid between centre and outside diameter, with their length in longitudinal direction of the rod (parallel to the extrusion direction).
- (9) Test specimens: Type 1 B
- (10) Test speed: 5 mm/min (chosen acc. to ISO 10350-1 as a function of the ductile behaviour of the material (tough or brittle))
- (11) Test speed: 1 mm/min
- (12) Test specimens: cylinders Ø 8 mm x 16 mm
- (13) Pendulum used: 4 J
- (14) Measured on 10 mm thick test specimens (discs), mid between centre and outside diameter.
- (15) Electrode configuration: Ø 25 / Ø 75 mm coaxial cylinders ; in transformer oil according to IEC 60296 ; 1 mm thick test specimens.

■ This table, mainly to be used for comparison purposes, is a valuable help in the choice of a material. The data listed here fall within the normal range of product properties. However, they are not guaranteed and they should not be used to establish material specification limits nor used alone as the basis of design.

It has to be noted that this fibre reinforced material shows an anisotropic behaviour (properties differ when measured parallel and perpendicular to the extrusion direction).

### AVAILABILITY: see "Delivery Programme"

Ertalon® is a registered trademark of the Quadrant Group.

This product data sheet and any data and specifications presented on our website shall provide promotional and general information about the Engineering Plastic Products (the "Products") manufactured and offered by Quadrant Engineering Plastic Products ("Quadrant") and shall serve as a preliminary guide. All data and descriptions relating to the Products are of an indicative nature only. Neither this data sheet nor any data and specifications presented on our website shall create or be implied to create any legal or contractual obligation.

Any illustration of the possible fields of application of the Products shall merely demonstrate the potential of these Products, but any such description does not constitute any kind of covenant whatsoever. Irrespective of any tests that Quadrant may have carried out with respect to any Product, Quadrant does not possess expertise in evaluating the suitability of its materials or Products for use in specific applications or products manufactured or offered by the customer respectively. The choice of the most suitable plastics material depends on available chemical resistance data and practical experience, but often preliminary testing of the finished plastics part under actual service conditions (right chemical, concentration, temperature and contact time, as well as other conditions) is required to assess its final suitability for the given application.

It thus remains the customer's sole responsibility to test and assess the suitability and compatibility of Quadrant's Products for its intended applications, processes and uses, and to choose those Products which according to its assessment meet the requirements applicable to the specific use of the finished product. The customer undertakes all liability in respect of the application, processing or use of the aforementioned information or product, or any consequence thereof, and shall verify its quality and other properties.

**Quadrant Engineering Plastic Products**

global leader in engineering plastics for machining

www.quadrantplastics.com